DISSERTATION

ADVANCED SOLUTIONS FOR RAINFALL ESTIMATION OVER COMPLEX TERRAIN IN THE SAN FRANCISCO BAY AREA

Submitted by

Sounak Kumar Biswas

Department of Electrical & Computer Engineering

In partial fulfillment of the requirements

For the Degree of Doctor of Philosophy

Colorado State University

Fort Collins, Colorado

Fall 2023

Doctoral Committee:

Advisor: V. Chandrasekar

Margaret Cheney
Steven Gooch
Susan James

ABSTRACT

ADVANCED SOLUTIONS FOR RAINFALL ESTIMATION OVER COMPLEX TERRAIN IN THE SAN FRANCISCO BAY AREA

Fresh water is an increasingly scarce resource in the western United States and effective management and prediction of flooding and drought have a direct economic impact on almost all aspects of society. Therefore it is critical to monitor and predict water inputs into the hydrological cycle of the Western United States (US). The complex topography of the western US poses a significant challenge in developing physically realistic and spatially accurate estimates of precipitation using remote sensing techniques. The intricate landscape presents a challenging observing environment for weather radar systems. This is further compounded by the complex microphysical processes during the cool season which are influenced by coastal air-sea interactions, as well as orographic effects along the coastal regions of the West. The placement and density of operational National Weather Service (NWS) radars (popularly known as NEXRAD or WSR-88D) pose a challenge in meeting the needs for water resource management in the western US due to the complex terrain of the region. Consequently, areas like the San Francisco Bay Area could use enhanced precipitation monitoring, in terms of amount and type, along watersheds and surrounding rivers and streams. Shorter wavelength radars such as X-Band radar systems are able to augment the WSR-88D network, to observe better the lower atmosphere with higher temporal and spatial resolution. This research investigates and documents the challenges of precipitation monitoring by radars over complex terrain and aims to provide effective and advanced solutions for accurate Quantitative Precipitation Estimation (QPE) using both WSR-88D and the gap-filling X-Band radar systems over the Bay Area on the US West Coast, with a focus on the cool season. Specifically, this study focuses on a precipitation microphysics perspective, aiming to create an algorithm capable of distinguishing orographically enhanced rainfall from cool-season stratiform rainfall using X-Band radar observations. A radar-based rainfall estimator is developed to increase the accuracy of rainfall quantification. Additionally, various other scientific and engineering challenges have been addressed including radar calibration, attenuation correction of the radar beam, radar beam blockage due to terrain, and correction of measurements of the vertical profiles of radar observables. The final QPE product is constructed by merging the X-Band based QPE product with the operational NEXRAD based QPE product, significantly enhancing the overall quality of rainfall mapping within the Bay Area. Case studies reveal that the new product is able to improve QPE accuracy by 70% in terms of mean absolute error and root mean squared error compared to the operational products. This establishes the overall need for precipitation monitoring by gap-filling X-Band radar systems in the complex terrain of the San Francisco Bay Area.

ACKNOWLEDGEMENTS

This research is supported by the Advanced Quantitative Precipitation Information (AQPI) project. I also wish to express my gratitude to the Cooperative Institute for Research in the Atmosphere (CIRA), NOAA Physical Sciences Laboratory (PSL), the California Department of Water Resources (CA-DWR), Sonoma Water Agency (SCWA), and Santa Clara Valley Water (SCVW) for their generous support in this research. I am deeply grateful to my academic advisor, Prof. V. Chandrasekar, and Dr. Robert Cifelli for their invaluable guidance, support, and encouragement throughout this research endeavor. I am also indebted to Prof. Margaret Cheney, Dr. Steven Gooch, and Prof. Susan James for their willingness to serve on my Ph.D. committee. Furthermore, I would like to acknowledge all my colleagues at the Radar & Communications Group in the Department of Electrical and Computer Engineering at Colorado State University, as well as my colleagues at the NOAA PSL, for their support at various stages of this research.

DEDICATION

This dissertation is dedicated to my parents Mrs. Indrani Biswas and the late Mr. Prasanta Kumar Biswas

TABLE OF CONTENTS

LIST OF TABLES

LIST OF FIGURES

Chapter 1

Introduction

In the San Francisco Bay, precipitation is predominantly observed during the winter season, primarily as rain. This wintertime precipitation can be divided into two principal categories: cold or stratiform rain, which is characterized by the distinct radar bright band signature, and orographic rain, which stands out due to the absence of this radar feature. To conduct a comprehensive examination of these two distinct rain phenomena, valuable data from the Vertical Pointing S-Band profiler radar and disdrometer measurements collected from two strategically situated NOAA Hydrometeorology Testbed (HMT) sites across California are employed. The aim is to uncover the differences in the microphysical properties that distinguish cold stratiform rain from orographic rain, with the intent to refine radar rainfall estimation methods.

In addressing this research gap, a method has been developed to effectively differentiate non-bright band (NBB) rainfall from bright band (BB) rainfall. A methodological framework has been established utilizing actual radar observations of reflectivity (Z) and differential reflectivity (Z_{DR}). This distinct differentiation allows for the integration of a sophisticated algorithm into radar scans, enabling the efficient separation of these two categories of rain. Consequently, it ensures an appropriate application of both reflectivity (Z)-based and specific differential phase (K_{DP})-based methods for estimating rainfall.

Recently gap-filling X-Band weather radars with dual-polarization capabilities have been strategically deployed within the San Francisco Bay Area, specifically in the locale of Sonoma County and Santa Clara, to aid in weather monitoring and provide high-resolution Quantitative Precipitation Estimation (QPE) products. Practical application of the QPE methodology developed in this research to actual radar observations has revealed significant potential for enhancing the quality of QPE, surpassing traditional operational products that often underestimate rainfall within the coastal landscape of California.

1.1 Problem Statement

Accurate precipitation estimation is of paramount importance for diverse practical applications, including weather forecasting, flood prediction, and water resource management. Nevertheless, the precision of such measurements is frequently hindered by various fundamental and applied scientific issues [2]. One common challenge arises in the context of precipitation monitoring within regions characterized by complex topography. Remote sensing of precipitation primarily relies on weather radars, which can be ground-based, airborne, or space-based [2–5]. This study specifically delves into Quantitative Precipitation Estimation (QPE) using a ground-based X-Band weather radar surrounded by complex terrain in the San Francisco Bay Area. In such regions, the operational S-Band weather radars, often referred to as WSR-88Ds, tend to produce inaccurate rainfall estimates due to a multitude of challenges posed by the intricate terrain. Notably, a significant flooding event in Oroville, Northern California, in early 2017 highlighted the limitations of operational QPE products, which substantially underestimated radar-derived rainfall accumulations for that event. Several factors, including radar beam blockage, radar beam overshooting, discontinuity in the vertical profile of reflectivity (VPR), and variations in Drop Size Distribution (DSD), collectively contribute to the reduction in rainfall mapping accuracy. Among these factors, DSD variability significantly impacts the mean relationships between rainfall and radar observables. During the cool season, stratiform precipitation, often characterized by the presence of a Bright Band (BB), occurs when the precipitation extends well above the freezing level, causing particles to melt as they cross the environmental freezing layer. As particles melt and develop a liquid water coating, horizontal radar reflectivity is enhanced, resulting in a distinctive peak in the vertical reflectivity profile. This is commonly known as the radar bright band signature. Conversely, orographic rainfall usually results from the warm rain process when precipitation is shallow below freezing level and is intensified by topographical features. In mountainous regions, storms are significantly influenced by orographic enhancements, affecting the intensity, duration, and spatial distribution of precipitation. Orographic precipitation systems are typically shallow, do not exhibit high echo tops, and are predominantly concentrated in the lower atmospheric levels. Consequently, these systems are more frequently undersampled by operational WSR-88D radars in these areas due to beam overshooting at extended ranges [6]. Orographic rain is thus characterized by distinct microphysical properties compared to conventional winter-time stratiform rainfall. Collectively, these effects pose a substantial challenge to radar-based QPE in complex terrain.

[7] analyzed S-PROF observations during the strong El Nino winter of 1997-1998 in the coastal mountain region near Cazadero, California. Their findings revealed a substantial period of rainfall that lacked the typical radar Bright-band (BB) signature, a characteristic of winter stratiform rainfall. The study highlighted that this non bright band (NBB) rainfall differed from convective rainfall and exhibited orographic enhancement. Collocated disdrometer observations further unveiled that NBB rainfall during this period was characterized by a higher frequency of small drops and fewer large drops compared to the BB period. [8] also emphasized the contrasting nature of the drop size distribution in NBB rain periods and demonstrated an empirical radar rainfall Z-R relation at S-Band that significantly deviated from the default relations employed by the National Weather Service (NWS). In a separate investigation, [9] examined S-PROF data from HMT sites in the southeastern USA at New Bern and Old Fort during various winters. Their analysis confirmed the presence of NBB rainfall not only in mountainous coastal terrain but also in relatively flat regions where orographic forced rainfall is less likely. [10] additionally documented occurrences of NBB rainfall in California's flat central valley. These collective studies have provided conclusive evidence of NBB rainfall in flat areas surrounding coastal mountains, emphasizing the necessity for hybrid radar rainfall relations to accurately capture orographic precipitation.

The conventional approach to radar-based Quantitative Precipitation Estimation (QPE) relies on radar reflectivity (Z) to derive rainfall rates (R) [11,12]. For instance, WSR-88D radars employ specific $Z - R$ relationships tailored to distinct rainfall categories like stratiform, convective, tropical, and monsoon [13]. This methodology can be effective in regions with a consistent Drop Size Distribution (DSD) that doesn't change significantly over space and time [14]. The integration of polarimetric radar variables such as differential reflectivity (Z_{DR}) and specific differential phase (K_{DP}) has been demonstrated to enhance radar-based QPE [15]. It's been established that K_{DP}

depends on forward scattering and scales with frequency under Rayleigh scattering assumptions. Additionally, K_{DP} exhibits lower sensitivity to radar beam attenuation, ground clutter interference, and minor fluctuations in DSD compared to Z. Several studies, including [9, 14, 16], have harnessed K_{DP} for QPE at X-Band frequencies, yielding superior efficacy across various precipitation scenarios. The study by [14] showcased the potential of a K_{DP}-corrected $Z - R$ relationship, surpassing the use of K_{DP} or Z in isolation. Previous research has explored hybrid estimation methods that employ a hydrometeor classification system to guide the application of suitable rainfall estimators based on precipitation type [3, 17, 18]. However, in regions with complex terrain, particularly along coastlines, DSD exhibits substantial variability in both space and time, as noted by [7–9]. Under these conditions, the utilization of a fixed Z-R relationship can introduce significant errors due to the sensitivity of Z to DSD changes [15, 19]. While fixed $R(K_{DP})$ based rainfall measurements offer improved accuracy compared to Z-R based estimates, they too can be impacted by spatial and temporal DSD fluctuations, especially in scenarios involving orographic and stratiform rainfall. Variations in DSD dictate changes in the coefficients relating rainfall rate to different radar observables. Consequently, fixed $R(Z)$ or $R(K_{DP})$ relationships fail to adequately represent the fine-scale DSD variability.

1.2 Research Objectives

Previous research works have focused on radar-based precipitation estimation, forecasting, and the validation of numerical models in the San Francisco Bay Area [20–25]. However, an examination of radar-based Quantitative Precipitation Estimation (QPE) in this region with a particular focus on orographic rainfall remains conspicuously absent. This study's principal aim is to formulate a hybrid QPE algorithm tailored to bolster the capabilities of the Advanced Quantitative Precipitation Information (AQPI) System [26]. This algorithm is designed to take into account the impact of non Bright-band (NBB) rainfall on polarimetric rainfall rate estimators at X-Band and is anticipated to enhance the preexisting QPE products within this geographical domain.

To accomplish this goal, this study uses collocated Parsivel disdrometers and S-PROF measurements from two NOAA Hydrometeorology Testbed (HMT) sites. The Santa Rosa site is situated in the coastal plains within the Russian River valley, whereas the Middletown site is located in the neighboring mountains. Microphysical attributes of cold-season stratiform rainfall with a radar bright-band (BB) signature and orographically induced NBB rainfall are studied utilizing precipitation events spanning from the years 2016 to 2018. Drop Size Distribution (DSD) samples corresponding to rainfall conditions featuring the presence and absence of a bright band are categorized into two categories, namely BB and NBB. This delineation unveils distinct characteristics of BB and NBB rainfall, consistent with the findings of earlier investigations, as detailed previously. Subsequently, the DSD spectra serve as the basis for computing radar variables at X-Band through the employment of the T-Matrix scattering method [27]. An empirical $Z - Z_{DR}$ relationship is formulated to discriminate between these two rainfall types, rendering it applicable to real X-Band radar data. Simultaneously, corresponding polarimetric radar rainfall estimators are developed. The application of this method to X-Band radar data exhibits marked improvements in QPE when contrasted with existing operational products. This study thus contributes to the development of an accurate radar-based QPE methodology, with a special emphasis on orographic rainfall, tailored for the AQPI region. Furthermore, it aligns itself with the expanding corpus of literature dedicated to the domain of remote sensing of precipitation within complex terrains.

1.3 Organization of the Dissertation

This dissertation is structured as follows. Chapter 2 offers a detailed exploration of previous studies, highlighting the challenges involved in rainfall estimation in the complex terrain over the Bay Area. It also provides a comprehensive overview of dual-polarization radar theory, emphasizing the advantages of employing short-wavelength gap-filling radars. In chapter 3 the AQPI project is introduced, with a brief examination of the AQPI system. Chapter 4 delves into the deployment of the gap-filling X-Band weather radars in AQPI and discusses the various scientific and engineering challenges associated with radar observations in complex terrain. Next, chapter 5 presents the microphysical characteristics of stratiform and orographic rain followed by analyses of various data sets used for this research work. This chapter also underscores dual-polarization radar-based rainfall estimation algorithm development in stratiform and orographic rain along with product performance using case studies. Chapter 6 presents the development of the final AQPI QPE product which is a merged product of the X-Band based and NEXRAD based QPE. Finally, Chapter 7 offers a comprehensive summary of the QPE methodology for orographic rain as proposed in this study, including discussions on limitations and potential scope for future research.

Chapter 2

Background

2.1 Challenges of Rainfall Estimation in the Bay Area

Atmospheric rivers represent relatively narrow bands of moisture within the atmosphere, contributing to approximately 30–50% of the annual precipitation along the West Coast during a few short periods. They can cause significant damage from flooding, particularly when storms become stationary over a specific area or when the soil is already saturated. These events often present a challenge to forecasters, emergency responders, water and wastewater managers, environmental managers, and government authorities who require timely, high-resolution data for informed operational and safety-related decisions. Furthermore, given the influence of climate change, which is amplifying the region's inherent precipitation variability and pushing it to more extreme levels, the prevailing information deficiencies are poised to escalate. This phenomenon places additional strain on management systems and elevates the vulnerability of the public. Conventional NWS weather radars, originally engineered to peer into thunderstorms in the Midwest, typically struggle to provide an accurate depiction of weather patterns within California's intricate coastal mountain terrain. For context, Figure 2.1 illustrates a digital elevation map of the Californian coastline, while Figure 2.2 offers a schematic representation of the operational radar coverage within this region. Due to the topography's unique characteristics, precipitation in this area often takes shape at low atmospheric levels, beneath the detection capability of existing NEXRAD Doppler radars. Consequently, scientists are not merely concerned with estimating the amount of precipitation but also with forecasting the subsequent interactions when this precipitation reaches the ground and flows into the Bay. Therefore, one of the central elements of the AQPI project is the installation of four X-band radars and one C-band radar within this region. This augmentation aims to address the existing observational gaps and enhance the monitoring and prediction of atmospheric rivers in the San Francisco Bay Area.

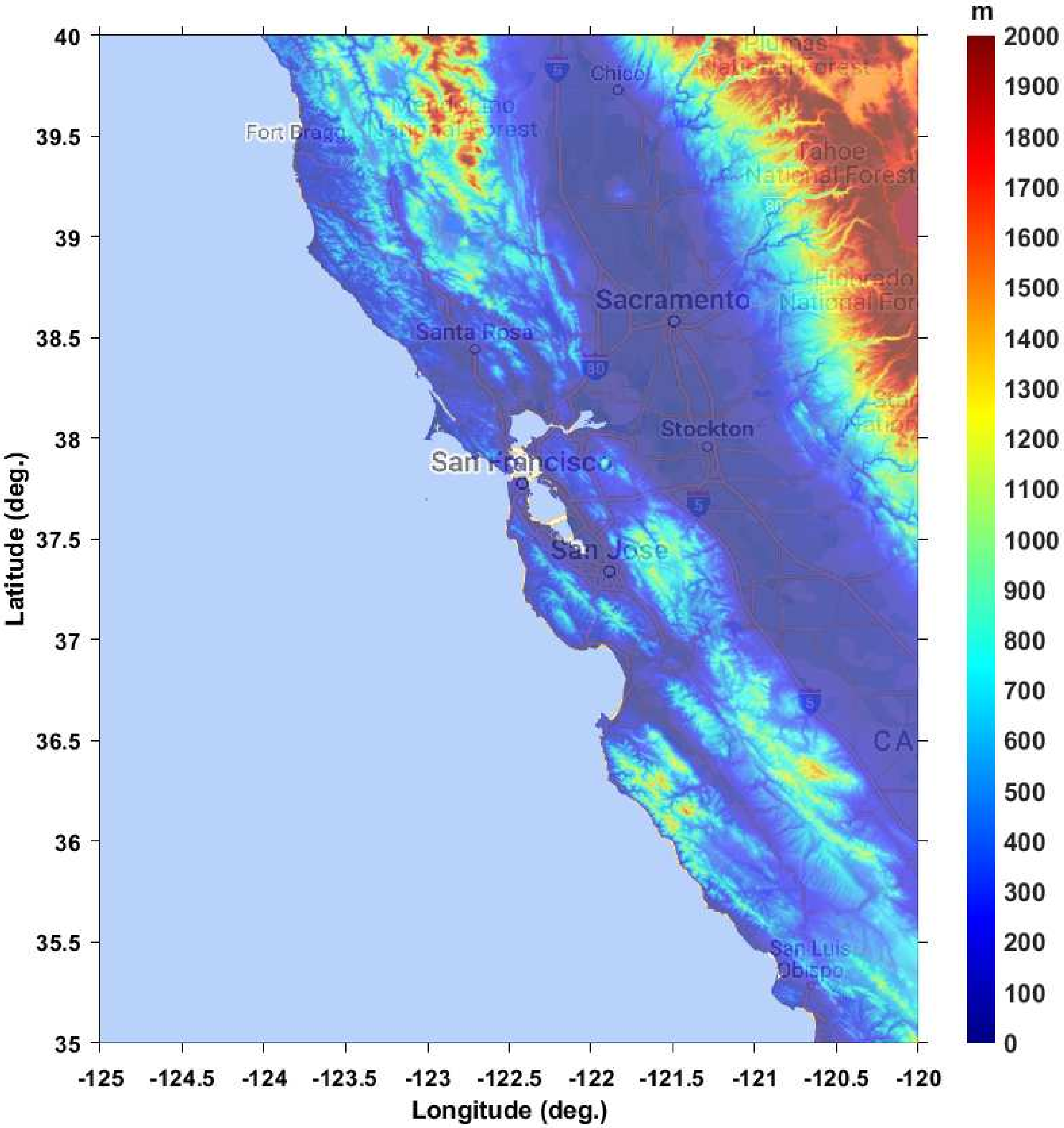

Figure 2.1: A Digital Elevation Map of the California coast showing the San Francisco Bay Area. The color map indicates the height of the terrain from the mean sea level in meters

Numerous investigations have delved into the key factors responsible for heavy rainfall and flooding episodes within the Bay Area and other regions of California. Ralph et al. (2003, 2006) [28,29] discerned a recurrent association between flooding events and the transport of moisture within the warm sector of landfalling extratropical cyclones. Notably, Ralph et al. (2003) [28]

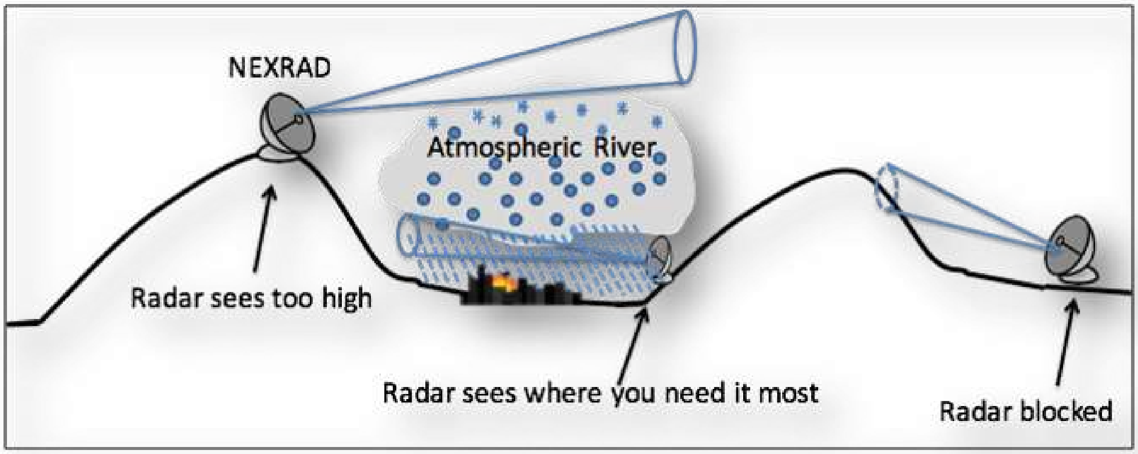

Figure 2.2: Cartoon highlighting the challenges of estimation of precipitation in complex terrain in the Bay Area. Adapted from "The Magazine for Environmental Managers, A&WMA, September 2019"

scrutinized an Atmospheric River (AR) occurrence sampled during the California Land-falling Jets Experiment (CALJET), which resulted in substantial flooding in the coastal Santa Cruz Mountains located south of the Bay Area. They underlined the pivotal roles of orographic enhancement and wind direction in dictating the extent of heavy rainfall and consequent flooding impacts. Interestingly, even slight shifts in wind direction were found to induce profound changes in both rainfall patterns and flood responses. In a complementary study, Ralph et al. (2006) [29] highlighted the significance of ARs in generating flooding events within the Russian River basin. Notably, all events reviewed in this investigation, conducted between 1997 and 2005, were invariably linked with ARs. Neiman et al. (2008) [30] harnessed a combination of satellite and ground-based data to assert that, in California at least, ARs contribute twice the volume of precipitation compared to all other meteorological systems. The ARs investigated in the Neiman et al. (2008) [30] research were characterized by anomalous warm conditions, consistent with their prevalent occurrence in the pre-frontal warm sector of extratropical cyclones. This study further revealed the role of ARs in modulating snow water equivalent (SWE), enhancing it during the fall and winter seasons, and diminishing it in the spring.

Gourley et al. (2009) [31] conducted a comprehensive examination of the complex terrains of the American River basin. Their focus was a comparative analysis of QPE derived from one WSR-88D radar and two research radars. Their inquiry aimed to unravel radar-based QPE errors, encompassing calibration correction, the Z–R relationship, and the vertical profile of reflectivity (VPR) for each radar. The current study extends the radar QPE approach to a broader expanse in Northern California, concentrating on the array of WSR-88D radars. In doing so, it addresses additional complexities, including radar data quality control, the creation of multi-radar mosaics, and the establishment of spatial continuities within rainfall products. The principal aim is to unearth inadequacies in the prevailing operational WSR-88D radar QPE and pinpoint areas amenable to enhancement. This study emphasizes radar QPE methods amenable to real-time operational application with a seamless transition into routine meteorological operations.

2.2 Operational Weather Surveillance Radars or NEXRADs

Weather radars are vital tools for monitoring and forecasting the weather worldwide. They can be deployed in various forms to meet operational and research requirements. Among these, ground-based radar is the most prevalent type, extensively employed by atmospheric scientists to predict weather conditions in numerous countries globally. These radar systems offer real-time insights into incoming weather phenomena across extensive geographical expanses [15, 32]. One of the most extensive deployments of ground-based weather radars is the Weather Surveillance Radar–1988 Doppler (WSR-88D) S-Band radar network in the United States. This network, commonly known as Next Generation Radar (NEXRAD), plays a pivotal role in operational weather forecasting, particularly in early storm warning and event prediction [33]. It is an integral component of the U.S. storm prediction and forecasting system, providing critical data for the detection of tornadoes and severe weather occurrences [34, 35]. Moreover, the data gathered by these radar systems significantly contributes to numerous numerical weather prediction models, enhancing their capability to forecast weather conditions over extended temporal ranges [36].

In recent years, the NEXRAD system has undergone considerable enhancements, notably the incorporation of dual-polarization capabilities. This advancement has increased the accuracy and efficacy of the system across its operational facets [37]. The upgraded system delivers comprehensive information regarding precipitation types, encompassing the detection of diverse hydrometeor species. This enhancement not only improves forecast accuracy but also plays a crucial role in safeguarding lives and property [38, 39]. In summary, the NEXRAD system has been pivotal in the progress of weather research, enabling scientists to delve into the intricacies of the atmosphere and develop novel technologies for augmenting weather forecasting proficiency. Its utility extends beyond weather prediction, influencing other domains like aviation, agriculture, and transportation.

Westrick et al. (1999) [40] conducted a comprehensive review focusing on issues about the density of the NEXRAD network and the minimum scanning elevation angle within numerous flood-prone watersheds along the U.S. West Coast. In the Bay Area, two NEXRADs, KMUX and KDAX, provide radar coverage. However, KMUX is located in the Santa Cruz mountains at an elevation exceeding 1000 m, distant from sea level regions of the Bay Area. This results in a radar beam at a considerable height (approximately 2 km above ground level) with substantial width (exceeding 1 km). Consequently, this radar is inadequate for accurately resolving precipitation patterns at an urban scale. KDAX, located closer to sea level but near Davis, CA, over 80 km from certain parts of the Bay Area, encounters partial radar beam blockage at low elevation angles. In addressing weather coverage issues over the offshore vicinity near San Francisco, NOAA conducted an evaluation using a combination of ground-based and aircraft data during the late 1990s and early 2000s (Reynolds 1995; White et al. 2003; Matrosov et al. 2005). These assessments exposed the occurrence of shallow Non Bright-band (NBB) rainfall, often below the scanning level of the KMUX NEXRAD. Matrosov et al. (2005) [41] employed transportable X-band radar measurements to observe precipitation at low levels typically overlooked by NEXRAD. The X-band QPE focused on the offshore region adjacent to the City of San Francisco, delivering detailed precipitation mapping near the surface. These studies underscore the significance of shallow rainfall in the Bay Area and emphasize that the NEXRAD radar frequently overshoots or is obstructed from detecting these low-level precipitation occurrences. Consequently, radar sampling and analytical strategies tailored to the distinctive features of the urban environment are indispensable in the Bay Area.

2.3 Essential Principles of Dual-Polarization Weather Radars

Atmospheric remote sensing by radars is based on the principle of scattering of electromagnetic energy by particles in the atmosphere. The radar transmits a series of electromagnetic pulses and receives back-scattered energy from targets. This scattered energy is measured as voltages recorded by the radar antenna. This measured power is further sampled and digitized at the receiver end to generate in-phase and quadrature-phase signals commonly known as IQ data. Next, various advanced digital signal processing techniques are leveraged to filter ground clutter and correct second-trip echoes. A detailed theory on the working principles and signal processing of weather radars is given in [42]. The targets of interest for a weather radar are meteorological scatterers that comprise hydrometeors either in the solid or liquid state. Recent advancements have enabled radars to transmit and receive electromagnetic energy using orthogonal polarization. The type of polarization is determined by the direction of the variation of the electric field vector in time with respect to the direction of propagation of the wave. Polarization can be of several types namely linear (horizontal/vertical/slant), elliptical, and circular. The most common polarization mode used in weather radars is linear. All weather radars in the continental USA have been upgraded to support dual polarization at orthogonal states. A significant advantage of dual polarization over single polarization lies in retrieving detailed information on hydrometeors such as types, shapes, sizes, and orientations. The fundamental quantities that a Doppler radar measures are known as radar moments. These are reflectivity, Doppler velocity, and spectrum width. In dual-polarization systems, additional polarimetric variables such as differential reflectivity, differential propagation phase, co-polar/cross-polar correlation coefficient, linear depolarization ratio, etc are derived from the complex power and phase measurements from the orthogonal channels. Mathematically, dual-polarization variables can be expressed in terms of the drop size distribution (DSD).

2.3.1 Drop Size Distribution

In the field of remote sensing and meteorology, the targets of interest are different types of hydrometeors. They can be rain, hail, snow, graupel, ice crystals, dendrites, and so on and so forth. These hydrometeors are the result of precipitation by the clouds in the atmosphere and they vary in shape and size. Understanding particle size distribution along with scattering microphysics is of fundamental importance in determining the characteristics of precipitation and its estimation. The natural variability in drop size distribution (DSD) of rain can be sufficiently described by a gamma distribution. This has been shown by Ulbrich in 1983. Testud showed that the gamma DSD model can be expressed in a normalized form which is

$$N(D) = N_w f(\mu) \left(\frac{D}{D_o}\right)^{\mu} e^{-\Lambda D} \tag{2.1}$$

where

$$\Lambda = \frac{3.67 + \mu}{D_o} \tag{2.2a}$$

$$f(\mu) = \frac{6}{3.67^4} \frac{(3.67 + \mu)^{\mu+4}}{\Gamma(\mu + 4)} \tag{2.2b}$$

$N(D)$ $(mm^{-3}m^{-1})$ is the number of drops per unit volume per unit diameter of size interval D (mm) and D+Δ D(mm), N_w $(mm^{-3}m^{-1})$ is called the normalized intercept parameter of an equivalent exponential DSD which has the same water content as the gamma DSD. μ is the shape parameter, and Λ (mm^{-1}) is the slope parameter. D_o (mm) is the median volume diameter in (mm) which is defined such that drops up to size D_o contribute to half the rainwater content. Γ () represents gamma function. Thus μ, D_o, and N_w are the 3 most important parameters of the drop size distribution which controls the shape of the curve.

2.3.2 Radar Moments Calculation

The most fundamental parameter, radar reflectivity, can be derived from a given drop size distribution. Other parameters namely differential reflectivity and specific differential phase shift can also be expressed as different moments of the gamma distribution. Reflectivity at the horizontal polarization denoted by Z_h can be calculated as

$$Z_h = \frac{\lambda^4}{\pi^5|K_w|^2}\int_D |S_{hh}(r,D)|^2 N(D)dD \tag{2.3}$$

Here, $Shh(r,D)$ is the back-scattering cross section at horizontal polarization, K_w is the dielectric constant of water, λ is the radar wavelength, d is the drop diameter and r is the distance of the drop with respect to radar. The reflectivity is also known as the water equivalent reflectivity factor since in the calculation, the dielectric constant of water is used as apriori information of the target hydrometeor is not known. In the Rayleigh scattering regime, the back-scattered cross section is proportional to D^6. The equation 2.3 can be simplified to

$$Z = \int_D N(D)D^6 dD \tag{2.4}$$

Thus the reflectivity factor can be approximated as the $6^t h$ moment of the DSD. This is also known as the Rayleigh approximation. Generally, S-Band radars operate at 2.7 GHz which falls under this regime. It should be noted that at higher frequencies the scattering regime falls in the non-Rayleigh or Mie region where this approximation is not valid. The differential reflectivity is denoted by Z_{dr} is calculated as

$$Z_{dr} = \frac{\int_D |S_{hh}(r,D)|^2 N(D)dD}{\int_D |S_{vv}(r,D)|^2 N(D)dD} \tag{2.5}$$

It can be noticed that Differential reflectivity is independent of the number of drops but depends directly upon the drop axis ratio. Another measured parameter is called the differential phase and is denoted by Φ_{dp}. As the pulse propagates through the medium, the cumulative change in phase between horizontal and vertical polarization is given by Φ_{dp}. The radar cannot directly measure the differential phase. It rather measures Ψ_{dp} which not only considers the forward propagation phase change but also the back-scatter differential phase δ_{co}.

$$\Psi_{dp}(r) = \Phi_{dp}(r) + \delta_{co}(r) \tag{2.6}$$

Differential Phase (Φ_{dp}) can also be expressed as the range derivative of Specific Differential Phase denoted by K_{dp}.

$$\Phi_{dp}(r) = \int_0^r K_{dp}(r)dr + \delta_{sys} \tag{2.7}$$

Here δ_{sys} is a constant term that denotes the built-in system phase. This is usually an adjustable parameter and is often considered 0 in calculations.

$$K_{dp} = \frac{2\pi}{k_0}\Re\int_D N(D)\left[\hat{h}\cdot\vec{f}(r,D) - \hat{v}\cdot\vec{f}(r,D)\right]dD \tag{2.8}$$

The specific differential phase can be expressed in terms of forward scattering amplitude at both polarizations.

2.4 Advantages of X-Band radars

The radar's sampling volume primarily depends on the transmitted pulse width, antenna beamwidth, and radar range. For an ideal uniformly illuminated parabolic reflector, the sampling resolution is given by the following:

$$Resolution\ volume\ length = c\tau/2 \tag{2.9a}$$

$$Resolution\ volume\ width = R\theta \tag{2.9b}$$

where c is the speed of light; T is the transmitted pulse width typically in the order of μs, R is the range from radar, and θ is the half-power beamwidth. In the case of a parabolic dish antenna, the beam width is directly proportional to the wavelength λ and inversely proportional to the antenna diameter d. McLaughlin et al. (2009) [43] suggested that a practical antenna size for unobtrusive deployment falls in the range of 1 to 1.5 meters. Assuming the NEXRAD radar system's frequency, operating a 1-meter antenna would yield a resolution cell width of 3 kilometers at a 30-kilometer range. At this resolution, fine-scale weather phenomena such as convective cells, tornadoes, and microbursts cannot be adequately resolved. Each NEXRAD radar system is equipped with a large 9-meter diameter antenna. However, the non-overlapping coverage of NEXRAD radars results in significant spacing between radars, approximately 230 kilometers in the eastern United States and almost 400 kilometers in the western United States. As the radar range increases, the illuminated volume expands significantly. Moreover, due to the Earth's curvature and terrain obstruction, over 70% of the atmosphere below 1 kilometer above ground level (AGL) remains unobservable. From a temporal resolution perspective, NEXRAD radars operate with predefined volume coverage patterns (VCP). The update rate decreases as the number of elevation angles in the VCP increases. For instance, using the commonly used VCP12 precipitation mode with 14 tilts (increasing elevation angles from 0.5^o to 19.5^o) takes 5 to 6 minutes to complete a volume scan. This time frame is insufficient to capture rapidly evolving, small-scale meteorological events like urban flash floods. Additionally, deploying and maintaining large, high-power radars like those with 12-meter radomes is costly and operationally complex. Transitioning to a shorter wavelength, such as the X band, allows for higher spatial resolution with smaller antennas. These compact systems can be easily deployed on small towers, rooftops, or existing infrastructure. Compared to the NEXRAD radars, X-band radar systems offer higher temporal resolutions and lower power requirements. Consequently, low-cost, low-power X-band radar systems have garnered increasing interest in recent years. To address the limitations of the NEXRAD radar coverage and resolution, the AQPI project proposed deploying four X-band radars to create a network in the Bay Area. X-Band radar systems outperform individual NEXRAD radars in terms of update rates on key weather features, beam height, and spatial resolution (Junyent and Chandrasekar 2009) [44]. Overcoming inherent challenges in transitioning to X-Band radar involved developing technical solutions for issues such as attenuation and range velocity ambiguity. Research has shown that attenuation can be addressed using dual-polarization based attenuation correction techniques [45,46]. Range velocity ambiguity can be mitigated using advanced pulsing schemes and signal processing [47]. Additionally, special attention is required for clutter suppression during short-range operations in urban areas. In summary, the AQPI X-Band radar network has successfully implemented all significant technical initiatives, primarily emphasizing the transition from research to operational applications in the domain of urban weather monitoring and alert systems.

Chapter 3

AQPI: Advanced Quantitative Precipitation Information

In the western United States, the significance of winter-time precipitation cannot be overstated. This region heavily relies on Atmospheric Rivers (ARs), which are concentrated water vapor transport bands often associated with land-falling extra-tropical cyclones. Interestingly, nearly half of California's yearly precipitation results from a handful of intense AR events, according to [48]. These ARs, with their heavy downpours, present a dual-edged sword for Californians. While they offer respite to drought-stricken areas, their concentrated deluge, which can occur in a span of just a few days, poses a serious flooding threat, putting lives and property at risk. An alarming statistic reveals that ARs are responsible for more than 80% of the flood damages in the western U.S., with an annual cost averaging over $1 billion [49]. The San Francisco Bay Area is particularly susceptible to the havoc that ARs can wreak [49]. Recent history provides examples, such as the series of rain events in February 2017. These led to catastrophic flooding in San Jose, as Coyote Creek breached its banks, displacing 14,000 residents. The same weather system caused substantial damage to the Oroville Dam spillway, necessitating the evacuation of nearly 200,000 residents downstream [50]. The cumulative financial toll of the February 2017 storms surpassed $1.5 billion [51]. In 2019, another sequence of rainfall events in the Bay Area resulted in over $150 million in flood damages and a presidential disaster declaration [52]. Moreover, landslides are another imminent danger. [53] demonstrated that the vast majority of landslides in the San Francisco Bay area were directly linked to ARs. The region's intricate terrain and proximity to the San Francisco Bay make it especially vulnerable to flooding events. The predicament is further exacerbated by flash floods along inland rivers and creeks, which drain numerous small watersheds and when coupled with coastal flooding along the bay shoreline, create compound flooding events.

Urbanization in the region plays a pivotal role in compounding the challenges. Home to more than seven million residents, spanning nine counties and encompassing major cities like San Francisco, Oakland, and San Jose, the Bay Area is densely populated. A disconcerting report from the California Department of Water Resources (CA-DWR, 2013) disclosed that nearly 400,000 people in the region are living in the 100-year floodplain, facing elevated risks. Impervious surfaces and stormwater runoff further exacerbate flooding conditions. The consequences of urban flooding are multifaceted, spanning from compromised water quality in the Bay to inundated roadways and buildings during storms. The situation is expected to worsen due to sea-level rise and continuous urban development.

To address these challenges, the region needs precise monitoring and forecasting of extreme rain and flooding. While existing weather monitoring infrastructure, including satellites, off-shore observations, and the operational radar network [34], offers a measure of preparedness, it often falls short in providing the required specificity for timely mitigative actions. The primary reason is that precipitation frequently forms or intensifies at very low atmospheric levels, beyond the capability of the existing NEXRAD network to detect effectively. Orographic lifting and warm rain collision-coalescence processes in the complex terrain are contributing factors [7]. Furthermore, the radar observations in the Bay Area are obstructed by coastal mountains, creating substantial blind spots in the surveillance network. To overcome these limitations, the California Department of Water Resources (CA-DWR) and the U.S. Department of Energy have embarked on an innovative approach. They have invested in creating an 'atmospheric river observatory picket fence' (AROs) along the U.S. West Coast. These AROs, crafted by the National Oceanic and Atmospheric Administration Physical Sciences Laboratory (NOAA-PSL), offer crucial data on wind and temperature profiles, column-integrated water vapor, onshore moisture flux, and freezing elevation at seven coastal sites and two inland locations [54, 55]. They have significantly improved forecasting and serve as vital tools for water resource managers, helping them gauge the intensity of an AR event right at the ARO location. However, AROs have their limitations; they do not function like traditional weather radar systems but instead provide a detailed view of the atmosphere directly above them.

To bridge this gap and detect variations in storms across different watersheds, a scanning radar system was temporarily deployed in Santa Clara, CA, with support from NOAA. This initiative, preceding the AQPI Project, showcased superior high-resolution rainfall estimates [20]. The Advanced Quantitative Precipitation Information (AQPI) Project, awarded by CA-DWR to NOAA and collaborating partners in 2017, is now administered by the Sonoma Water Agency. This groundbreaking initiative aims to provide more precise measurements and forecasts of precipitation, streamflow, and coastal flooding within the San Francisco Bay area. The project's inception can be traced back over a decade, rooted in fundamental research that sought to enhance our understanding of hydrometeorological processes [7, 41, 56, 57]. A unique feature of AQPI is its collaborative approach, bringing together local, state, and federal agencies, and research institutions. The array of agencies involved includes NOAA Physical Sciences Laboratory (PSL), NOAA Global Systems Laboratory (GSL), NOAA Cooperative Institute for Research in the Atmosphere (CIRA), NOAA Cooperative Institute for Research in Environmental Sciences (CIRES), USGS Pacific Coastal and Marine Science Center, NOAA National Severe Storms Laboratory (NSSL), Colorado State University Department of Economics, Scripps Institute of Oceanography, California Department of Water Resources (CA-DWR), Sonoma Water (SCWA), Valley Water (SCVWD), San Francisco Public Utilities, Contra Costa County, East Bay Municipal, Alameda County, Napa County, Marine County, and the National Weather Service (NWS). This united effort strives to provide solutions to the complex water management and flood response needs of the Bay Area.

3.1 AQPI Components

AQPI incorporates a combination of integrated observations and high-resolution model forecasts to monitor storm systems and predict precipitation, streamflow, and coastal flooding across the Bay area, as illustrated in Figure 3.1. As mentioned earlier, AQPI's observational framework extends from an existing network established by NOAA, CA-DWR, Scripps Institute of Oceanography, San Jose State, and Sonoma Water, which is dedicated to monitoring extreme precipitation events in California. The coastal modeling component further leverages prior research efforts conducted in and around the San Francisco Bay region by the USGS and their research partners [58–60]. The fundamental basis of AQPI's observational network consists of the incorporation of new radar systems, encompassing four X-band and one C-band radar installations, as delineated in Figure 3.2.

These radar systems are meticulously designed to complement NEXRAD coverage in the vicinity of the Bay area, substantially enhancing the precision of quantitative precipitation estimation (QPE). Initial evaluation has revealed that QPE data derived from AQPI radar installations exhibit superior accuracy and contribute to enhanced streamflow simulations compared to NEXRAD [20, 61]. Notably, the AQPI radars excel in the identification of narrow cold frontal rainbands (NCFRs) in specific regions of the Bay Area, which may not be adequately observed by NEXRAD, as visually represented in Figure 3.3. NCFRs are characteristic rainbands that frequently manifest along the cold frontal boundaries of extratropical cyclones, giving rise to high-intensity precipitation rates [62]. These weather phenomena are often responsible for flash floods and hazards like debris flows [63,64]. As of now, two X-band radar systems have been successfully installed and are operational, as denoted in Figure 3.2. The progress of installing the remaining X-band radar units and the C-band radar has been impeded by a confluence of factors including the pandemic, wildfires, and power outages. However, it is anticipated that these installations will be completed by the middle of 2024.

Furthermore, there exists a data repository that includes information sourced from pre-existing station networks, readily accessible to a wide audience, such as the Hydrometeorological Automated Data System (HADS) [65]. This encompasses data from the recently introduced surface meteorological and precipitation profiling radar stations, part of NOAA/PSL's contributions to AQPI, and another comprehensive statewide observational initiative supported by CA-DWR [66]. Additionally, the repository encompasses data from station networks operated by local entities that were formerly restricted to individual water agencies. The seamless aggregation of station data is facilitated through the NOAA Meteorological Assimilation Data Ingest System (MADIS) [67], harnessing MADIS's robust integration and quality control mechanisms, thus ensuring data standardization across all datasets. In addition to observational data, forecast models play a pivotal role in predicting precipitation, streamflow, and coastal flooding dynamics within the AQPI domain. The extent of model coverage is depicted in Figure 3.4.

3.2 AQPI System

The AQPI system is an integration of comprehensive observation and model datasets, delivering them in user-friendly formats with tailored threshold alerts, thereby serving as a valuable resource for informed decision-making. The development of this system was supported by extensive collaboration with local water management agencies, which played an instrumental role in defining the specific requirements and demands for data related to precipitation, streamflow, and coastal flooding. To garner insights into geographic areas of concern and determine the requisite threshold values for precipitation, streamflow, and coastal water levels, the AQPI research team engaged in a series of in-person consultations with representatives from various Bay Area water agencies. These agencies, each with distinct missions and operating within diverse regions characterized by variations in land use, terrain, and proximity to the bay, articulated their unique needs. The outcome of these consultations culminated in a comprehensive catalog of requirements that ultimately served as the blueprint for the AQPI system's design. A case in point is the San Francisco Public Utilities (SFPUC), which is particularly focused on assessing the potential flooding repercussions stemming from water discharges at Lower Crystal Springs Reservoir into San Mateo Creek, especially in the vicinity of Highway 101 where the creek converges with the Bay. The forecasts regarding Bay water levels from the Coastal Storm Modeling System (CoSMoS) will play a pivotal role in guiding SFPUC's decision-making process concerning reservoir outflows.

As previously highlighted, a key motivation behind the AQPI system is to aggregate essential information concerning precipitation, streamflow, and coastal water levels in the Bay area. To achieve this objective, the Meteorological Assimilation Data Ingest System (MADIS) serves as a crucial tool for the collection and dissemination of data within the AQPI domain. The inclusion of local data carries an added advantage, as it allows for the bias correction of Multi-Radar Multi-Sensor Quantitative Precipitation Estimation (MRMS QPE) products by leveraging the precipitation data available through MADIS. To date, an impressive total of 295 local network stations have been incorporated into the MADIS system, extending data accessibility to 13 water agencies in the Bay Area.

Users are provided access to model forecast data sourced from the High-Resolution Rapid Refresh (HRRR), Global Forecast System (GFS), National Water Model (NWM), and CoSMoS, all tailored to their respective areas of interest. This information can be harnessed independently to foster situational awareness or can be employed to drive localized models. For instance, in Santa Clara County, radar data is employed for real-time storm monitoring to identify potential flood-prone areas. In Contra Costa County, NWM data acts as an input for the Hydrologic Engineering Center River Analysis System (HEC-RAS) model to inform assessments of flows in areas of concern. Moreover, the SFPUC Wastewater enterprise leverages AQPI HRRR forecasts to anticipate 18-hour rainfall accumulation across various sectors of the city and to flag short-duration periods (1 hour) marked by projected rainfall rates exceeding flood return period criteria. The ultimate aim is to extend the reach of this information down to the neighborhood level, enabling a more precise identification of areas within the city vulnerable to flooding during rain events. The radar data within the AQPI system is instrumental in generating Quantitative Precipitation Estimation (QPE) and Nowcast products. Furthermore, it is shared with the National Severe Storms Laboratory and amalgamated with NEXRAD data in the developmental phase of the MRMS product. Ongoing efforts are concentrated on transitioning AQPI data into the operational version of MRMS to facilitate its assimilation by the operational HRRR model.

The AQPI graphical user interface has been meticulously designed to furnish users with real-time access to model and observational data, offering customization to align with the distinct requirements of each water agency. Users have the flexibility to select the specific products of interest corresponding to their geographic regions of concern, while also being able to establish predefined thresholds for precipitation, streamflow, and coastal flooding. The interface empowers users to visualize and download real-time AQPI observation and model data, ensuring access to the most current information.

3.3 AQPI Products

The AQPI includes a diverse array of products, drawing from both observational data and model forecasts, as comprehensively outlined in Table 3.1. These products cater to the specific needs of water agencies, tailored to their respective regions of interest, and encompass model forecasts related to precipitation, streamflow, and coastal water levels, sourced from the modeling systems delineated earlier. Additionally, several products are generated from observations, with a prominent focus on Quantitative Precipitation Estimation (QPE) and Nowcast. The QPE product, a pivotal component of AQPI, uses AQPI radar data, wherein the X-band radar systems provide coverage, and Multi-Radar Multi-Sensor Quantitative Precipitation Estimation (MRMS) data to account for the remainder of the domain. The AQPI radar QPE methodology builds upon the principles elucidated in [68], leveraging optimal radar rainfall estimators informed by both reflectivity and specific differential phase measurements. This approach is guided by the classification of rainfall types, distinguishing orographic from stratiform precipitation, as expounded in [68]. Furthermore, it incorporates a sophisticated algorithm to mitigate bright band contamination, a key concern in radar-based precipitation estimation. In regions beyond the coverage of the AQPI radar network, the MRMS radar-only QPE is employed to complete the QPE dataset. The QPE product offers both 15-minute and hourly precipitation estimates, with a remarkable update frequency of two minutes. For an in-depth exploration of the QPE products, comprehensive details are presented in subsequent chapters.

The AQPI real-time nowcast system leverages the Dynamic and Adaptive Radar Tracking of Storms (DARTS) tool, a solution introduced by Ruzanski et al. in 2011, to extrapolate radar-based observations of precipitation (QPE) for the forthcoming 60 minutes. DARTS operates as an area-based nowcast tool, employing the solution of the field flow equation in the frequency domain. Fast

Table 3.1: Description of AQPI products.

AQPI Product	**Input**	**Description**
Precipitation and near-surface temperature forecasts	HRRR+GFS	Hourly forecast out to 18-h updated each hour with HRRR; GFS forecast appended to end of each 18-h HRRR forecast out to 120-h at 3-h intervals to 90-h and 6-h intervals from 90-h to 120-h; GFS updated every 6-h
Streamflow forecasts	NWM	Hourly forecast out to 18-h updated each hour
Coastal water level forecasts	CoSMoS	Hourly forecast out to 18-h using the latest HRRR forecast and using latest NWM forecast
QPE	AQPI and MRMS RadarOnly QPE	15-min and 60-min rainfall accumulation updated every 2 min
Nowcast	MRMS RadarOnly QPE	Precipitation nowcast out to 60-min updated every 2 min

computations are achieved through the application of a Fast Fourier Transform (FFT) technique. At present, the AQPI real-time nowcast system utilizes the MRMS radar-only QPE product to generate nowcasts. Future iterations will incorporate a fusion of AQPI and NEXRAD data to further enhance forecasting accuracy.

Beyond CoSMoS-derived water level forecasts in the Bay area, AQPI provides graphical representations of coastal flood inundation sourced from CoSMoS. These visualizations encompass critical information, including water levels referenced to the North American Vertical Datum of 1988 (NAVD88), water depth referenced to a recent Digital Elevation Model (DEM) [69], and key wave parameters. The wave data encompasses details on wave height, period, and direction, offering valuable insights for assessing the risk of wave-driven overtopping of adjacent levees or seawalls. Additionally, although not presented as graphical displays, depth-averaged currents can be obtained from the outputs, further enriching the comprehensive dataset available within AQPI.

3.4 Deployment of AQPI surface instruments

As a crucial element of the AQPI initiative, an advanced system has been meticulously developed, featuring cutting-edge X-Band dual-polarization radars and sophisticated surface observational instruments [20,26]. The AQPI's extensive domain spans a vast area covering the majority of flood-prone watersheds within the Bay Area. Notably, recent additions include the deployment of two high-performance X-band radars, XSCW and XSCV, located strategically in Santa Rosa and Santa Clara, respectively. These innovative radar installations are poised to significantly enhance the existing NEXRAD network's coverage, providing invaluable insights into the intricacies of rainfall processes. This research investigation is tailored to address the coastal region of California, with a primary focus on the San Francisco Bay Area. Remarkably, this region plays a pivotal role in the National Oceanic and Atmospheric Administration's (NOAA) Hydrometeorology Testbed (HMT) program. The HMT program is collaboratively managed by NOAA's Physical Sciences Laboratory (PSL) within the Office of Oceanic and Atmospheric Research (OAR) and the Weather Prediction Center of the National Weather Service (NWS). It boasts a network of ground-based observation sites strategically positioned throughout this locale. Within this network, a majority of these sites are equipped with precision-engineered tipping bucket rain gauges and cutting-edge optical disdrometers. Select sites are further equipped with vertically oriented S-Band Profiler Radars (S-PROF) and Snow Level Radars (SLR), further amplifying the observational capacity of this expansive network.

Table 3.2: NOAA PSL surface instrumentation sites

Station ID	Lat.	Lon.	Elv. (MSL)
STR	$38.5154^o N$	$122.8022^o W$	$32 m$
MDT	$38.7456^o N$	$122.7112^o W$	$972 m$
LGS	$37.2615^o N$	$122.1328^o W$	$777 m$

Figure 3.5a depicts a topographical map of the Santa Rosa region, highlighting the positions of the XSCW X-Band radar and NOAA PSL surface instrumentation sites. In the figure, the radar observation ranges are denoted by black circles, ranging from 0 to 40 km with increments of 10

km. The red crosses symbolize the presence of two key NOAA PSL sites, known as STR, situated in Santa Rosa, and MDT, located in Middletown. Both of these sites are equipped with an array of instruments, including S-PROF, Parsivel disdrometers, and surface observation gauges. Figures 3.5b and 3.5c offer insights into the XSCW radar beam's trajectory, specifically in the line of sight azimuth direction towards the two PSL sites. These images provide details on the azimuth and the distance separating the radar's location from the ground sites. Of particular interest is the proximity of the STR site to the radar, located within the valley, and the placement of the MDT site in the mountains near the eastern boundary of the watershed, creating a distance of 27 km between these two sites.

In a manner similar to Figure 3.5, an illustration of the PSL site located within the coverage area of the XSCV radar in the Santa Clara region is shown in Figure 3.6. This specific site is situated in Los Gatos at an elevation of approximately 777 meters above Mean Sea Level (MSL). Like the aforementioned sites, this location is equipped with a range of observation instruments, including a precipitation gauge, optical disdrometers, and a Snow Level Radar (SLR), in addition to other surface measurement devices. For comprehensive geographical coordinates and site elevation information of all NOAA PSL sites falling within the X-Band radar domains, please refer to Table 3.2.

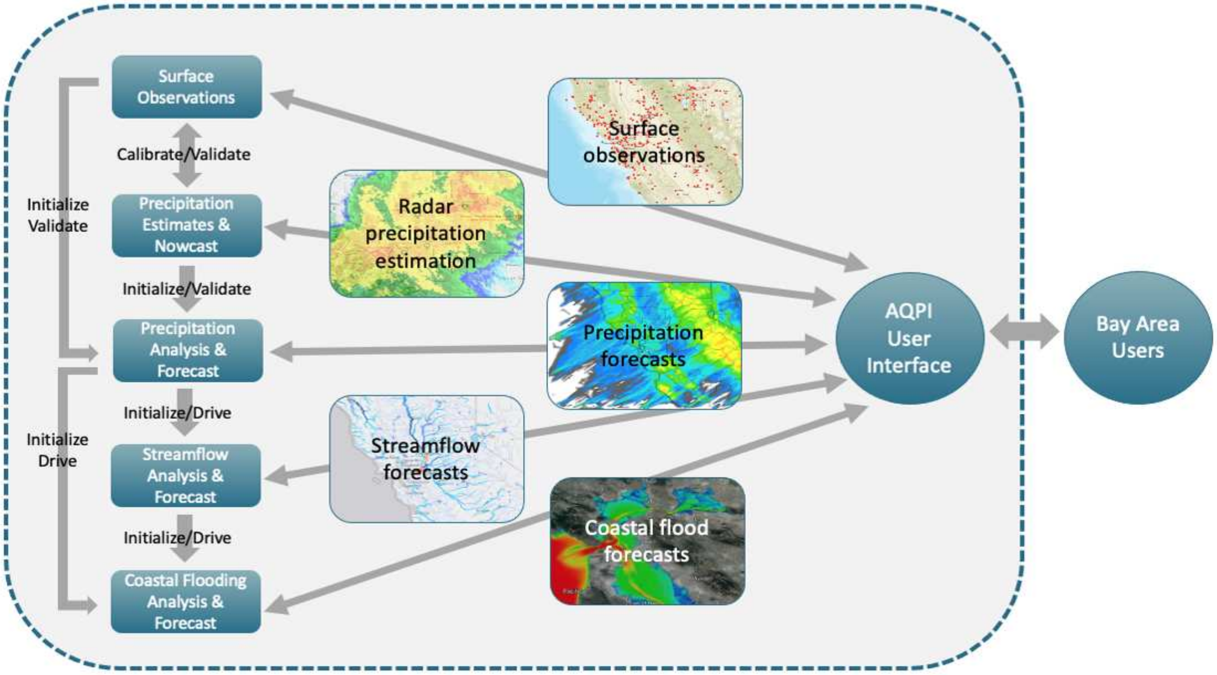

Figure 3.1: Components of AQPI and the flow of information to and from the AQPI system User Interface and Bay Area users. Image reference Cifelli et al. (2022) [1]

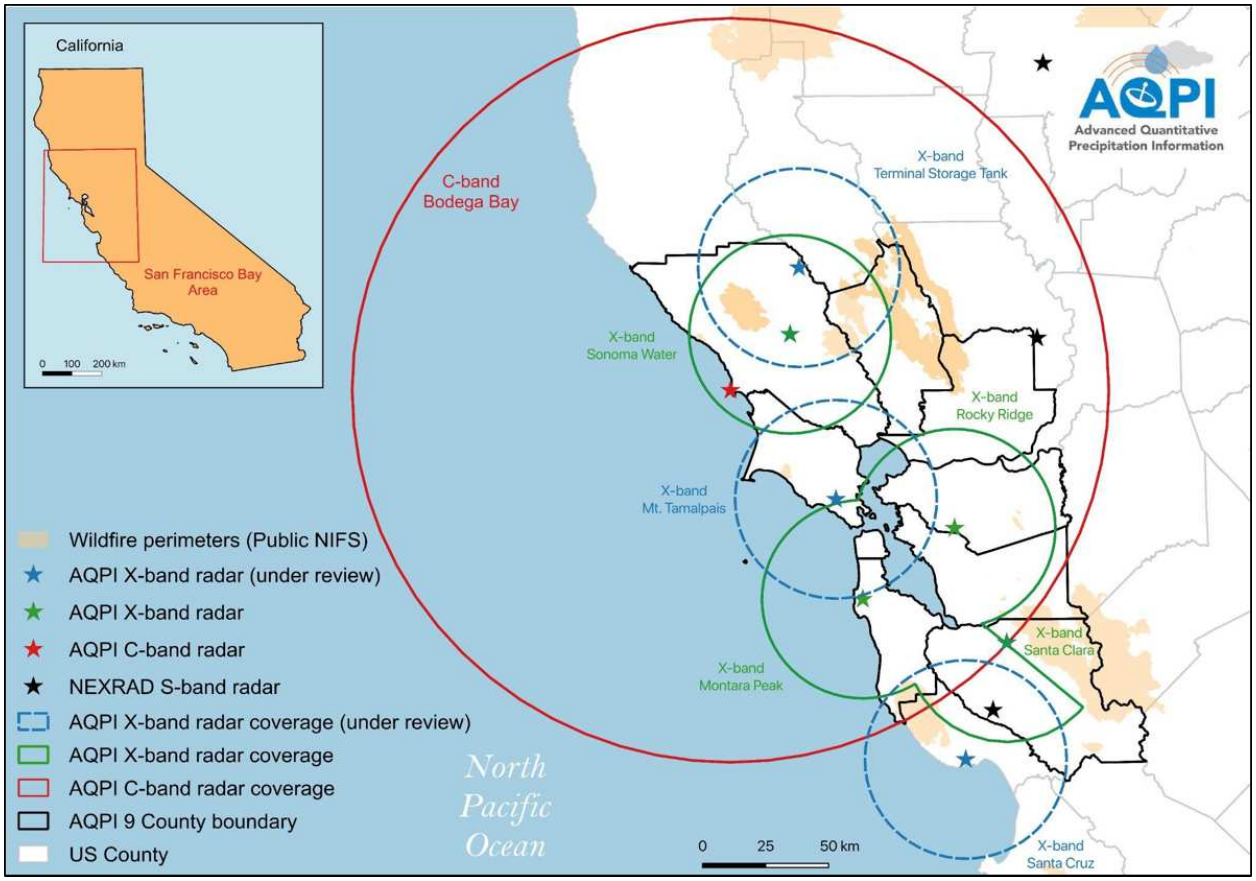

Figure 3.2: Location of the radar network for AQPI. X-band systems are shown in green with the circles indicating a 40 km range of coverage. The proposed C-band location is shown in red with the circle indicating a 100-km range of coverage. The blue dashed lines indicate additional X-band systems that have been supported by other funding agencies and will be integrated into AQPI in the near future. Image reference Cifelli et al. (2022) [1]

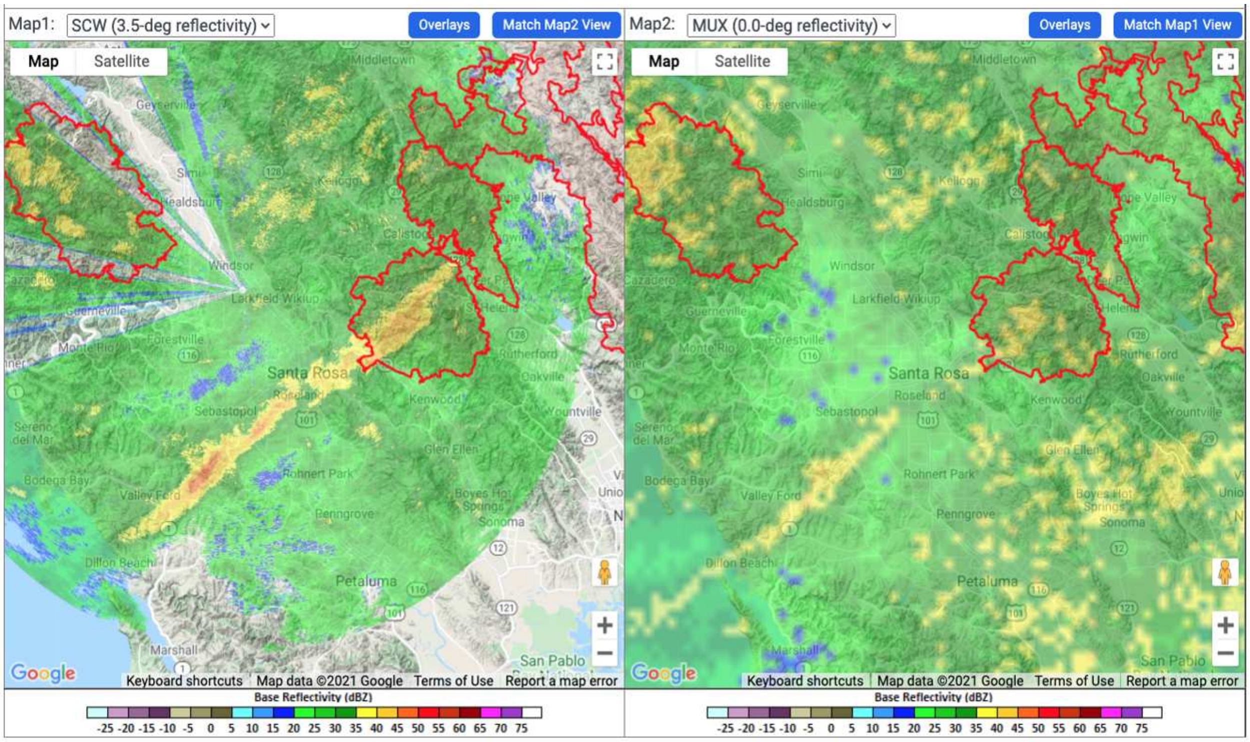

Figure 3.3: Comparison of radar reflectivity from (a) AQPI XSCW X-Band Radar and (b) KMUX NEXRAD during an AR event observed at 18:46 UTC on 24 October 2021. The narrow ribbon of high radar reflectivity near Santa Rosa in the center of each image represents an NCFR. Areas outlined in red represent recent burn scars. Image reference Cifelli et al. (2022) [1]

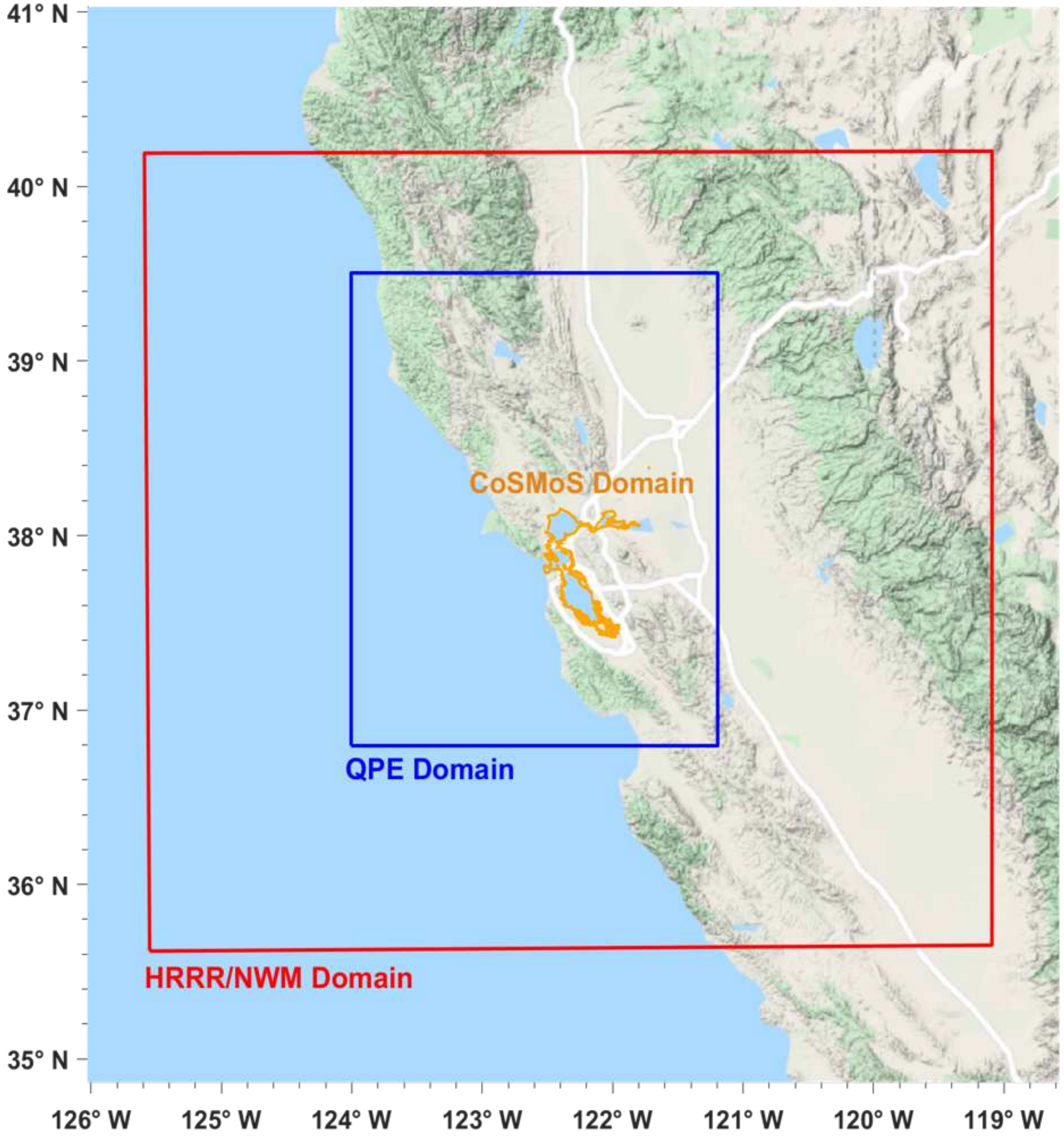

Figure 3.4: Domain of coverage for modeling components of AQPI: HRRR/NWM, QPE and CoSMoS domains are shown in red, blue, and orange respectively.

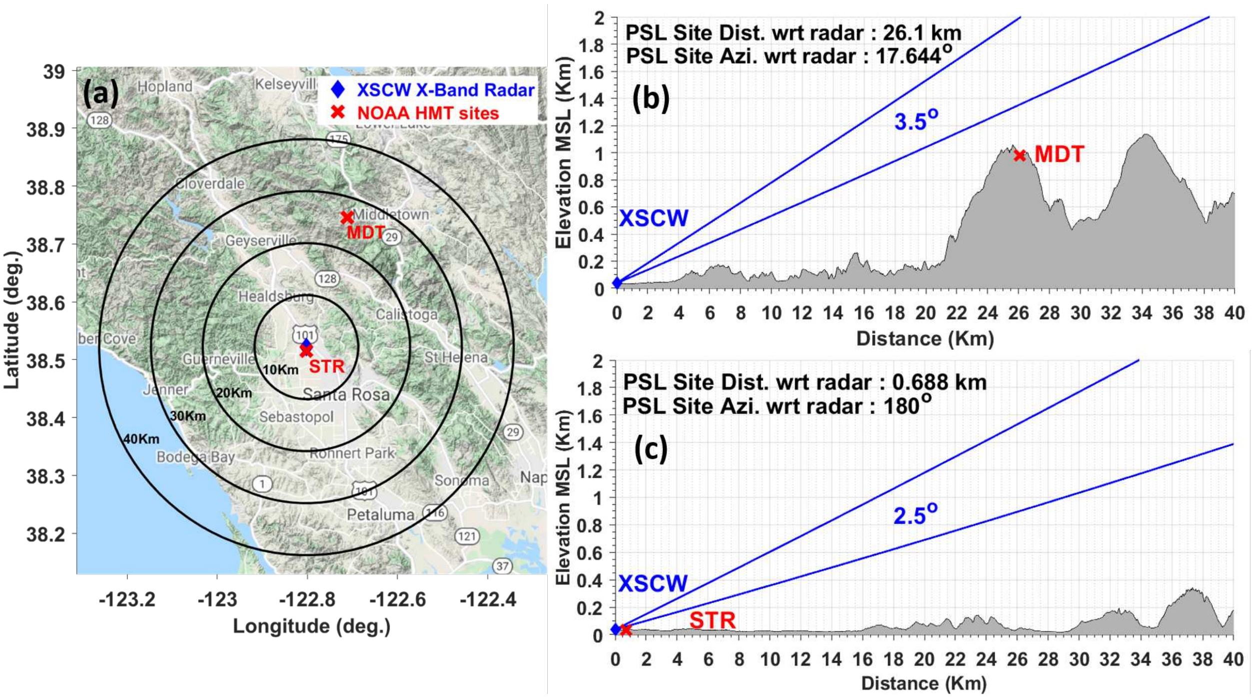

Figure 3.5: (a) A map of the Santa Rosa region in California, highlighting the domain of the XSCW X-Band radar. The black circles represent radar range circles at every 10 km increment. The red crosses represent NOAA PSL ground instrumentation sites, at Santa Rosa (STR) and at Middletown (MDT). Each site contains an S-PROF, a Parsivel disdrometer, and a precipitation gauge. (b) shows the location of the MDT site relative to the radar along the line of sight azimuth direction along with the radar beam. (c) is same as (b) but for the STR site.

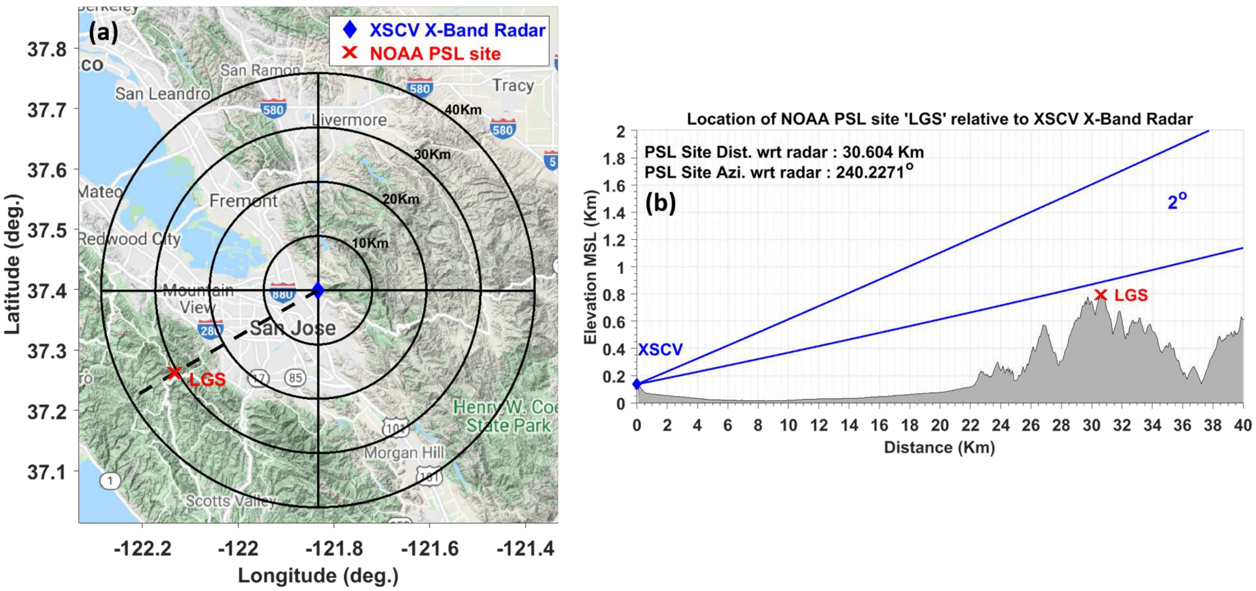

Figure 3.6: (a) A map of the Santa Clara region in California, highlighting the domain of the XSCV X-Band radar. The black circles represent radar range circles at every 10 km increment. The red cross represents the NOAA PSL ground instrumentation site, at Los Gatos (LGS). This site contains an SLR, a Parsivel disdrometer, and a precipitation gauge. (b) shows the location of the LGS site relative to the radar along the line of sight azimuth direction along with the radar beam.

Chapter 4

AQPI X-Band Radars

The AQPI system has a primary objective of enhancing the monitoring and prediction of precipitation, streamflow, and coastal flood warnings in the San Francisco Bay Area. The AQPI domain spans an area of approximately 76,300 square kilometers, encompassing most of the watersheds in the region that are susceptible to flooding. As previously outlined, one of the key aims of the AQPI initiative is the establishment of an operational radar network, which includes X-Band dual-polarization radars to fill coverage gaps, complemented by one C-Band dual-polarization radar. Notably, two X-Band radars, XSCW and XSCV, have been recently deployed in Santa Rosa and Santa Clara, respectively. These radar installations are intended to enhance the existing NEXRAD radar network's coverage and provide comprehensive insights into rainfall processes. For reference, Table 4.1 provides the geographical coordinates of the radar deployment sites, along with site elevation measurements relative to mean sea level.

Table 4.1: AQPI X-Band Radar Site Information

Station ID	**Lat.**	**Lon.**	**Elv. (MSL)**
XSCW	$38.5216^o N$	$122.8022^o W$	$38.5m$
XSCV	$37.3988^o N$	$121.8333^o W$	$32m$

The XSCW radar is located in Santa Rosa within the premises of Sonoma County Water Agency. The radar deployment coordinates are $38.5216^o N$, $122.8022^o W$. A picture of the radar is shown in Figure 4.1a. The XSCV X-band radar is located in Santa Clara, California. at the Penitencia Water Treatment Plant operated by the Santa Clara Valley Water District (SCVWD). The radar deployment coordinates are $37.3988^o N$, $121.8333^o W$. Figure 4.1b shows a picture of the XSCV radar.

For the XSCW radar, the radar positioner, antenna with the nose-cone radome, and transceiver hardware are located on the top of the container whereas, for the XSCV radar, these are located

(a) XSCW in Santa Rosa **(b)** XSCV in Santa Clara

Figure 4.1: X-Band Radars in AQPI. Picture courtesy: Fransesc Junyent

inside the dome-shaped radome on the rooftop of the Fluoride building as shown in Figure 4.1b. The radome is vented and has a thermostat-actuated fan attached to one of the vents to ensure adequate airflow in hot conditions. A harness of cables including single phase 120VAC power, Cat6 Ethernet cable, and a $\frac{3}{8}$ inch diameter air hose runs from the container to the pedestal on top. The UPS, air dehydrator, radar computer, and other necessary tools are located inside the temperature-controlled container. Both radar systems are low-power, dual-polarization, Doppler X-band radar systems operating at 9.4 GHz. The main system characteristics are presented in Table 4.2.

The system's physical layout basic block diagram is shown in Figure 4.2, showing the main components. From a networking point of view, the system block diagram is shown in Figure 4.3, and from a data-flow perspective, the system block diagram is shown in Figure 4.4.

Both radars are configured to perform effective scanning to ensure high temporal and spatial resolution products. Both radars conduct volume Plan Position Indicator (PPI) scans at a cadence of 2 minutes. In particular, the XSCV radar performs $1^o, 2^o, 3^o$, and 4^o elevation sector PPI scans.

Table 4.2: AQPI X-Band Radar System Specification

System	
Main Power	Single Phase 220 V, 20 A
Weight	2500 lbs (max. including radome)
Radome Diameter	128" (typ.)
Radome Height	128" (typ.)
Transmitter	
Type	Magnetron
Frequency	9380-9420 MHz
Number of channels	2
Peak power output	9 kW (per channel typ.)
Average power output	12.5 W (per channel typ.)
Duty Cycle	0.16 % (max.)
PRF	2 kHZ (avg. max.)
Antenna and Positioner	
Antenna Type	Front-Fed Parabolic
Antenna Feed	Orthogonal dual-pol
Antenna Polarization	Linear H, V
Primary Diameter	6 ft.
Beam Width (3dB)	1.4 deg. (typ.)
Gain	41.5 (typ.)
Scan Velocity	60 deg/s (typ.)
Scan Acceleration	90 deg/s^2 (typ.)
Az. Motion Range	Unlimited
El. Motion Range	-10 deg. to 190 deg.
Indoor Mounting Footprint	
Signal Processor Server	Rack, 4U max
U.P.S	Rack, 4U max
Eth. Switch	Rack, 1U max
Dehydrator	Wall/Rack, 2U max

The PPI sectors are from 130^o to 310^o in azimuth angle. This sector region was selected primarily based on the surrounding topography and urban zone. This configuration allowed for coverage of most of the densely populated areas and commercial districts in the valley southwest of the radar while avoiding the mountain areas northeast of the radar. This is desirable to reduce the latency and computational complexity caused by signal processing for ground clutter removal. On the other hand, the XSCW radar is configured to perform full 360^o volume PPI scans with scan elevations $1.5^o, 2.5^o, 3.5^o$, and 4.5^o. In addition, the XSCW radar also performs Range Height Indicator

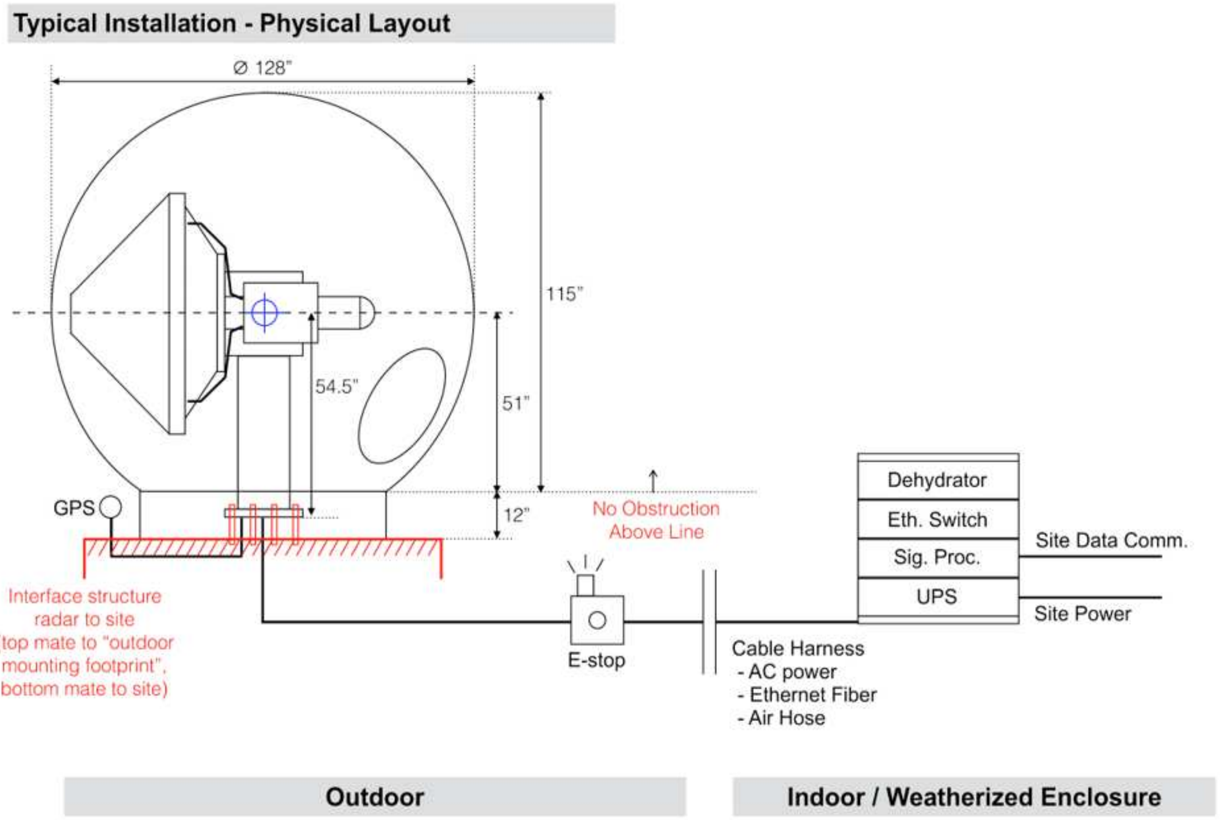

Figure 4.2: AQPI X-Band radar system's physical layout basic block diagram. Reference: AQPI X-Band Radar Handbook

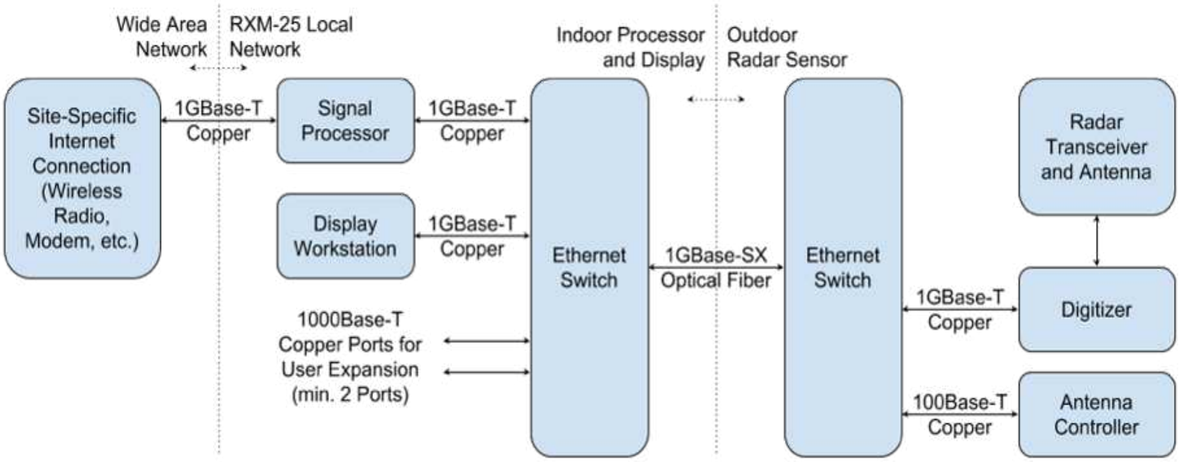

Figure 4.3: AQPI X-Band radar system's network block diagram. Reference: AQPI X-Band Radar Handbook

(RHI) scans at four selected azimuths of $296^o, 300^o, 304^o$, and 308^o. Compared with the scan strategy adopted by the NEXRADs which is a repeated volume scan every 5 to 6 min, the AQPI

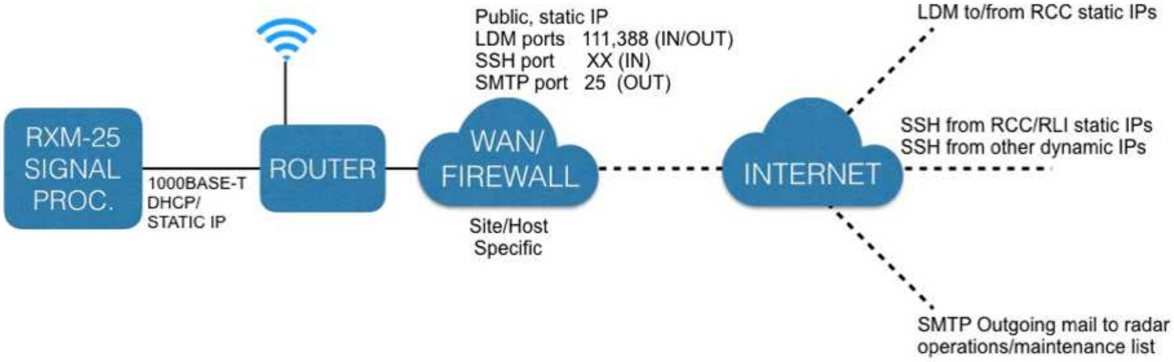

Figure 4.4: AQPI X-Band radar system's data-flow block diagram. Reference: AQPI X-Band Radar Handbook

radars provide higher resolution precipitation information for use in weather forecasts and assist the water districts in their ability to monitor rainfall and streamflow. The lowest elevation scans for both radars are significantly blocked due to terrain. Consequently, measurements obtained from the 2^o scan for XSCV and 2.5^o scan for XSCW were utilized to compute the instantaneous rainfall rate as well as various rainfall accumulation products.

4.1 Beam Blockage Identification and Correction

Due to the complex terrain in the Bay Area region, both XSCW and XSCV suffer from beam blockage in certain areas within their domain. The XSCW radar scan angles are partially blocked by some trees and poles towards the west of the radar but are mostly clear to the east, including watersheds that have been impacted by recent wildfires. The radar performs volume PPI scans with elevation angles varying from 1.5 to 4.5 deg. The combination of scan angles provides low-level coverage for rainfall estimation and 3-D information on storm structure that can be used for numerical weather prediction. The scan cycle is updated every two minutes. Figure 4.5 below shows the terrain around the radar.

The radar blockage patterns for different elevation angles are shown in Figure 4.6. The images show only clutter reflectivity from scans when there was no precipitation event. It can be observed as we go higher in elevation the clutter areas decrease.

Figure 4.5: View of approximate azimuth angles of the terrain around the XSCW radar. (a) 70^o to 210^o azimuth. (b) 200^o to 330^o azimuth. Picture courtesy: Fransesc Junyent

The XSCV radar is located next to the mountains. The scan angles are limited by the mountains and other constraints by the Water Treatment Plant. The scan angles of the radar are 130^o to 310^o in azimuth, providing good coverage over the urban regions of Santa Clara and San Jose as well as some of the watersheds that are important for SCVWD's operations. The radar performs PPI scans with elevation angles varying from 1^o to 4^o. The combination of scan angles provides low-level coverage for rainfall estimation and 3-D information on storm structure that can be used for numerical weather prediction. The scan cycle is updated every two minutes. The pictures in Figure 4.7 show the terrain around the radar.

Again the radar blockage patterns for different elevation angles are shown in Figure 4.8. The images show only clutter reflectivity from scans when there was no precipitation event. A similar trend compared to the XSCW radar clutter map can be observed as we go higher in elevation.

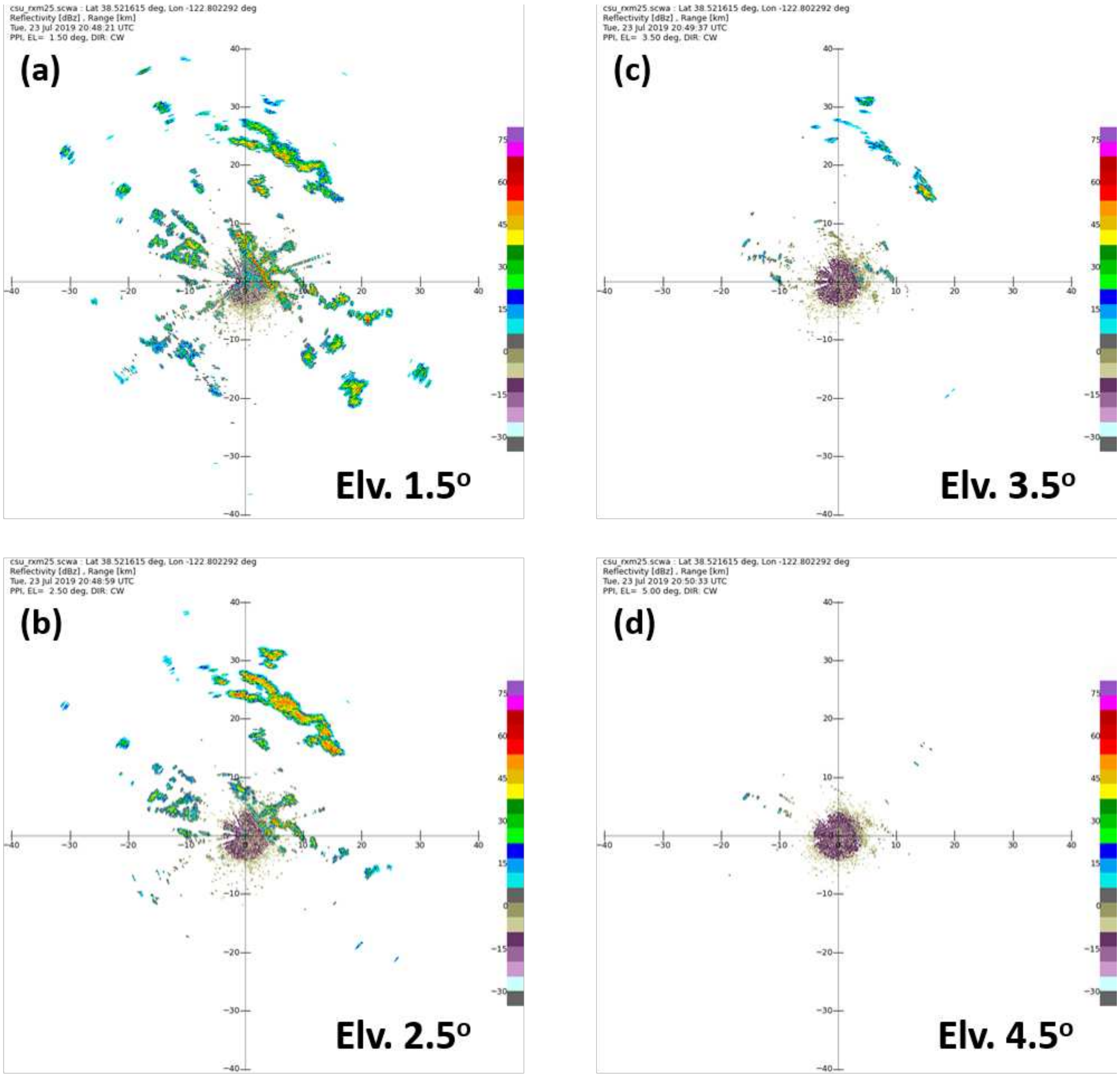

Figure 4.6: Reflectivity due to clutter at multiple elevations for the XSCW radar. (a) 1.5^o elevation scan, (b) 2.5^o elevation scan, (c) 3.5^o elevation scan, (d) 4.5^o elevation scan.

Next, radar visibility maps have been generated through the utilization of Digital Elevation Models (DEM). In Figure 4.9, we can observe the extent of beam blockage for the XSCW radar within the 40 km range domain. The regions that are obstructed are depicted in grey, and this corresponds to the underlying terrain map. The average heights of the radar beams are indicated in areas that remain unblocked. For the $1.5°$ elevation PPI scan, it is evident that a significant portion of the region is blocked by terrain, resulting in a radar visibility of approximately 36.7%. Despite

Figure 4.7: View of the terrain around the radar at approximate azimuth angles. Clockwise from top left: (a) 90^o, (b) 180^o, (c) 250^o, and (d) 135^o. Picture courtesy: Fransesc Junyent

being the lowest elevation scan, the $1.5°$ scan alone does not provide a sufficiently clear view for accurate Quantitative Precipitation Estimation (QPE). The subsequent elevation scan, $2.5°$, exhibits substantially reduced blockage, with radar visibility of 66.3%. As elevation increases, blockage diminishes, but the beam height also rises. Therefore, as a compromise between beam height and blockage, the $2.5°$ scan is selected as the lowest ideal scan for generating various products. Similar radar visibility maps have been created for the XSCV radar, as illustrated in Figure 4.10. Notably, the lowest scan at $1°$ exhibits significant blockage toward the southwest sector. However, in contrast to the XSCW radar, the next elevation scan at $2°$ is unobstructed across the scanning sector. It should be noted that the XSCV radar is configured to perform a sector scan, spanning between specific azimuth angles. Thus, data from the $2°$ elevation scan of the XSCV radar is

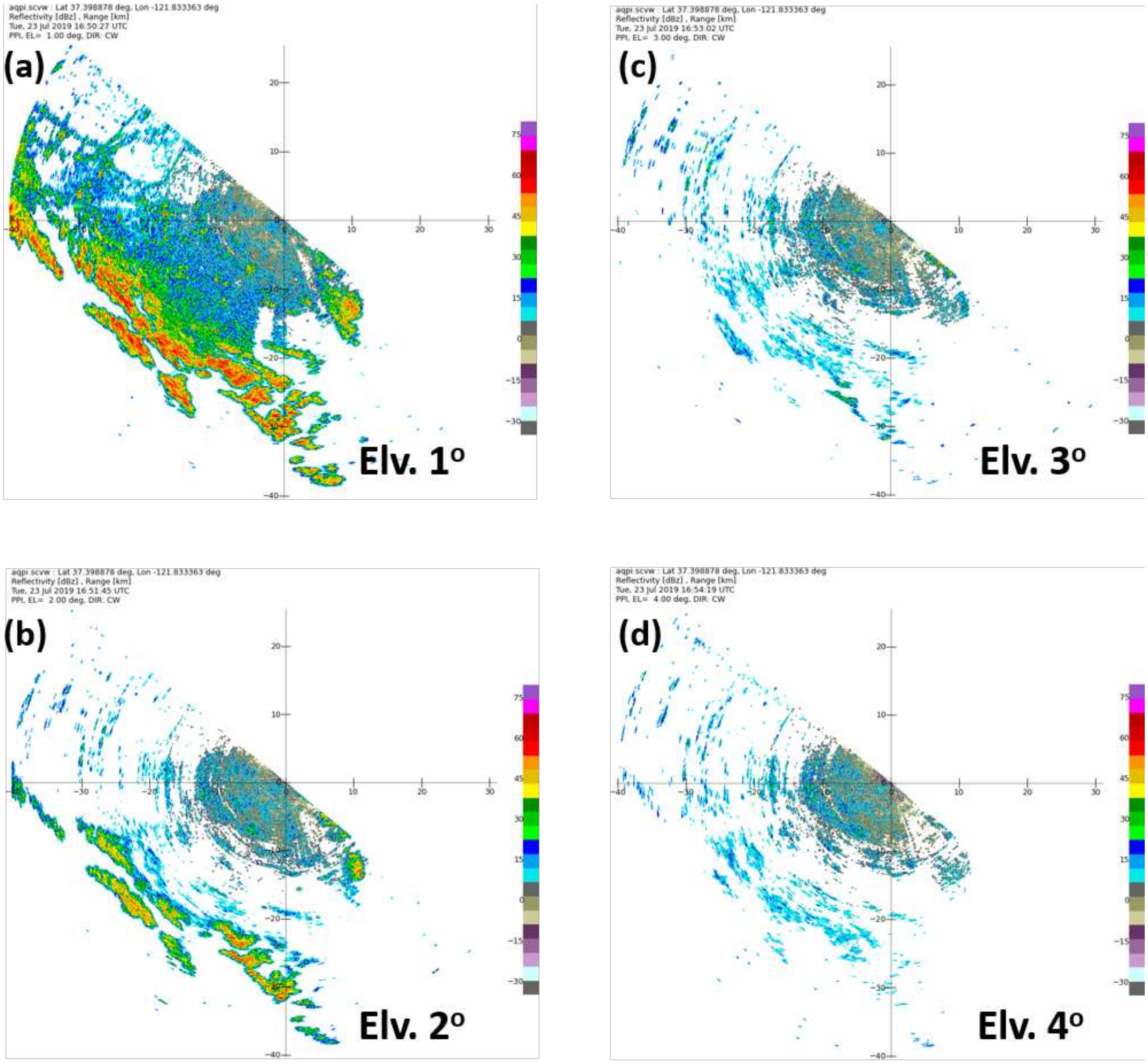

Figure 4.8: Reflectivity due to clutter at multiple elevations for the XSCV radar. (a) 1^o elevation scan, (b) 2^o elevation scan, (c) 3^o elevation scan, and (d) 4^o elevation scan.

employed for the generation of various products. The other two higher elevation scans at 3° and 4° are unobstructed as well, but due to their elevated beam heights, these scans are not considered in the production of QPE products.

The 2.5^o PPI scan of the XSCW radar with around 60% visibility still remains an issue for accurate rainfall estimation over the entire domain. An example of radar beam blockage at different scan elevations while observing a precipitation event on January 27 2021 is presented in Figure 4.11. (a) to (d) presents observed radar reflectivity at different scan elevations. (e) to (f) presents

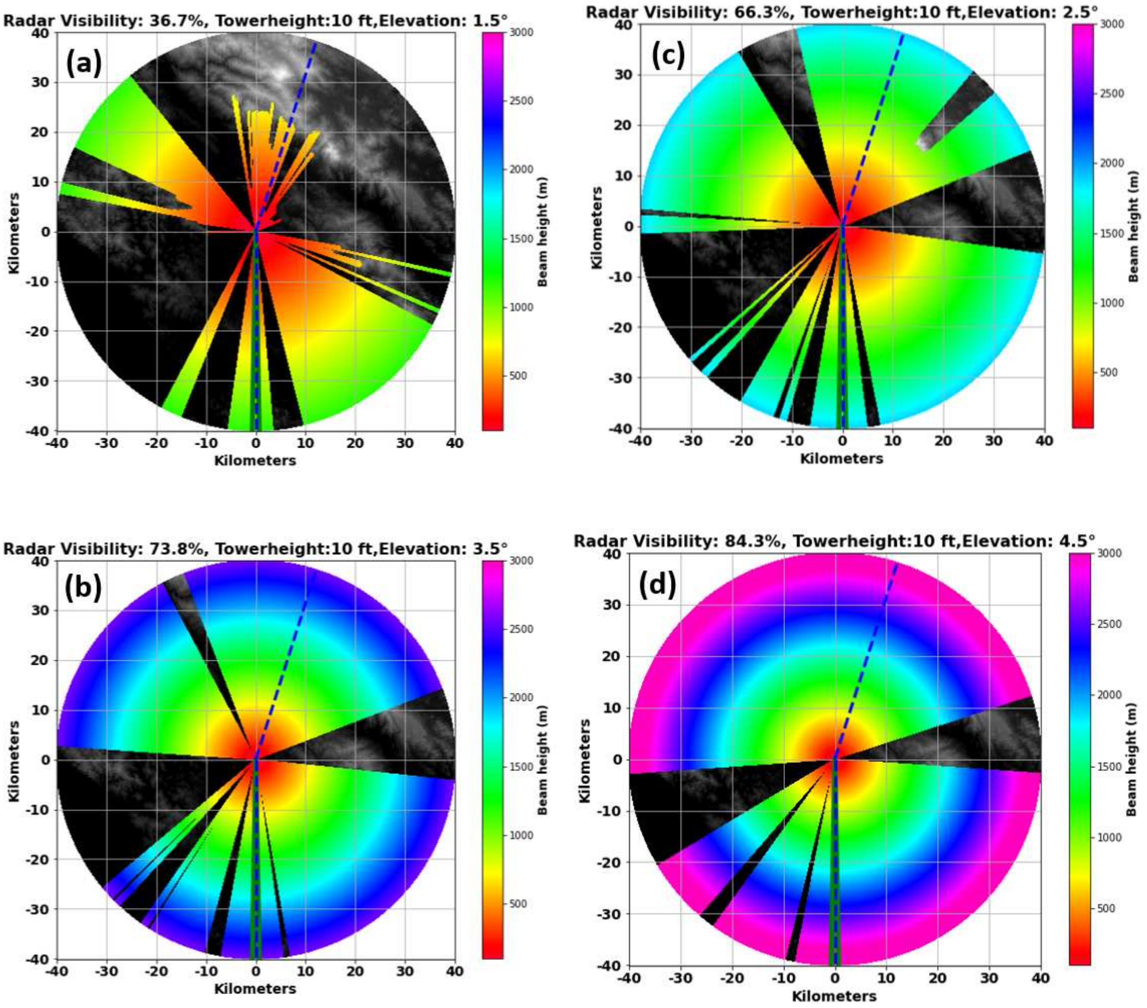

Figure 4.9: Radar visibility map for the XSCW radar. (a) 1.5^o elevation scan, (b) 2.5^o elevation scan, (c) 3.5^o elevation scan, and (d) 4.5^o elevation scan.

the corresponding signal-to-noise (SNR) ratio. It is interesting to notice the blockage patterns observed in Figure 4.11 match with Figure 4.10. However, some additional blockages can be observed on the west side of the radar at all 4 elevation scans which is due to the presence of trees. This is not evident in Figure 4.9 since the DEM can not account for vegetation but it can be seen in Figure 4.5.

To mitigate the beam blockage problem, a hybrid scan has been implemented which uses data from higher elevation scans in place of partial or fully blocked sectors. First, the 2.5^o scan is considered and the blocked azimuths at this scan are identified using the DEM information. Next,

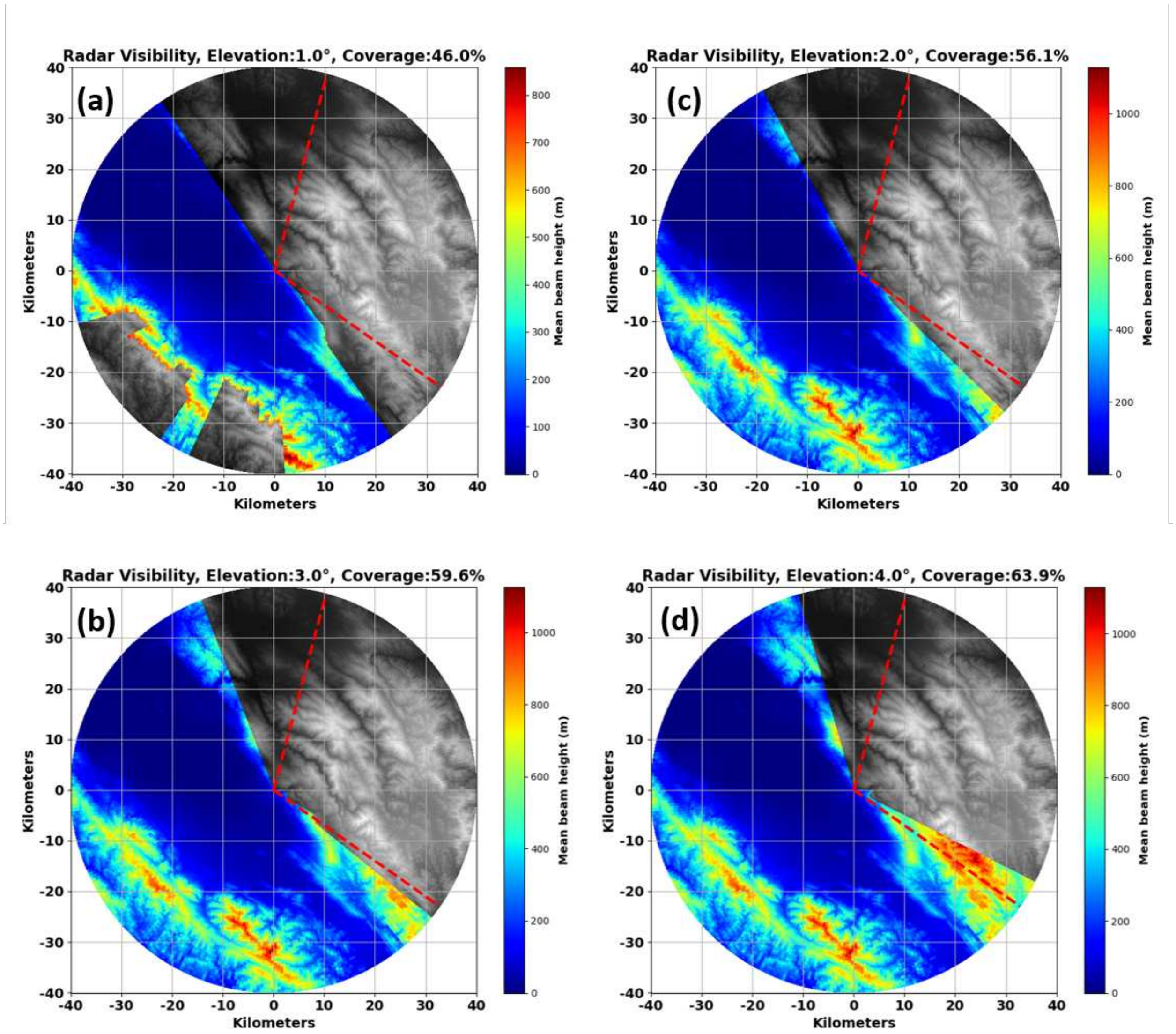

Figure 4.10: Radar visibility map for the XSCV radar. (a) 1.5^o elevation scan, (b) 2.5^o elevation scan, (c) 3.5^o elevation scan, and (d) 4.5^o elevation scan.

where possible, the 3.5^o scan is used to fill up the blocked regions identified in the 2.5^o scan. Finally, the remaining blocked locations are filled up by the 4.5^o scan. Figure 4.12a shows a map of the hybrid scan highlighting which elevation information is used in different azimuth locations. Moving forward, the blocked azimuths, obscured by trees, are pinpointed by assessing the radar reflectivity in the presence of precipitation. To address these blocked regions, azimuthal interpolation is applied. It's worth noting that these specific azimuths remain obstructed at all elevation angles. In this interpolation process, a cubic spline polynomial serves as the interpolating func-

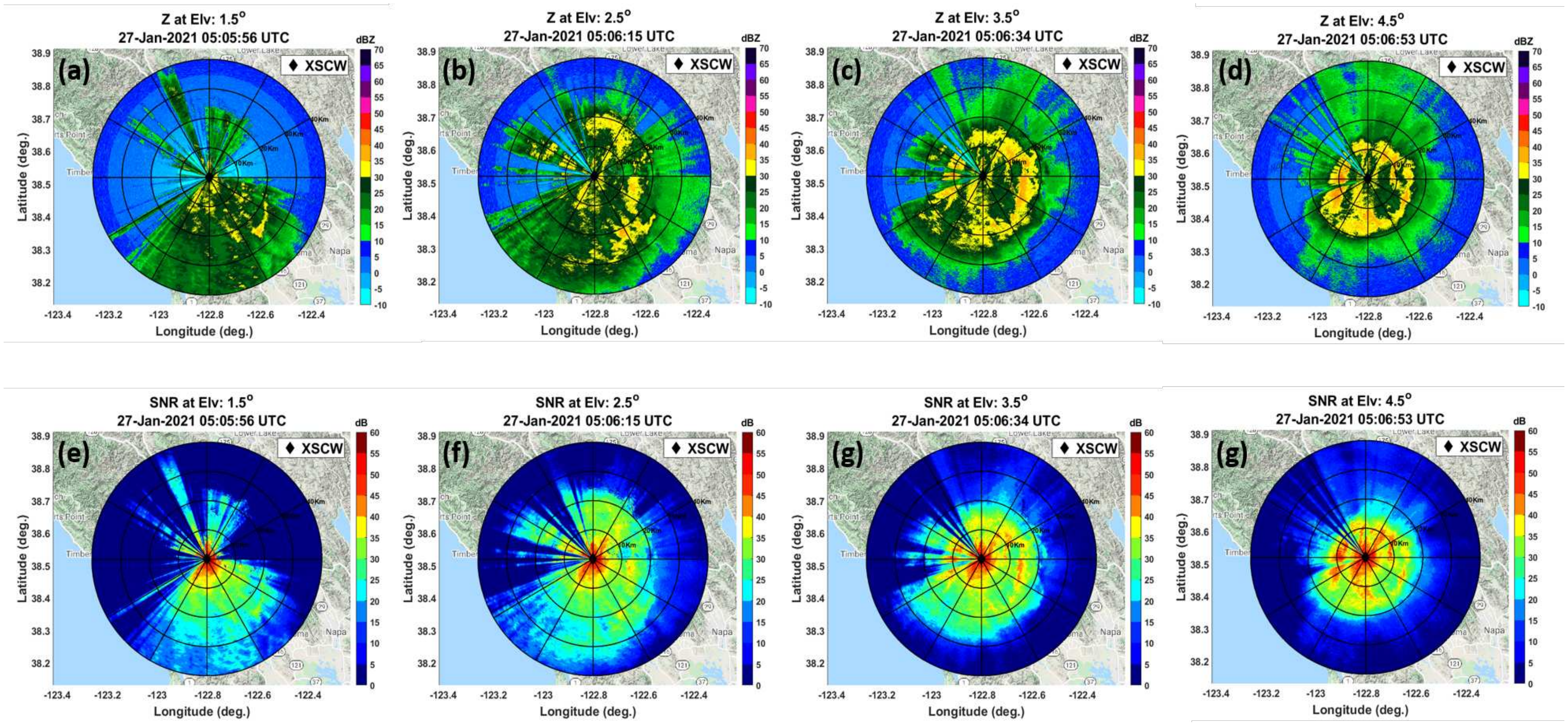
Z at Elv: 1.5^{o} 27-Jan-2021 05:05:56 UTC

Z at Elv: 2.5^{o} 27-Jan-2021 05:06:15 UTC

Z at Elv: 3.5^{o} 27-Jan-2021 05:06:34 UTC

Z at Elv: 4.5^{o} 27-Jan-2021 05:06:53 UTC

SNR at Elv: 1.5^{o} 27-Jan-2021 05:05:56 UTC

SNR at Elv: 2.5^{o} 27-Jan-2021 05:06:15 UTC

SNR at Elv: 3.5^{o} 27-Jan-2021 05:06:34 UTC

SNR at Elv: 4.5^{o} 27-Jan-2021 05:06:53 UTC

Figure 4.11: XSCW Radar observations of a precipitation event on Jan-27-2021. The top row shows observed radar reflectivity (Z). The bottom row shows the corresponding signal-to-noise ratio (SNR). (a)&(e) 1.5^{o} elevation scan, (b)&(f) 2.5^{o} elevation scan, (c)&(g) 3.5^{o} elevation scan, and (d)&(h) 4.5^{o} elevation scan.

tion, effectively filling in the blocked areas. This is demonstrated in Figure 4.12b. The white areas indicate interpolation in azimuth.

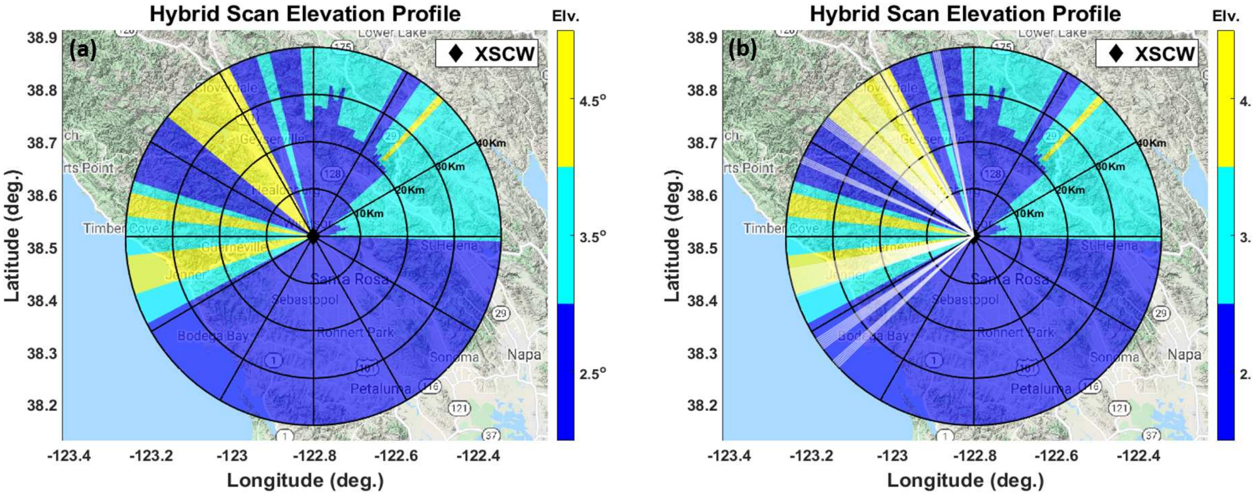

Figure 4.12: (a) XSCW domain map showing hybrid scan using scans from different elevations. (b) Same as (a) along with regions of azimuthal interpolation.

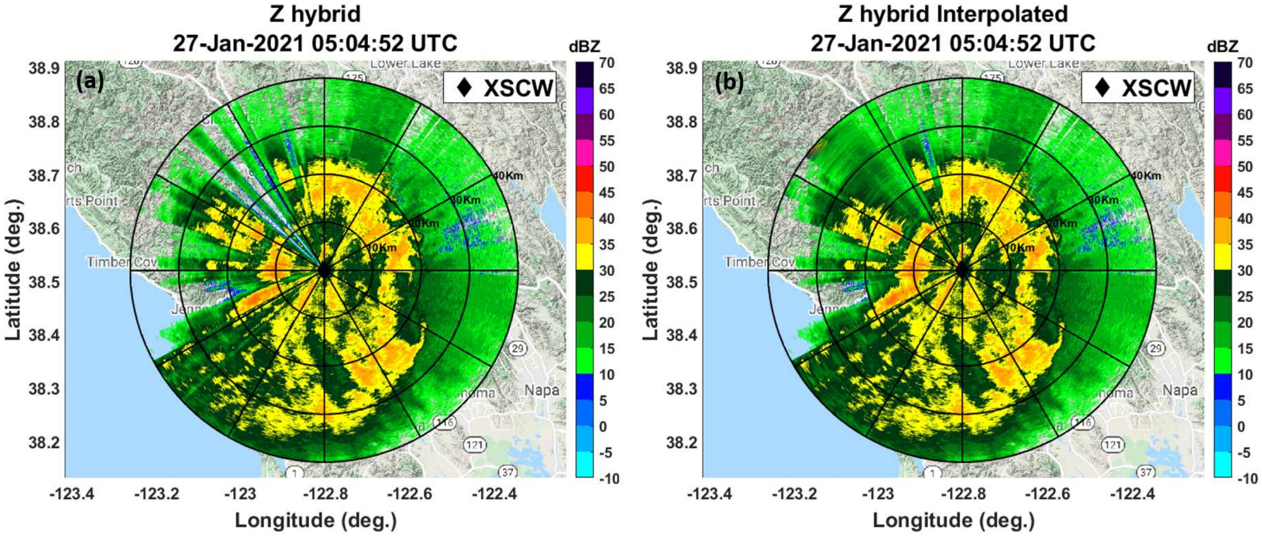

Figure 4.13: Example of XSCW radar hybrid scan using observation from Jan-27-2021 precipitation event. (a) Map showing hybrid scan. (b) Same as (a) along with azimuthal interpolation to mitigate observation discontinuity due to the presence of tress.

An example of the hybrid scan of XSCW radar reflectivity is shown in Figure 4.13 to demonstrate the hybrid scan technique used for mitigating beam blockage. It should be noted that a similar methodology is used for other radar variables such as Z_{DR} and K_{DP}.

4.2 Attenuation Correction

The attenuation induced by the propagation of the EM signals in rain media can not be neglected in X-band applications. Substantial research conducted in the past, as evidenced by [15, 45, 46], has underscored the significance of this issue. It has been established that this challenge can be effectively addressed through the application of attenuation correction techniques reliant on measurements of the differential propagation phase. Equation 2.8 gives the relation of specific differential phase (K_{DP}) to the drop size distribution. The two-way differential propagation phase (ϕ_{DP}) between two range locations r0 and r is expressed in terms of K_{DP} as

$$\phi_{DP} = 2 \int_{r0}^{r} K_{DP}(s) ds \tag{4.1}$$

where s is the path for integration. Electromagnetic waves passing through precipitation suffer from power loss resulting from absorption and scattering. Specific attenuation at two polarization states and differential attenuation are related to DSD as

$$\alpha_{h,v} = 4.343 \times 10^{-3} \int_{D_{min}}^{D_{max}} \sigma_{ext(h,v)}(D) N(D) dD \quad (dBkm^{-1}) \tag{4.2a}$$

$$\alpha_{dp} = \alpha_h - \alpha_v \tag{4.2b}$$

where σ_{ext} is the extinction cross-section derived by the sum of the absorption cross-section and scattering cross-section. At X-Band, absorption dominates. It can be shown that at frequencies greater than 5 GHz, the specific attenuation and differential attenuation can be approximated in terms of K_{DP} as

$$\alpha_h = aK_{dp} \tag{4.3a}$$

$$\alpha_{dp} = bK_{dp} \tag{4.3b}$$

Two-way cumulative attenuation A_h and differential attenuation A_{dp} can be expressed as

$$A_h = 2\int_{r0}^{r} \alpha_h(s)ds \tag{4.4a}$$

$$A_{dp} = 2\int_{r0}^{r} \alpha_{dp}(s)ds \tag{4.4b}$$

Attenuation in radar signals can also be attributed to atmospheric gases or cloud droplets. It is worth noting that while attenuation caused by atmospheric gases at X-band frequencies can be comparable to the attenuation caused by very light rainfall, it becomes negligible when dealing with heavy to moderate rainfall. Thus for an inhomogeneous rain path, i.e. when A_h, v varies with path, the attenuation corrected reflectivity $Z_{h(corr)}$ and differential reflectivity $Z_{dr(corr)}$ can be obtained as

$$\begin{aligned} Z_h(r)\ \ (dB) &= Z_{h(corr)}(r)\ \ (dB) - 2\int_0^r \alpha_h(s)ds \\ &= Z_{h(corr)}(r)\ \ (dB) - 2a\int_0^r K_{dp}(s)ds \end{aligned} \tag{4.5a}$$

$$\begin{aligned} Z_{dr}(r)\ \ (dB) &= Z_{dr(corr)}(r)\ \ (dB) - 2\int_0^r \alpha_{dp}(s)ds \\ &= Z_{dr(corr)}(r)\ \ (dB) - 2b\int_0^r K_{dp}(s)ds \end{aligned} \tag{4.5b}$$

In AQPI, the attenuation correction procedure is implemented following the above methodology using equations 4.3 and 4.5. In order to calculate the specific attenuation, K_{DP} must be estimated which is accomplished using the algorithm described in [70]. Next, actual DSD measurements from years 2016 to 2018 collected at the NOAA PSL sites STR, MDT, and LGS are used to compute estimates of attenuation at h-pol, differential attenuation, and K_{DP}. This is done by T-Matrix scattering computation at X-Band using the Beard-Chuang drop shape model at different temperatures. The coefficients a and b mentioned in equations 4.3 are calculated using linear regression analysis on α_h, α_{DP}, and K_{DP} estimates. Figure 4.14a and 4.14b show the scatter plots of α_h versus K_{DP} and α_{DP} vs K_{DP} respectively. The black curve denotes the best-fit line which is obtained by least squares regression analysis. The coefficient for α_h is 0.37 whereas the coefficient for α_{dp} is 0.074. Examples of attenuation correction for both XSCW and XSCV radar are shown in Figures 4.15 and 4.16. It should be noted the attenuation correction procedure described earlier applies to rain regions only. Therefore, before applying the attenuation correction procedure, first, the environmental freezing level is first identified. Specific attenuation estimates are only calculated for radar range bins below the freezing level. Attenuation correction in the snow region is not carried out since attenuation due to snow aggregates at X-Band is negligible compared to rain.

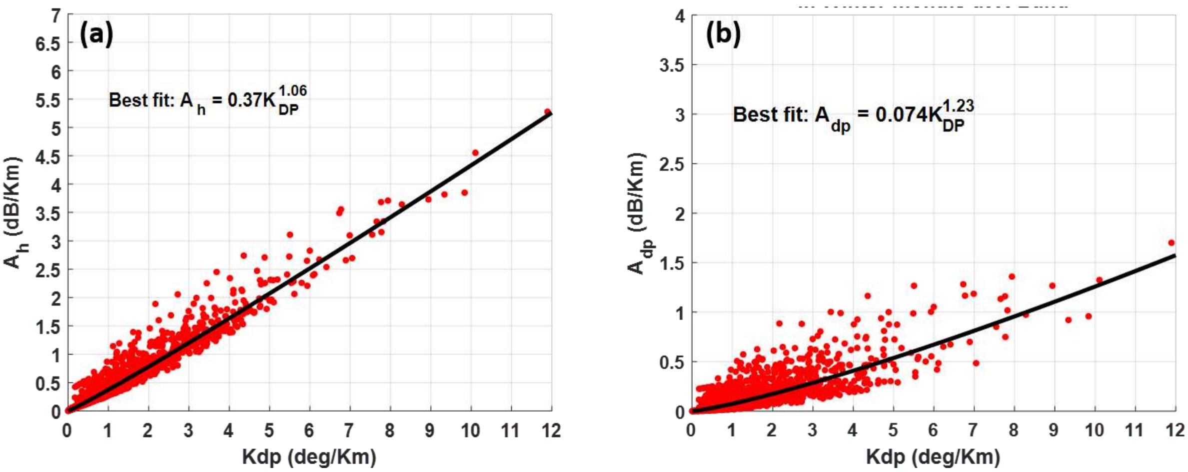

Figure 4.14: Scatter plots of (a) specific attenuation versus specific differential phase and (b) specific differential attenuation versus specific differential phase computed from DSD measurements from 2016 to 2018 at the NOAA PSL sites of STR and MDT. The black lines indicate the best-fit line obtained using the least squares method.

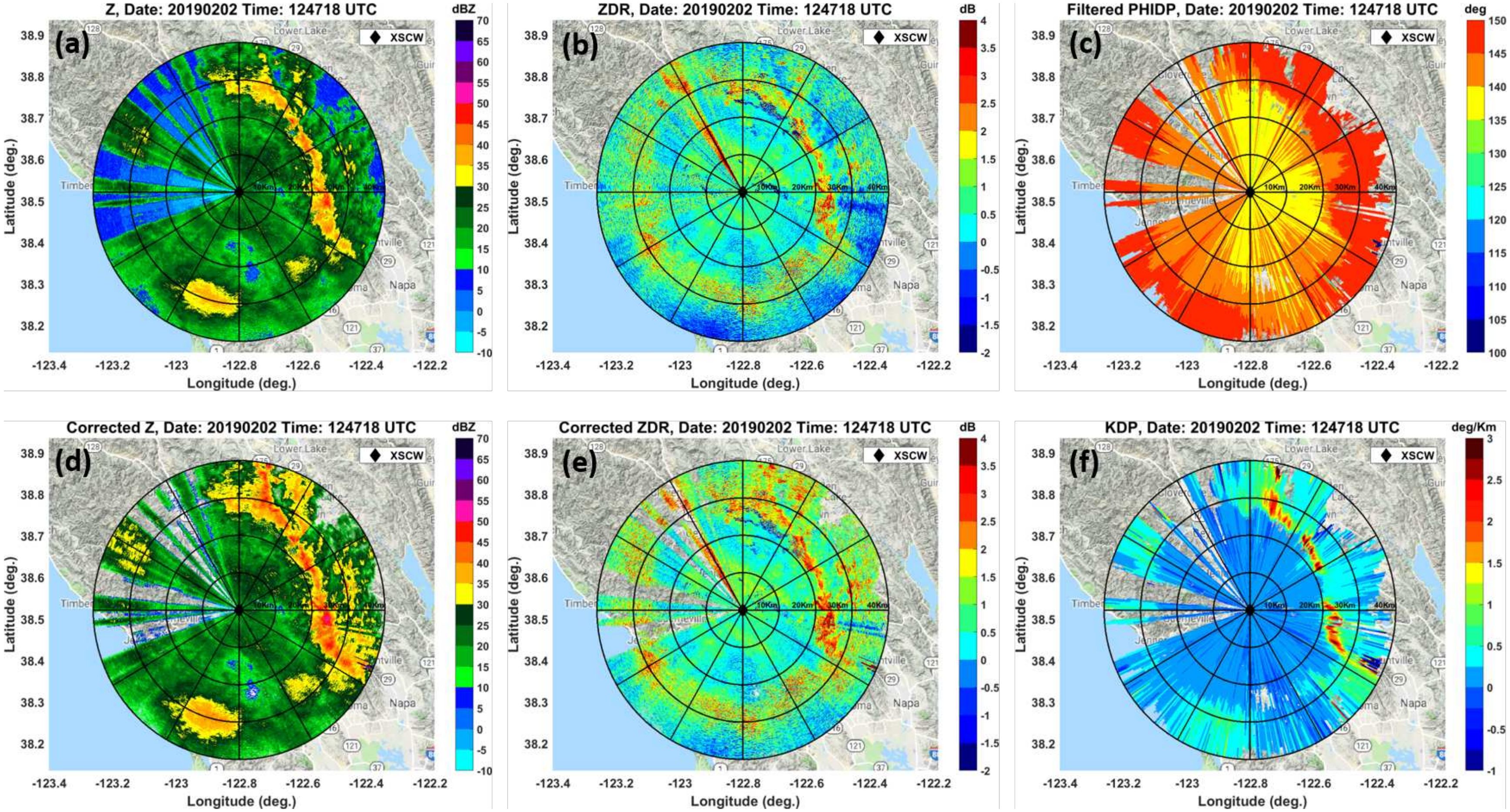

Figure 4.15: Example of attenuation correction of XSCW radar observations at 2.5^o tilt of an AR event on Feb-02-2019. (a) Observed reflectivity, (b) Observed differential reflectivity, (c) Differential propagation phase, (d) Attenuation corrected reflectivity, (e) Attenuation corrected differential reflectivity, and (f) Specific Differential Phase.

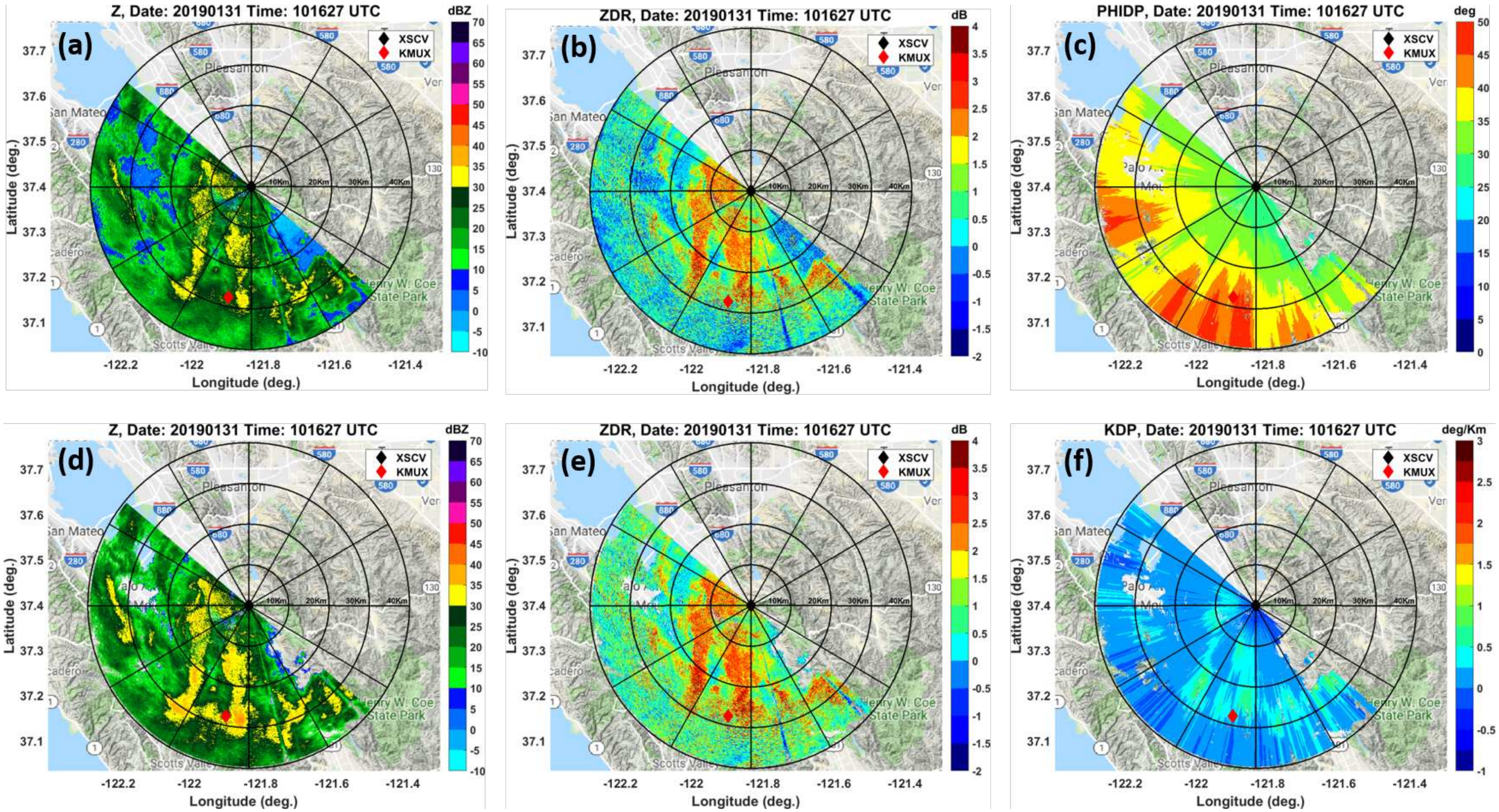

Figure 4.16: Example of attenuation correction of XSCV radar observations at 2^o tilt of an AR event on Jan-31-2019. (a) to (e) are the same as Figure 4.15 but for the XSCV radar.

4.3 Radar Calibration

Radar reflectivity stands as one of the most prevalent radar observables, forming the foundation for numerous radar-based retrievals. Accurate measurements of reflectivity are pivotal, particularly in the context of quantitative precipitation estimation (QPE) retrievals, where the need for precise calibration of all radar systems becomes evident. In practice, radar measurements can be subject to systematic biases stemming from diverse factors like hardware and system design. To ensure the accuracy of reflectivity measurements, it's crucial to maintain temperature stability within the radar housing, safeguard antennas and radomes against moisture, conduct frequent automatic internal calibrations, and carry out regular maintenance procedures [71, 72].

In systems such as AQPI, the verification of reflectivity calibration assumes a central role. The use of naturally occurring volumetric targets for calibration verification is a well-established approach. Raindrops, as reference targets, offer the advantage of directly accounting for antenna properties in the calibration process. The first successful efforts to evaluate meteorological radars using raindrops date back to 1968, and subsequent years have witnessed the development of various assessment techniques. One of the most widely adopted methods hinges on disdrometer observations. Here, drop size distributions (DSDs) measured by disdrometers are converted into radar reflectivity through electromagnetic scattering computations. This approach involves comparing time series or distributions of calculated and observed reflectivities. A significant source of uncertainty in this method relates to the vertical variability of reflectivity profiles, which can arise from factors like turbulence, wind shear, evaporation, drop breakup, and coalescence. Consequently, it's imperative to focus on radar observations close to the ground, where disdrometers are positioned. In AQPI, disdrometers are colocated with both X-Band radars and sample drops at a 10-second interval. An inherent challenge in comparing the two sets of instantaneous observations lies in the substantial disparity in sample volumes. The radar averages precipitation over a considerably larger volume in each pulse compared to the disdrometer. To address this discrepancy, 10-second DSD samples are integrated into 2-minute samples. For instance, the disdrometer at the STR site is located 68 meters from the XSCW radar, with the radar's 2.5° beam height at the disdrometer location positioned at 35 meters above ground level. This proximity makes the STR disdrometer an ideal instrument for radar calibration. In this analysis, we consider three precipitation events that occurred on Nov 17-18, 2020, Mar 10, 2021, and Mar 18, 2021. Figures 4.17, 4.18, and 4.19 present examples of time series comparisons of reflectivity between the XSCW radar and the STR disdrometer. In these figures, blue lines represent the time series of radar reflectivity computed from the 2.5° PPI scan over the disdrometer location, while red lines depict time series of reflectivity computed from DSD measurements using T-Matrix scattering computations. The comparison reveals a negative bias in the XSCW radar's reflectivity, indicating that the radar reflectivity values are lower compared to those from the disdrometer. To quantify this bias, we calculate the difference between the median values of the radar and disdrometer reflectivity distributions. The corresponding histograms are illustrated in Figure 4.20. Across the three events considered, the biases are approximately 5 dB. Specifically, the bias for the events on Nov 17-18, 2020, Mar 10, 2021, and Mar 18, 2021, amounts to -4.71 dB, -5.48 dB, and -5.43 dB, respectively.

An average bias of 5 dB was estimated and added to the radar observations. Next, validation of the attenuation and bias-corrected X-Band reflectivity is performed independently through a comparison with the nearby NEXRAD radars. The nearest NEXRAD radar to XSCW is the KDAX radar which is located to the west at about 98 km. The baseline azimuth of the KDAX with respect to the XSCW radar is 90.98^{o} while that of the XSCW radar with respect to the KDAX radar is 271.68^{o}. The comparison is performed between the XSCW 2.5^{o} elevation PPI scan and KDAX 0.9^{o} PPI scan when both the radars point at each other. Figure 4.22a shows the geometry when XSCW and KDAX point to each other. The beam top and bottom heights are marked by blue for the XSCW radar and by red for the KDAX radar. The common observation observations volume is marked by black vertical lines between 25 to 33 km from the XSCW location. Figure 4.22b shows the ray profile of radar reflectivity along the baseline azimuth. The observed reflectivity of the XSCW radar is represented by the black line. The blue line corresponds to the attenuation and bias-corrected reflectivity, while the red line depicts the reflectivity from the KDAX radar. It is worth noting that the NEXRAD radars, operating at the S-Band frequency, do not require

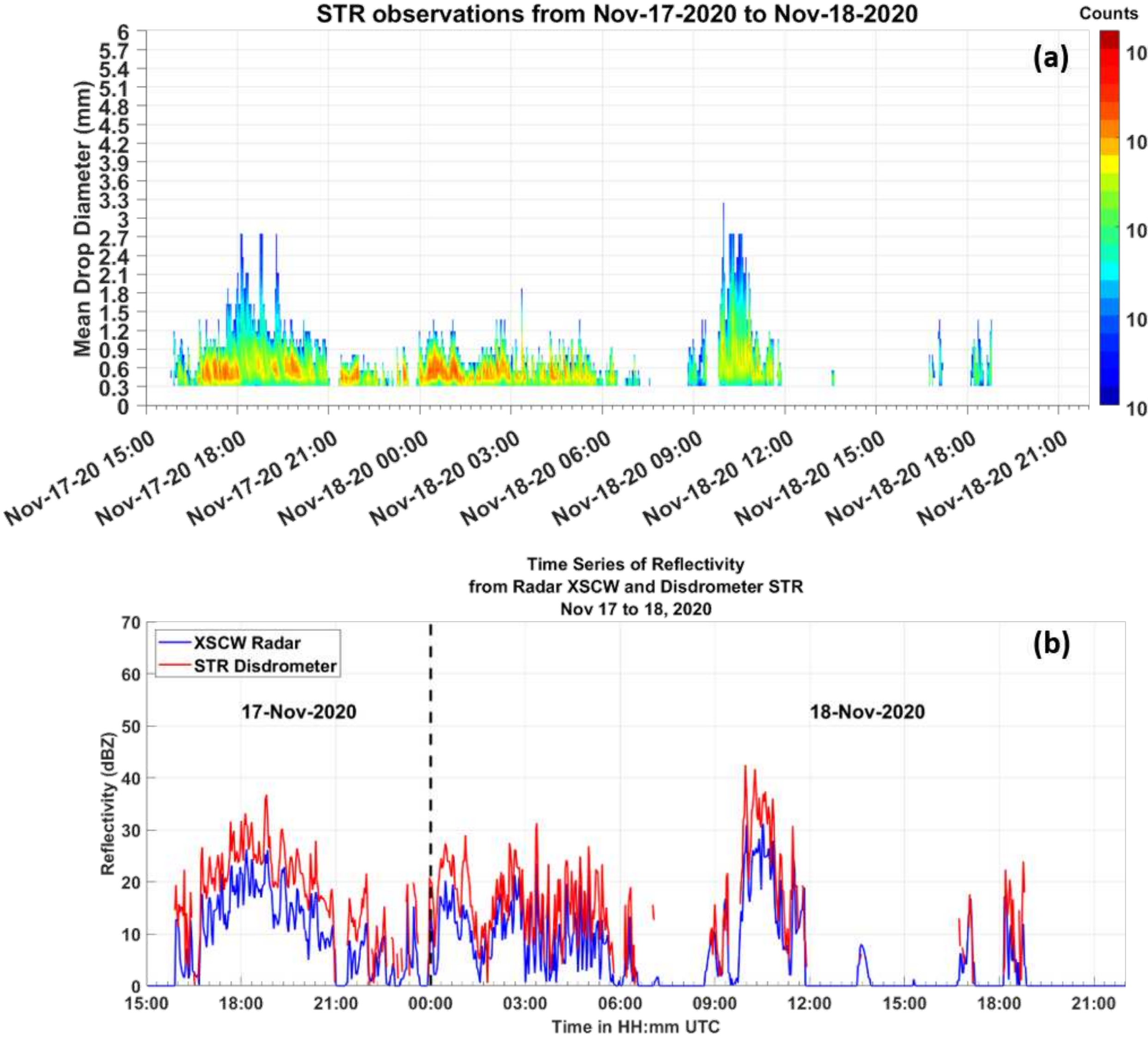

Figure 4.17: Comparison of radar reflectivity between the XSCW radar and the STR disdrometer for a precipitation event from Nov 17 to Nov 18, 2020. (a) Drop size distribution measured by the disdrometer. (b) Time series of radar observed reflectivity at the disdrometer location (denoted by blue) versus reflectivity computed from the DSD measurements (denoted by red).

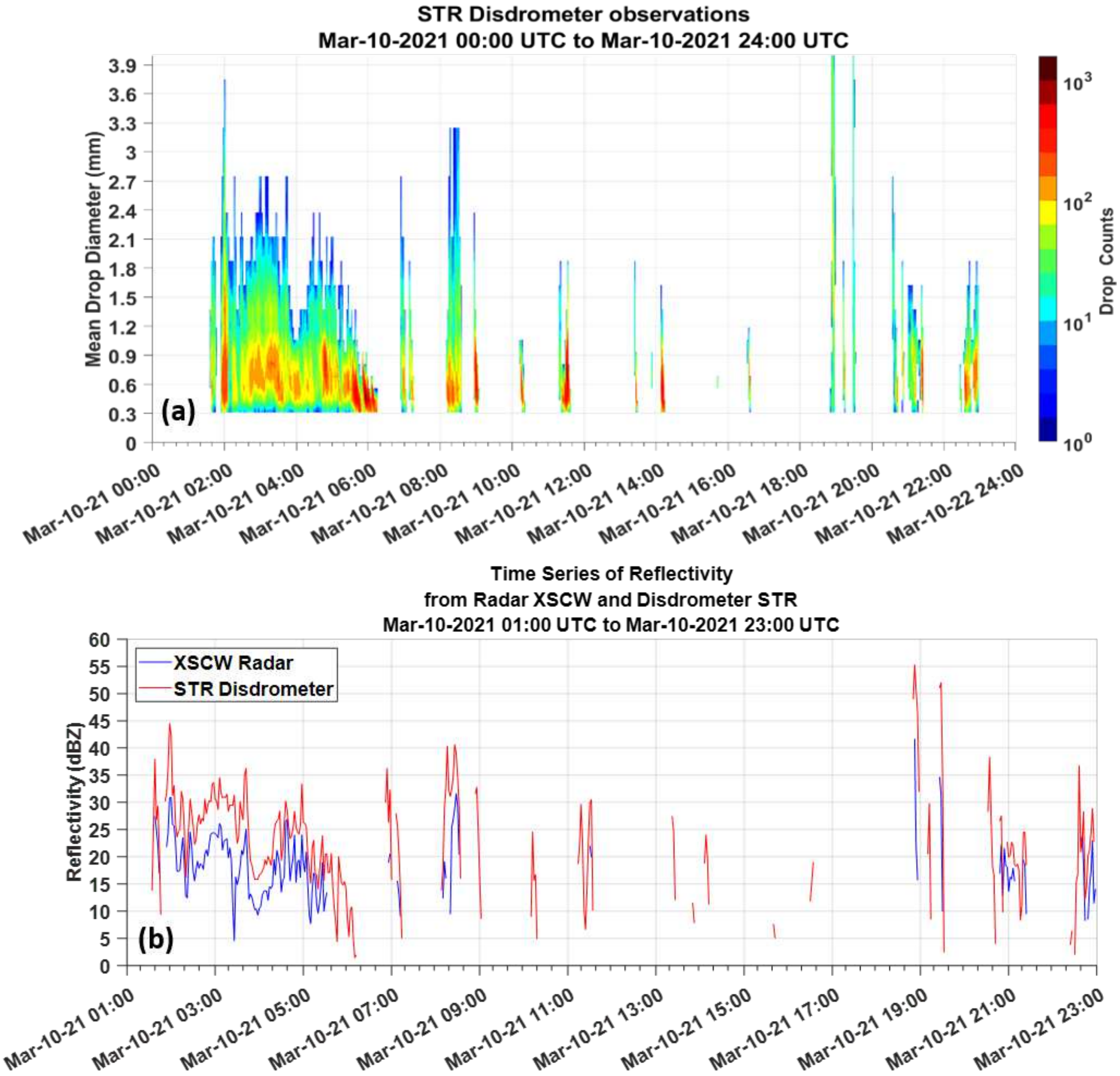

Figure 4.18: Same as Figure 4.17 but for a precipitation event on Mar 10 2021.

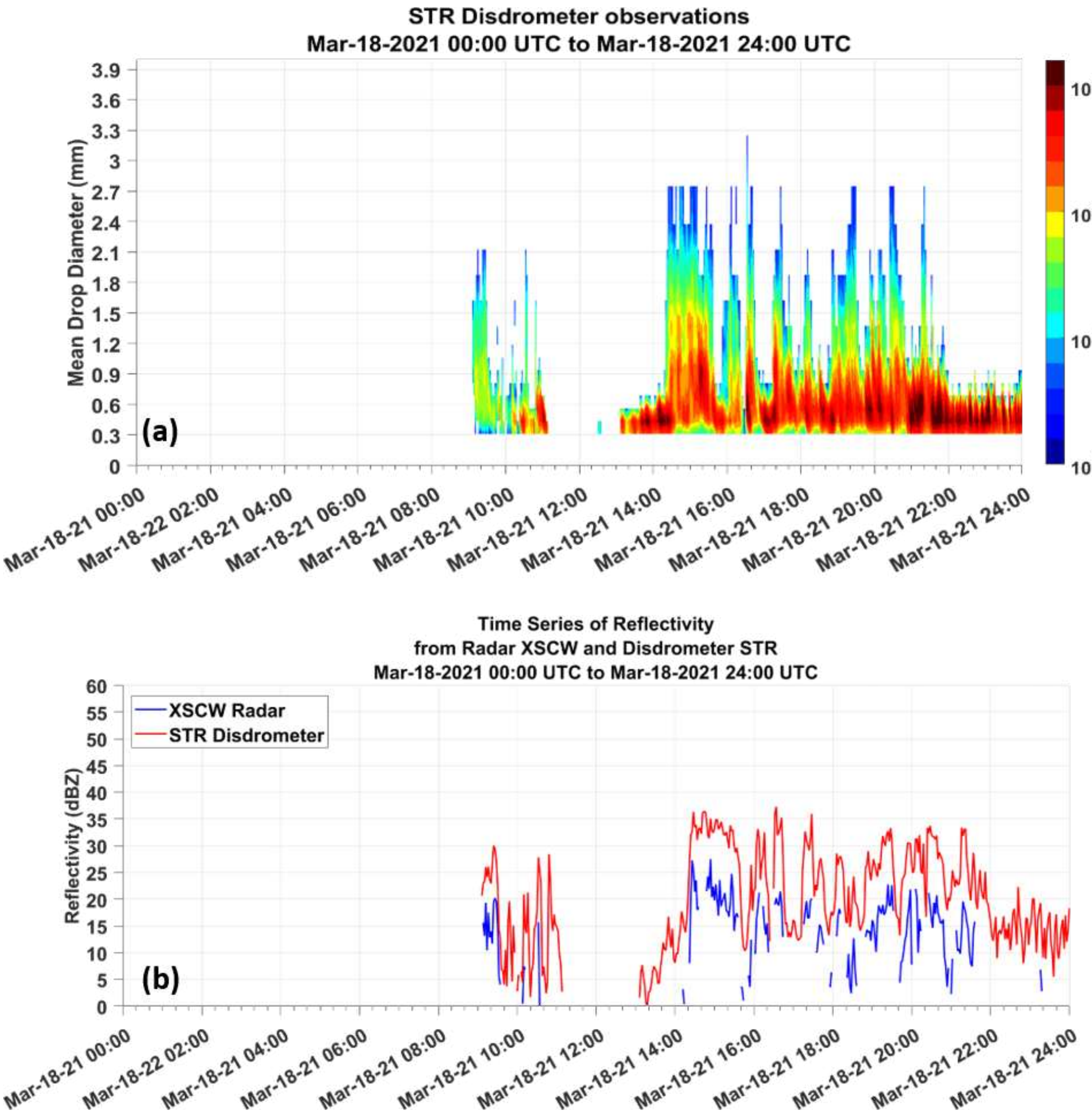

Figure 4.19: Same as Figure 4.17 but for a precipitation event on Mar 18 2021.

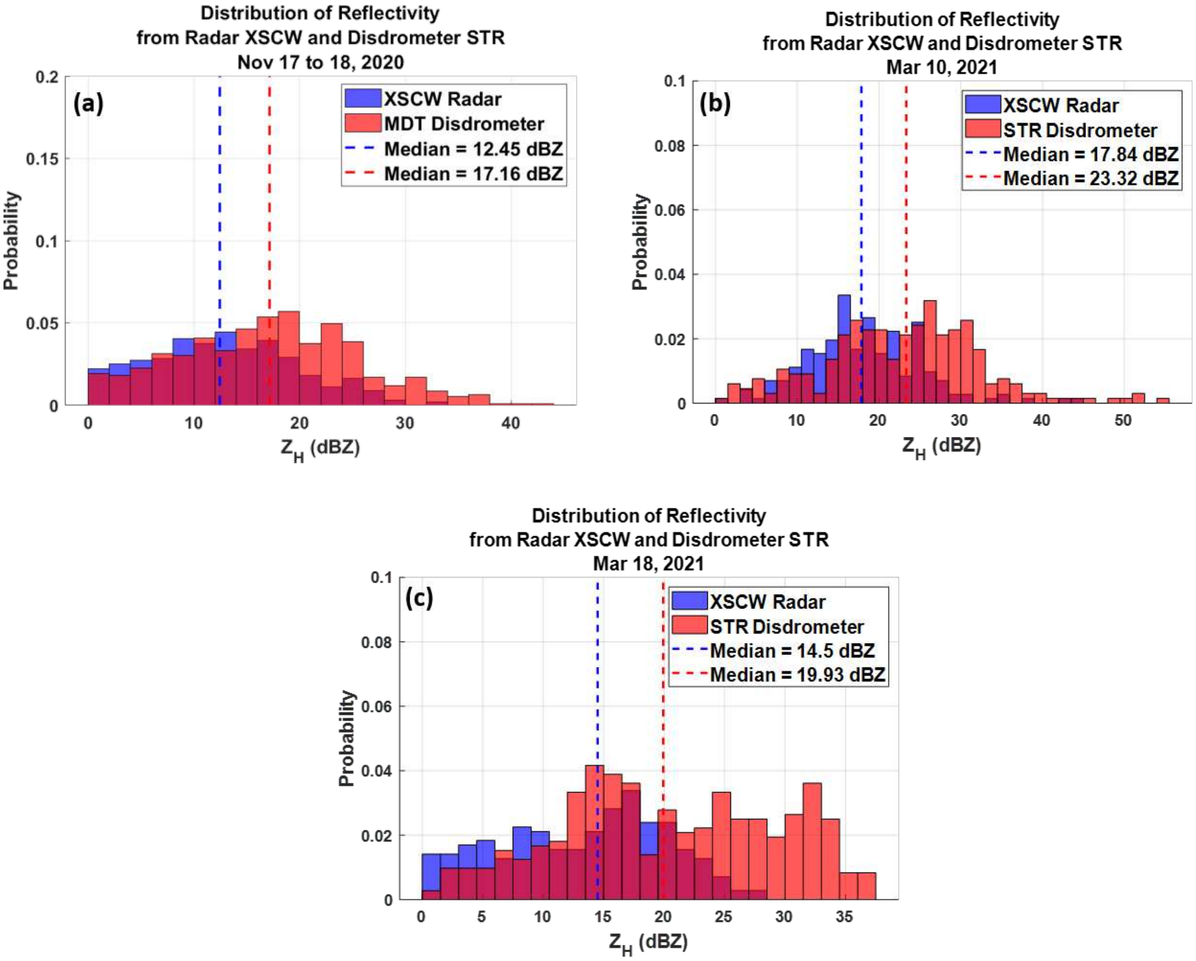

Figure 4.20: Distribution of reflectivity at the STR disdrometer site computed from XSCW radar observations and the STR disdrometer measurements for different precipitation events. (a) Nov 17-18, 2020 event. (b) March 10, 2021 event. (c) March 18, 2021 event. The dotted lines represent the median values of the distributions.

attenuation correction. It can be observed that the XSCW reflectivities closely align with those from the KDAX radar within the common volume.

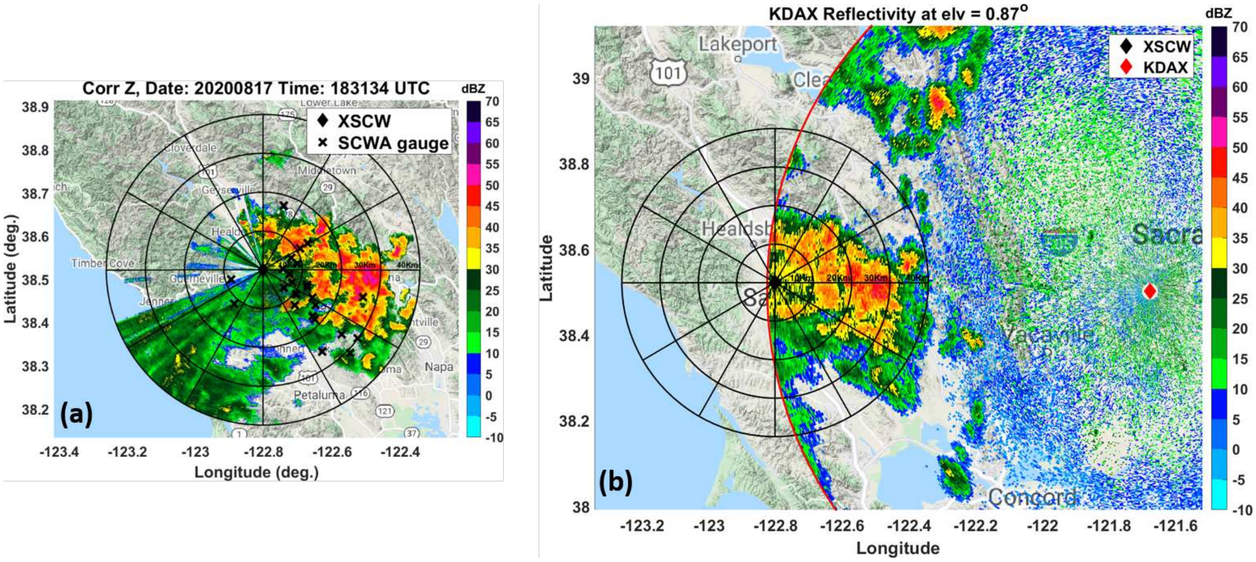

Figure 4.21: Observation of reflectivity from a precipitation event on Aug 17, 2020 at 18:31:34 UTC. (a) XSCW radar 2.5^o PPI scan. (b) KDAX radar 0.9^o PPI scan centered at the XSCW radar location.

Similar comparisons of X-Band versus NEXRAD have been conducted for the XSCV radar as well. Figure 4.23 shows XSCV 2^o PPI scan and KMUX 0^o PPI scan from a precipitation event from January 27, 2021. The KMUX PPI image is centered at the location of the XSCV radar. The KMUX radar is located to the south of XSCV radar at a distance of 27.63 km. The baseline azimuth of the KMUX with respect to the XSCV radar is 11.98^o while that of the XSCV radar with respect to the KMUX radar is 198.98^o. The comparison is performed between the XSCV 2^o elevation PPI scan and KMUX 0^o PPI scan when both radars point at each other. A similar trend compared to 4.22 can be observed for XSCV versus KMUX in Figure 4.24. In the common volume region attenuation and bias-corrected XSCV reflectivity appears to match the KMUX reflectivity very well.

A commonly employed method for determining the system bias in Z_{DR} is the "bird bath" scan. In this scanning technique, the radar is oriented vertically during light rain conditions and rotated through a full $360°$ in azimuth. The measured Z_{DR} values are then averaged across the entire $360°$

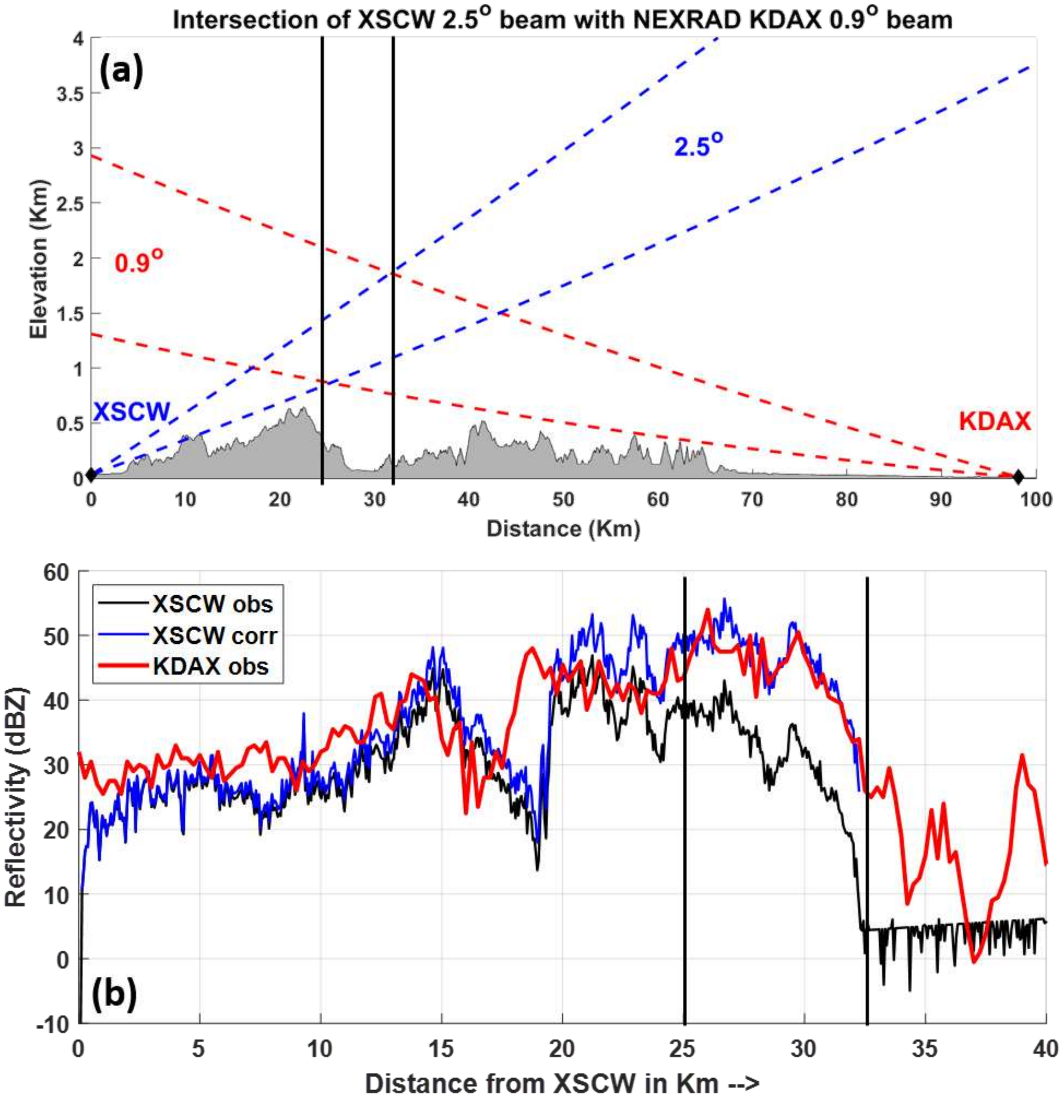

Figure 4.22: Comparison of reflectivity between XSCW and KDAX from a precipitation event on Aug 17, 2020 at 18:31:34 UTC. (a) Geometry of XSCW radar 2.5^o beam and KDAX radar 0.9^o beam along the baseline azimuth when both the radars are pointing at each other. (b) Ray profiles of reflectivities from the XSCW and the KDAX radar. The common volume is marked by vertical black lines in both (a) and (b).

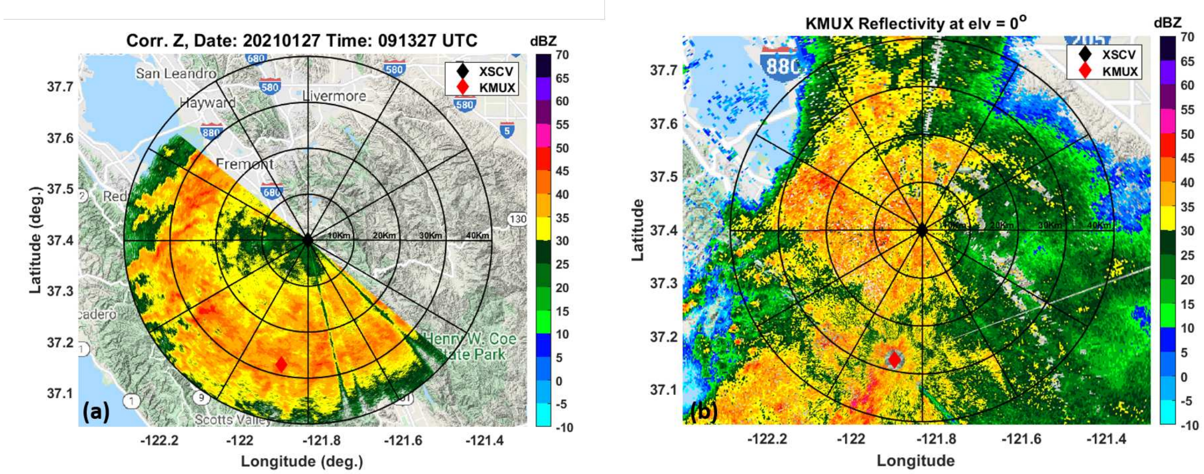

Figure 4.23: Observation of reflectivity from a precipitation event on Jan 27, 2021, at 09:13:27 UTC. (a) XSCV radar 2^o PPI scan. (b) KMUX radar 0^o PPI scan centered at the XSCV radar location.

rotation to eliminate azimuthal dependencies. Therefore, any remaining biases would primarily arise from differences between the horizontal (H-pol) and vertical (V-pol) channels of the radar. Deviations from 0 dB in the measured Z_{DR} indicate the presence of bias, as detailed in prior studies [73, 74]. It's worth noting that this technique is predominantly applied in research radar settings. However, the AQPI radars are not configured for vertically pointing scans. Instead, an alternative approach is employed for the AQPI radars, involving the observation of drizzle at a very low elevation angle. Since raindrops in drizzle are spherical, at low incident angles, the intrinsic Z_{DR} should theoretically be 0 dB, as the horizontal and vertical polarization returns would be the same. The calibration process begins by identifying regions of drizzle from the lowest Plan Position Indicator (PPI) scan, focusing on areas with copolar correlation coefficient (ρ_{HV}) exceeding 0.99 and signal-to-noise ratio (SNR) surpassing 10 dB. Furthermore, within these regions, Z values ranging from 0 to 20 dBZ are selected. All these together ensure we are selecting data from strong radar returns in drizzle. Care should be taken to avoid contamination from the melting layer and this can be achieved by considering data only below the melting layer. Subsequently, a scatter density plot consisting of Z_{DR} and Z samples in drizzle can be constructed. We can fit an empirical $Z - Z_{DR}$ relation and see when Z approaches 0 dBZ the Z_{DR} also should be 0 dB. Any deviation from that can be taken as the Z_{DR} bias. Another approach is to construct histograms

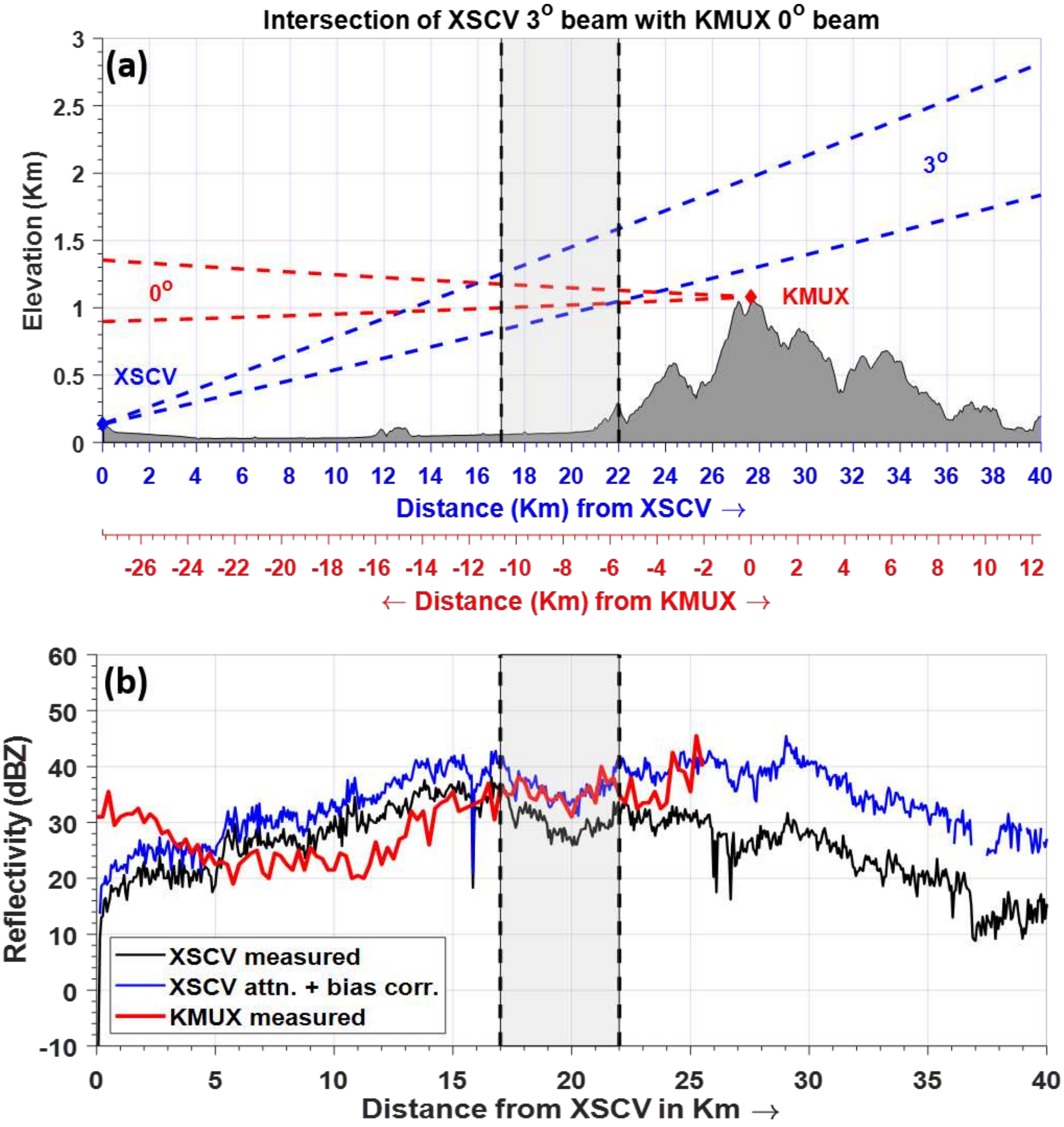

Figure 4.24: Comparison of reflectivity between XSCV and KMUX from a precipitation event on Jan 27, 2021, at 09:13:27 UTC. (a) Geometry of XSCV radar 2^o beam and KMUX radar 0^o beam along the baseline azimuth when both the radars are pointing at each other. (b) Ray profiles of reflectivities from the XSCV and the KMUX radar. The common volume is marked by vertical black lines in both (a) and (b).

of Z_{DR} samples in drizzle. The histogram should exhibit a Gaussian-shaped distribution centered around 0 dB. Any deviation of the median from 0 dB is indicative of bias. Figure 4.25 provides an illustration of the Z_{DR} bias calculation for the XSCV radar based on a precipitation event that occurred on Jan 27, 2021. In this instance, the median value of the Z_{DR} distribution is 0.44 dB, signifying that the measured Z_{DR} is greater by this amount.

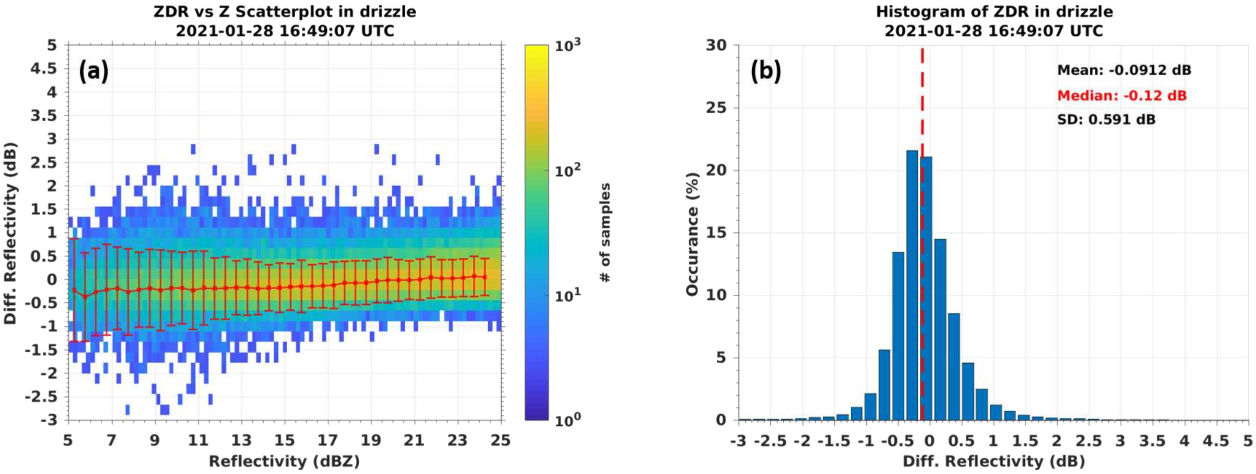

Figure 4.25: Example of Z_{DR} estimation of the XSCV radar using observations of drizzle from a precipitation event of Jan 27, 2021. (a) Scatter density plot of Z_{DR} vs Z from 2^o PPI scan in the drizzle. The red line denotes mean Z_{DR} for every 0.5 dB interval of Z with standard deviation bars. (b) Histogram of Z_{DR} in drizzle.

Chapter 5

Estimation of Orographic rainfall

5.1 Characteristics of Rain Drop Size Distribution

For analysis purposes, data from collocated Parsivel disdrometer and the profiler radars at the STR and MDT sites are selected corresponding to the 2016 to 2018 rainy season. DSD spectra collected from disdrometers are useful in identifying bulk microphysical properties of precipitation. The NOAA HMT Parsivel disdrometers are configured with a sampling resolution of 10 sec. Each of these samples contains the detected number of raindrops within the sampling interval which is arranged in a 32 by 32 drop size versus fall velocity matrix. This information represents the DSD spectra. The diameter size ranges from 0 to 25 mm with individual bin width increasing with the size from 0.125 to 3 mm. Detectable fall velocity values range from 0 to 20 m/s with each bin width increasing with fall velocity. Detailed technical information about the Parsivel disdrometer can be found in [75]. If each velocity bin is denoted by i and the diameter bin is denoted by j then the total number of raindrops T_d can be calculated as

$$T_d = \sum_{i=1}^{32} \sum_{j=1}^{32} n_{i,j} \tag{5.1}$$

where $n_{i,j}$ stands for number of drops in each bin. In order to improve the data reliability of the raw samples a series of data quality control procedures have been applied. First, each 10-sec sample is aggregated into 2 min intervals for minimizing random sampling errors. These 2 min samples help to better comprehend overall rainfall characteristics. In addition, raindrops from the lowest two bins are rejected due to the low signal-to-noise ratio. DSD spectra with a total number of drops less than 20 as well as spectra with derived rainfall rate less than 0.1 mm/h are removed from the analysis [76]. Furthermore, raindrops of diameters larger than 8 mm are not considered in order to avoid hail contamination according to [15]. Finally, the empirical terminal fall velocity versus drop diameter (V-D) relationship by [77] is adopted to mitigate contamination introduced by strong horizontal wind gradients and partially melted hydrometeors.

$$V(D) = 9.65 - 10.3e^{-0.6D} \tag{5.2}$$

Velocity measured by the disdrometer is compared to the Atlas relation in equation 5.2 for each diameter bin. Drops with measured velocities within a $\pm 50\%$ error are considered for further analysis. All of the above data quality control methods are applied to essentially restrict data to rain samples only. A total of 63,033 raw samples were studied out of which only 36,421 samples passed the quality control criteria. Figure 5.1 shows disdrometer data from 2016 to 2018 at STR and MDT sites before and after the quality control process. The number concentration of raindrops per unit volume for the j^{th} diameter bin can be calculated according to

$$N(D_j) = \sum_{i=1}^{32} \frac{n_{i.j}}{A \Delta t V_t \Delta D_j} \tag{5.3}$$

where $N(D_j)$ is in $m^{-3}mm^{-1}$; D_j is the j^{th} diameter bin in mm; A is the sampling area of the disdrometer which is 0.0054 m^2; Δt is the sampling time interval which is 120 sec; ΔD_j is the width of j^{th} diameter bin in mm; V_i is the value of fall speed for the i^{th} velocity bin in ms^-1. Rainfall rate R $(mm\ h^{-1})$ can be calculated based on $N(D)$ as

$$\begin{aligned} R &= 6\pi \times 10^{-4} \sum_{j=1}^{32} V(D_j) D_j^3 N(D_j) \Delta D_j \\ &= \sum_{j=1}^{32} R(D_j) \Delta D_j \end{aligned} \tag{5.4}$$

where $R(D_j)$ is the rainfall rate at the jth diameter bin. Furthermore, a normalized gamma DSD model first reported by [78] has been adopted in this study for calculating the median volume diameter D_0 (mm), mass-weighted mean diameter D_m (mm), and intercept parameter N_w

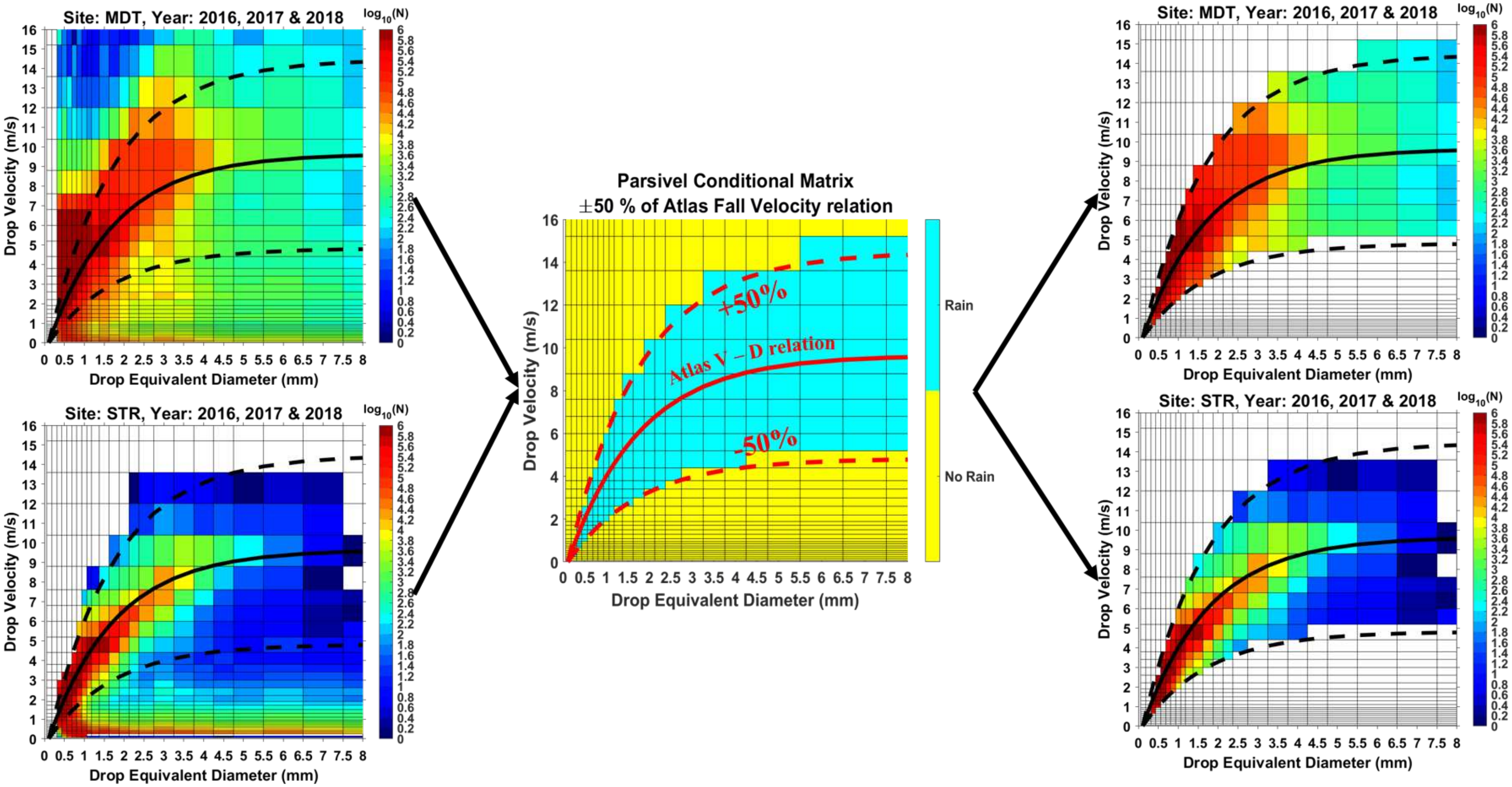

Figure 5.1: (a) and (b) shows raw disdrometer observations at MDT and STR sites respectively from the year 2016 to 2018 presented in a fall velocity vs drop diameter color density plot. (c) represents the Parsivel Conditional Matrix matrix used for quality control purposes. The ideal Atlas fall velocity vs drop diameter curve is shown by a solid black line whereas dashed black lines denote ±50% tolerance. The region within the dotted lines (shaded in blue) is considered as rain. The region outside (shaded in yellow) is no rain. (d) and (e) are quality-controlled disdrometer observations at MDT and STR sites respectively

$(m^{-3}\ mm^{-1})$. The normalized gamma DSD can be described as

$$N(D) = N_{\mathrm{w}} f(\mu) \Big(\frac{D}{D_m}\Big)^{\mu} \text{exp}\Bigg[-(4+\mu)\frac{D}{D_m}\Bigg] \tag{5.5}$$

Here, $f(\mu)$ is given by

$$f(\mu) = \frac{6(4+\mu)^{\mu+4}}{4^4\Gamma(\mu+4)} \tag{5.6}$$

where μ is the shape parameter and Γ is the Euler Gamma function. D_m can be expressed as a ratio of the fourth-order moment of $N(D_j)$ to the third-order moment of $N(D_j)$ as follows:

$$D_m = \frac{m_4}{m_3} \tag{5.7}$$

where the nth-order moment m_n of $N(D_j)$ is defined as

$$m_n = \sum_{j=1}^{32} D_j^n N(D_j) \Delta D_j \tag{5.8}$$

The median volume diameter D_0 is defined such that drops smaller than D_0 contribute to half the total liquid water content W $(g\ m^-3)$ as follows

$$\begin{aligned} \int_0^{D_0} D^3 N(D) dD &= \frac{1}{2}\int_0^{\infty} D^3 N(D) dD \\ &= \frac{1}{2}(W) \end{aligned} \tag{5.9}$$

It is also related to D_m as

$$\frac{D_0}{D_m} = \frac{3.67+\mu}{4+\mu} \tag{5.10}$$

N_w is calculated as

$$N_{\mathrm{w}} = \frac{4^4}{\pi}\Big(\frac{10^3 W}{D_m^4}\Big) \tag{5.11}$$

It should be noted that rainfall accumulations of individual events from 2016 to 2018 for Parsivel disdrometer data and the collocated tipping-bucket type rain gauges were generally in agreement to within $10\% - 15\%$. A close agreement between Parsivel rainfall rate retrievals and those from the robust 2D video disdrometer measurements was also reported by [79]. This gives an additional indication of the suitability of using the Parsivel disdrometer data.

5.2 Rainfall Classification based on S-Band Profiler Radar observations

Stratiform rain is characterized by precipitation that extends well above the melting layer. Below the freezing point of $0°$ C, hydrometeors consist of aggregated snowflakes. As these aggregates descend and encounter the melting layer, they begin to undergo a melting process from the outer layers inward. During this phase, the previously frozen hydrometeors develop an outer coating of liquid water, leading them to appear as large liquid drops when observed by radar. Given that the radar reflectivity factor (Z_H) is highly sensitive to the sixth power of drop diameter, there is a significant increase in Z_H at the level of the melting layer. This elevation in reflectivity is accompanied by a decrease in both differential reflectivity (Z_{DR}) and copolar coherency ratio (ρ_{HV}). This characteristic radar signature is known as the "bright band" and, as a result, stratiform rain is also commonly referred to as bright band (BB) rain. Below this region, the large liquid drops continue to fall, fully melting into smaller droplets due to aerodynamic instability. Conversely, orographic rainfall is primarily associated with a warm rain process, where rainfall is relatively shallow and influenced by the presence of topography. In this scenario, precipitation is mostly confined below the melting layer, and there are no large snowflake aggregates. Instead, numerous water droplets grow in size through condensation, aided by upslope flow and the coalescence of droplets within a relatively shallow layer near the terrain. In this study, both stratiform and orographic rain are identified as predominant rainfall types.

The classification of different rainfall types in the study conducted by [7] was based on vertically pointing S-PROF radar measurements, analyzed on a profile-by-profile basis during half-hour intervals. The categories used in this classification were warm rain, cold rain, hybrid rain, and convective rain. If multiple rainfall types were observed during a specific half-hour period, the rain type with the most distinct profiles was assigned to the entire period. For analysis in this study, BB rain is treated as a single category, without further subdivision into cold and hybrid rain, as both exhibit the bright band signature. In contrast, warm or orographic rain is considered as non-bright band (NBB) rain. Convective periods, which constituted less than 5% of the total rainy period, were excluded from examination. It is important to note that while the bright band signature is typically obscured in convective rain, it can also be regarded as NBB rain. However, since convective rain is not the focus of this study, the NBB terminology primarily refers to warm or orographic rain. The quality-controlled drop size distribution (DSD) samples are classified into BB and NBB rainfall categories based on simultaneous observations from the collocated S-PROF radar at the STR and MDT sites.

In Figure 5.2, we can observe the total drop counts plotted against drop equivalent diameters at both observation sites. For the purposes of this study, drops with diameters less than 1.5 mm are categorized as small drops, those with diameters ranging from 1.5 to 3 mm are considered mid-sized drops, and drops larger than 3 mm fall into the category of large drops, following the classification proposed by [80] and [75]. A notable trend emerges from this analysis: NBB rain exhibits a higher frequency of small raindrops at both the STR and MDT sites, whereas BB rain is associated with a higher frequency of mid-sized to large drops. The transition from small to mid-sized and larger drops occurs within a range of 0.75 mm to 1.15 mm in drop diameter for both sites. However, it's worth noting that there is a more pronounced distinction between mid-sized and large drops at the STR site compared to the MDT site. Furthermore, the MDT site demonstrates a higher number concentration of smaller drops compared to the STR site. This observation suggests the dominance of the orographic process at MDT, likely resulting from the rapid upward movement of air caused by the local mountainous topography. These trends are further illustrated by the probability distribution of mass-weighted mean diameter (D_m), median diameter (D_0), and normalized intercept parameter (N_w) in Figure 5.3.

In this figure, BB rain is denoted by blue and NBB rain is denoted by orange. D_0 and D_m both have similar positively skewed distributions in BB and NBB rain. It can be seen that, although

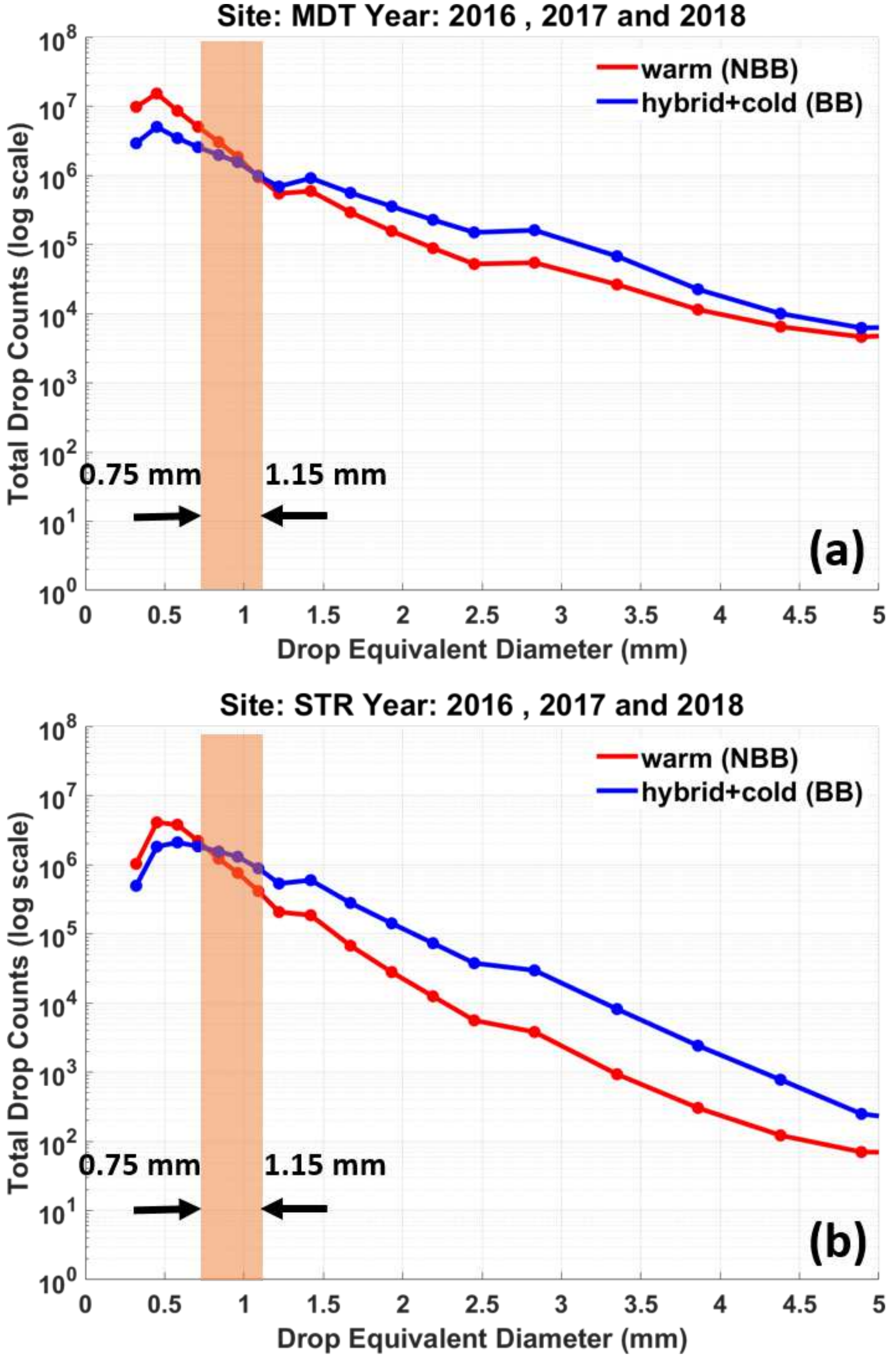

Figure 5.2: Total drop counts vs drop equivalent diameter in NBB rain and BB rain at (a) MDT site and (b) STR site based on data from the 2016 - 2018 rain seasons. The shaded region in (a) and (b) indicates the crossover between small and large-sized drops.

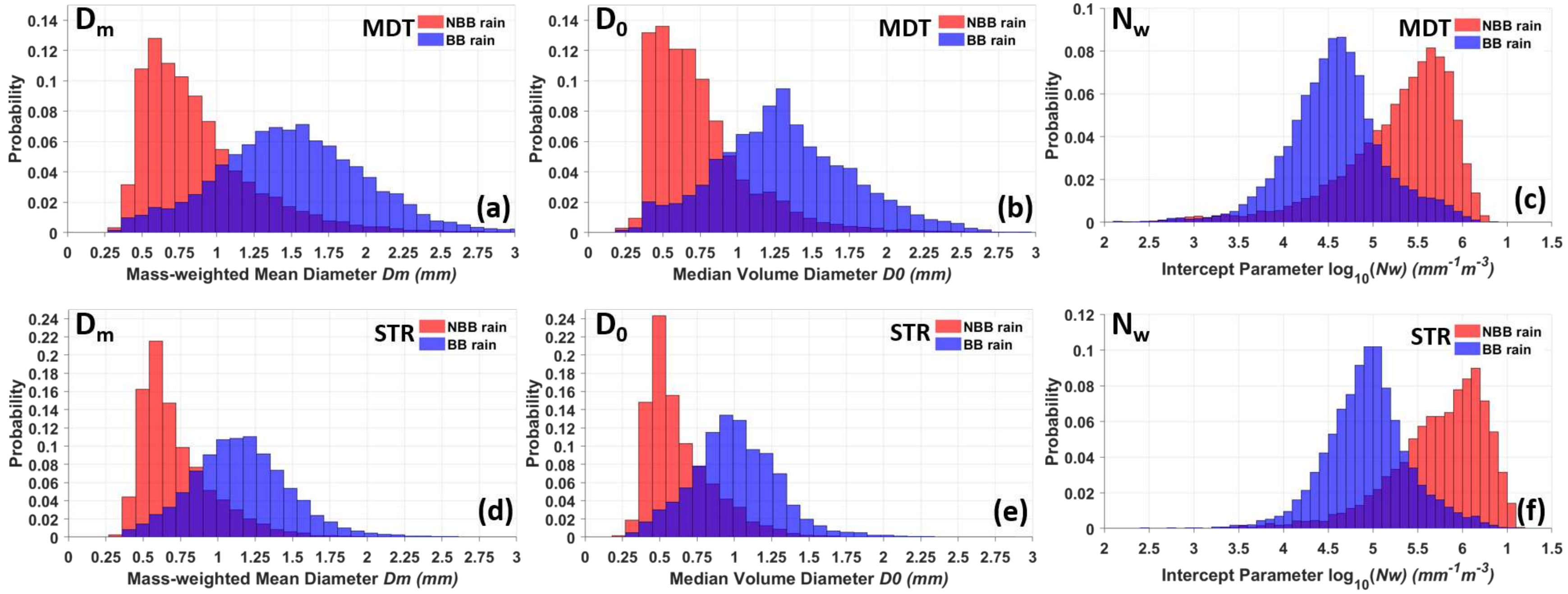

Figure 5.3: Histograms of (a,d) D_m, (b,e) D_0, and (c,f) $log_{10}N_w$ at the (top) MDT and (bottom) STR sites calculated from DSD data from the 2016 - 2018 rain seasons.

there is some overlap, NBB rain in general has a higher probability of a smaller drop diameter compared to BB rain whereas BB rain has a higher probability of a bigger drop diameter. The N_w distribution of NBB rain is negatively skewed at both sites while the distribution of N_w in BB rain is symmetric. This supports the findings in Figure 5.2 that NBB rain has a higher concentration of overall drop counts compared to BB rain.

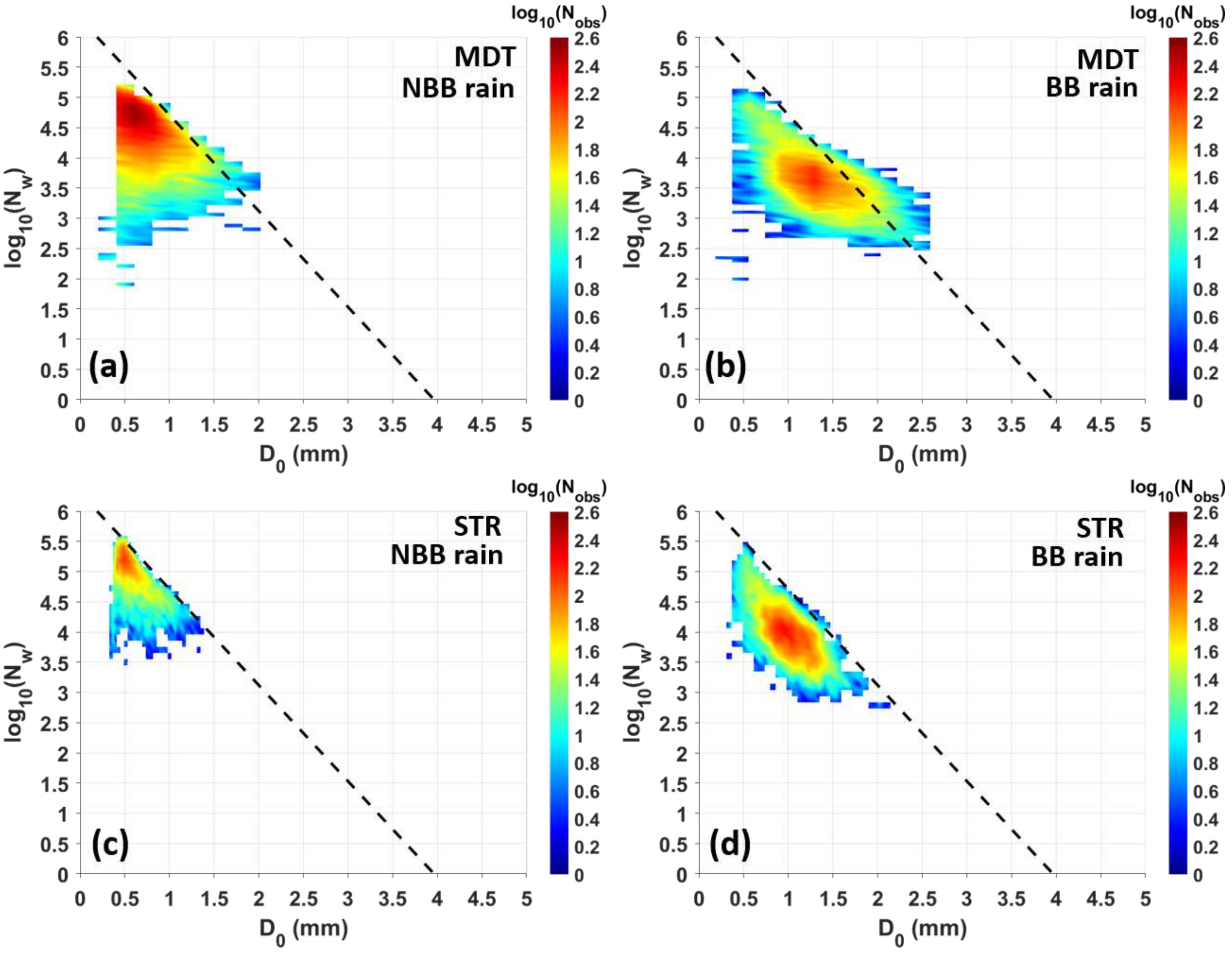

Figure 5.4: Scatter density plots of $log_{10}N_w$ versus D_0 in (a,c) NBB and (b,d) BB rain at the (top) MDT and (bottom) STR sites. The black dashed line signifies stratiform and convective separation based on equation 5.12

Figure 5.4 presents scatter density plots of $log_{10}N_w$ versus D_0 for BB and NBB rain at the two sites. The black dotted line is given by the equation

$$log_{10}N_w^{sep} = -1.6D_0 + 6.3 \tag{5.12}$$

This empirical relation is used to separate stratiform rain from convective rain [81, 82]. As expected almost all samples fall in the stratiform region. In summary, it can be concluded that NBB rain observations at both sites exhibit higher concentrations of smaller drops compared to BB rain. For both rain types, the mean values of D_0 are larger at MDT compared to STR. The dominance of orographic enhancement at MDT is clearly indicated due to a higher concentration of small drops.

5.3 Rainfall Type Classification Based On Dual-Pol Parameters at X-Band

Distinguishing between BB rain and NBB rain using vertical profiler radar data, which provides profiles of radar reflectivity (Z) and Doppler velocity, is relatively straightforward. However, performing the same classification with PPI (Plan Position Indicator) scans from weather radars presents certain challenges. Previous research by [83–85] has predominantly focused on detecting the bright band (BB) and correcting for the vertical profile of reflectivity (VPR) using polarimetric scanning radar data. [9] demonstrated the potential of using polarimetric radar variables at the S-Band to identify BB and non-bright band (NBB) rain types. However, the exploration of polarimetric relationships at the X-Band, particularly in the context of classifying rain types, has not been extensively addressed. This study is dedicated to developing a robust methodology for distinguishing between stratiform (BB) and orographic (NBB) rain types. The goal is to create an approach that can be applied to real-time scanning X-Band radar data.

Polarimetric radars, which are sensitive to drop shapes, offer a promising avenue for this classification. In cases where NBB rain is characterized by a higher concentration of small drops, the predominant drop shapes observed within the radar resolution volume will tend to be more spherical compared to BB rain. Consequently, polarimetric radar has the potential to not only discern different rain types but also provide more accurate estimates of rainfall intensity compared to single polarization measurements [42]. In situations where Rayleigh scattering prevails, the particle sizes are considerably smaller than the radar wavelength, allowing the radar reflectivity factor to be approximated as approximately equivalent to the sixth moment of the drop size distribution. However, this approximation often breaks down when large drops are present, particularly at a wavelength of 3 cm, corresponding to X-Band radar. Therefore, in this study, dual-polarization parameters specific differential phase (K_{DP}) in degrees per kilometer and differential reflectivity (Z_{DR}) in decibels (dB), along with reflectivity at horizontal polarization (Z) in dBZ, were computed using the T-Matrix scattering method [27]. The computation was based on quality-controlled two-minute drop size distribution (DSD) samples categorized into BB and NBB rain. A Gamma distribution was assumed for the drop size distribution, and drops were considered symmetric, with an orientation canting angle following a Gaussian distribution with a zero mean and a standard deviation of 5^o. The drop shape model described in [86] was applied. The computed Z and Z_{DR} values for BB and NBB rain from the DSD samples at both observation sites are presented in Figure 5.5 as scatter density plots.

Notably, the distributions of Z_{DR} versus Z exhibit distinct differences between non-bright band (NBB) and bright band (BB) rain. BB rain is characterized by higher Z and Z_{DR} values compared to NBB rain. In NBB rain, a substantial proportion of Z_{DR} values falls below 0.5 dB, indicating a larger fraction of smaller, spherical raindrops. To identify NBB and BB rain types based on the observed Z_{DR} versus Z patterns, a polarimetric approach is employed. However, due to the overlapping samples in the Z-Z_{DR} plots, distinguishing between the two rain types using a single threshold proves to be challenging. It's important to note that most of the significant overlap occurs at the lower values of Z and Z_{DR}, with a considerably lower number of overlapping samples corresponding to higher values. This is further illustrated in Figure 5.6, which is a scatter density plot of Z_{DR} versus Z for pixels with a sample size exceeding 50. An empirical relation is given by the equation

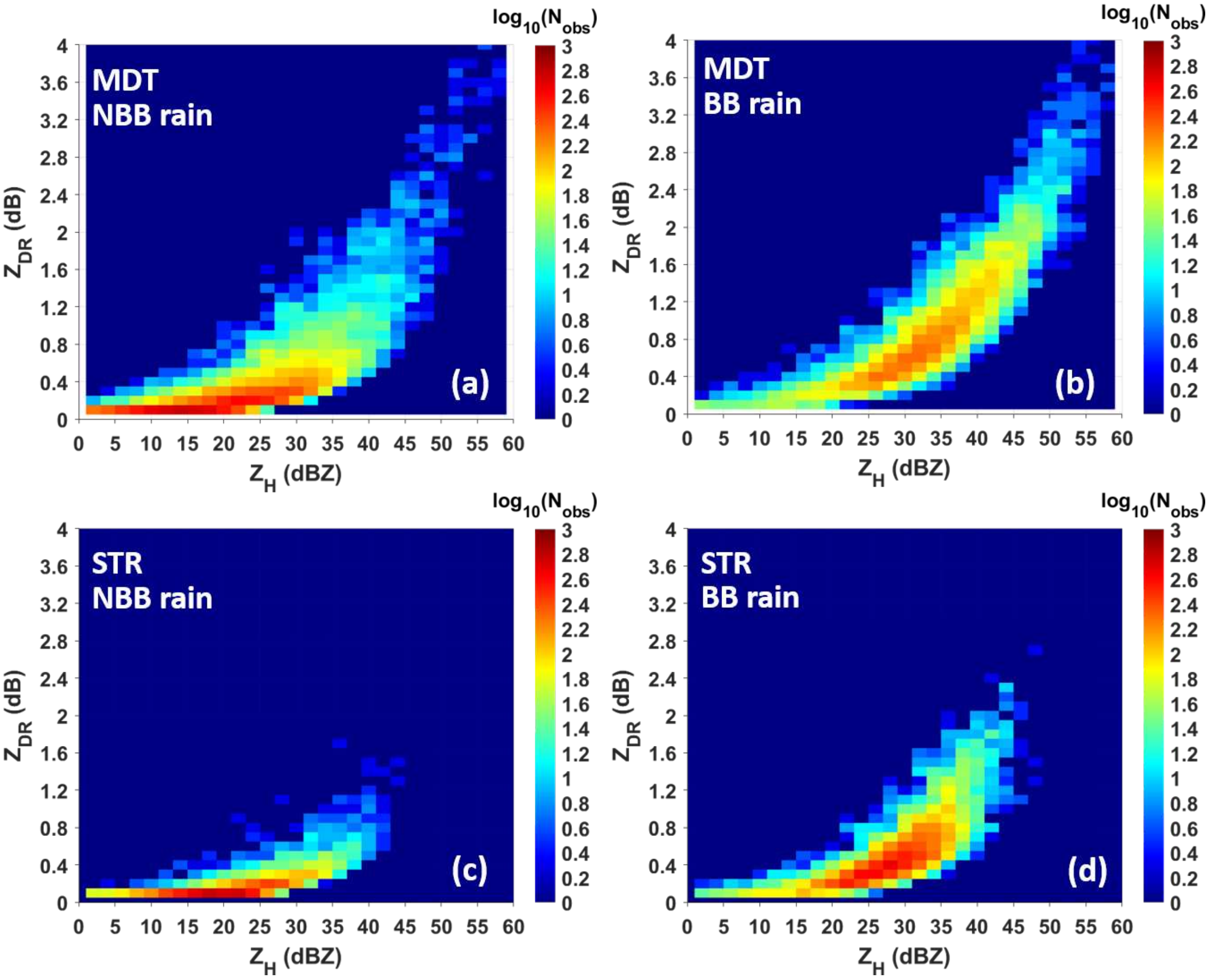

Figure 5.5: Scatter density plots of Z_{DR} versus Z_H in (a,c) NBB and (b,d) BB rain at the (top) MDT and (bottom) STR sites, calculated from the 2 min DSD spectra using T-Matrix scattering method.

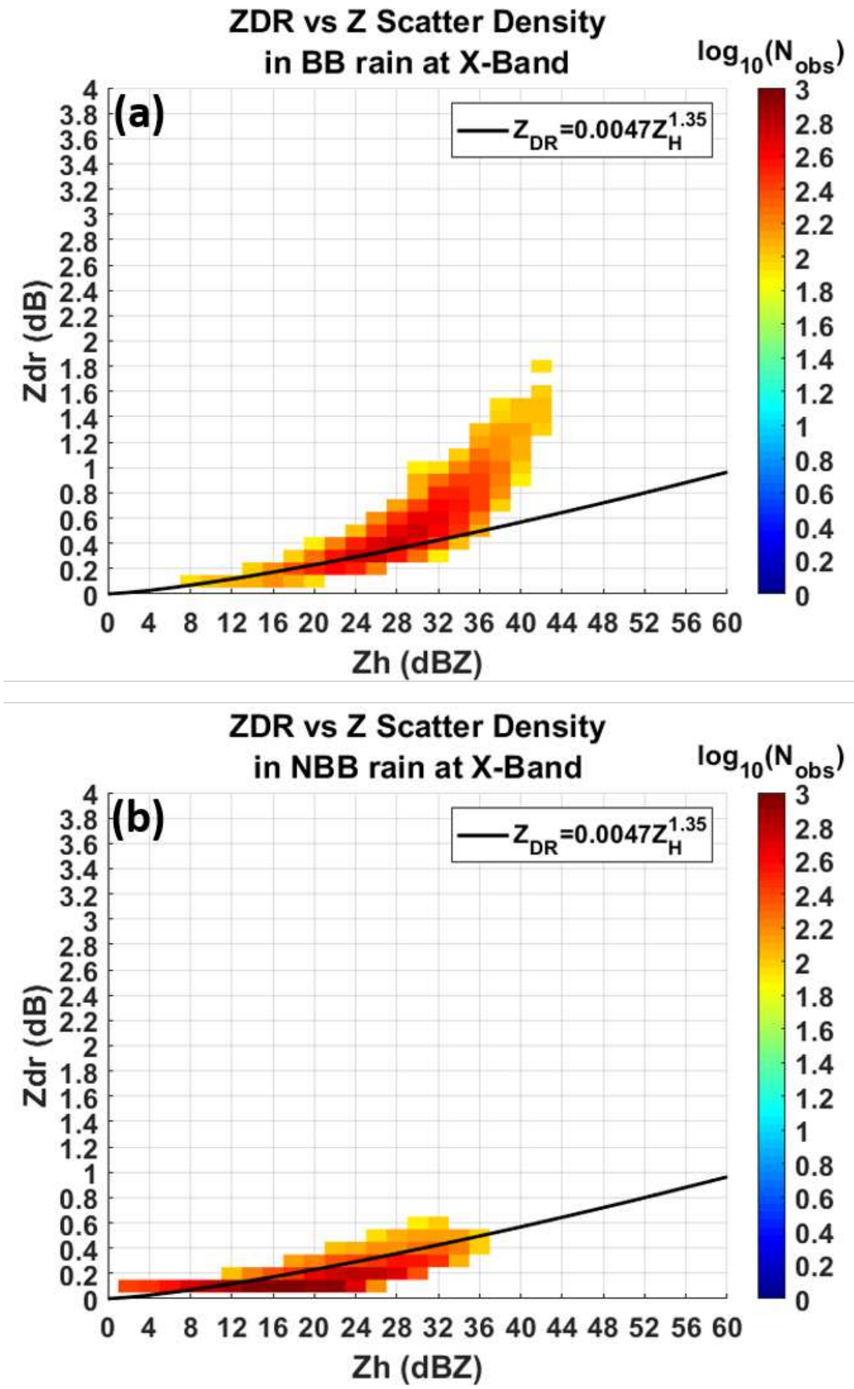

Figure 5.6: Classification of NBB versus BB rain in Z_{DR} versus Z_H space using the empirical relation in 5.13 denoted by a black curve. (a) Plot for NBB rain samples and (b) plot for BB rain samples combining data from both MDT and STR sites. It should be noted that only grid points with a sample density greater than 50 are considered.

$$Z_{DR}^t = 0.0047Z^{1.35} \tag{5.13}$$

is developed based on a fit to the data. It can be observed from Figure 5.6 that the black curve represented by equation 5.13 separates the two types of rainfall. For a given value of Z, the threshold Z_{DR} value for BB-NBB separation is denoted by Z_{DR}^t. If the observed Z_{DR} value is greater than this threshold then it is classified as BB rain and the opposite is true for NBB rain. It should be noted that in Figure 5.6 about 85% of the rain samples of either type are classified by equation 5.13. However, this approach is only applicable to radar observations of rain where there is no contamination from mixed-phase and ice hydrometers.

5.4 Dual-Pol Rainfall Rate Estimators

Rainfall rates R are retrieved by summation of individual rainfall rates at each disdrometer's diameter bin using equation 5.4. The calculated K_{DP} values and the corresponding rainfall rates from the DSD data are segregated for the two types of rain. Scatter density plots of R versus K_{DP} were made to get an overall trend of the rainfall rates compared to K_{DP}. This is shown in Figure 5.7a and b. The distributions were then fitted using an exponential curve which yielded two distinct equations. These two $R(K_{DP})$ estimators are given by

$$\begin{aligned} R_{BB} &= 18K_{DP}^{0.8} \\ R_{NBB} &= 23K_{DP}^{0.6} \end{aligned} \tag{5.14}$$

Since most of the K_{DP} values for the two types of rain are less than 1 deg/km, a lower exponent, as in the case of the NBB rain estimator, means a higher rainfall rate compared to the BB one. Figure 5.7c shows the density plot between rainfall rate versus K_{DP} when both BB and NBB samples are considered together. An exponential fit is also made to this distribution which is given by the

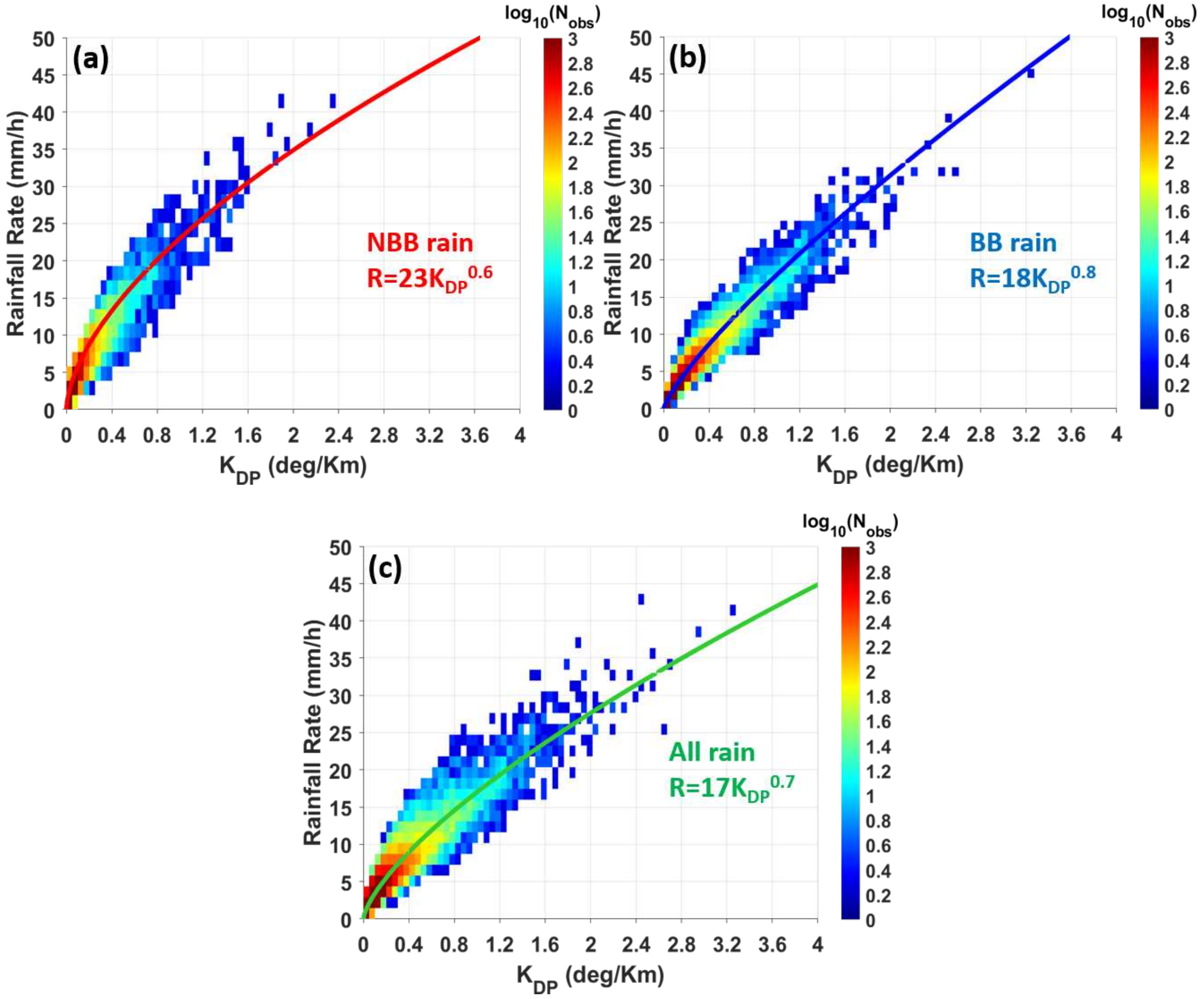

Figure 5.7: Rainfall Rate R versus Specific Differential Phase K_{DP} from disdrometer observations at the STR and MDT sites combined (a) for NBB rain samples (b) for BB rain samples (c) for both BB and NBB rain samples considered together

equation

$$R = 17K_{DP}^{0.7} \tag{5.15}$$

It is interesting to note that this exponential fit is quite different from either NBB or BB rains. The exponent lies between that of NBB and BB equations suggesting that it is an overall average fit. To demonstrate the significance of the hybrid $R(K_{DP})$ estimators on QPE, an orographic precipitation event on Oct 20, 2021, is chosen for analysis.

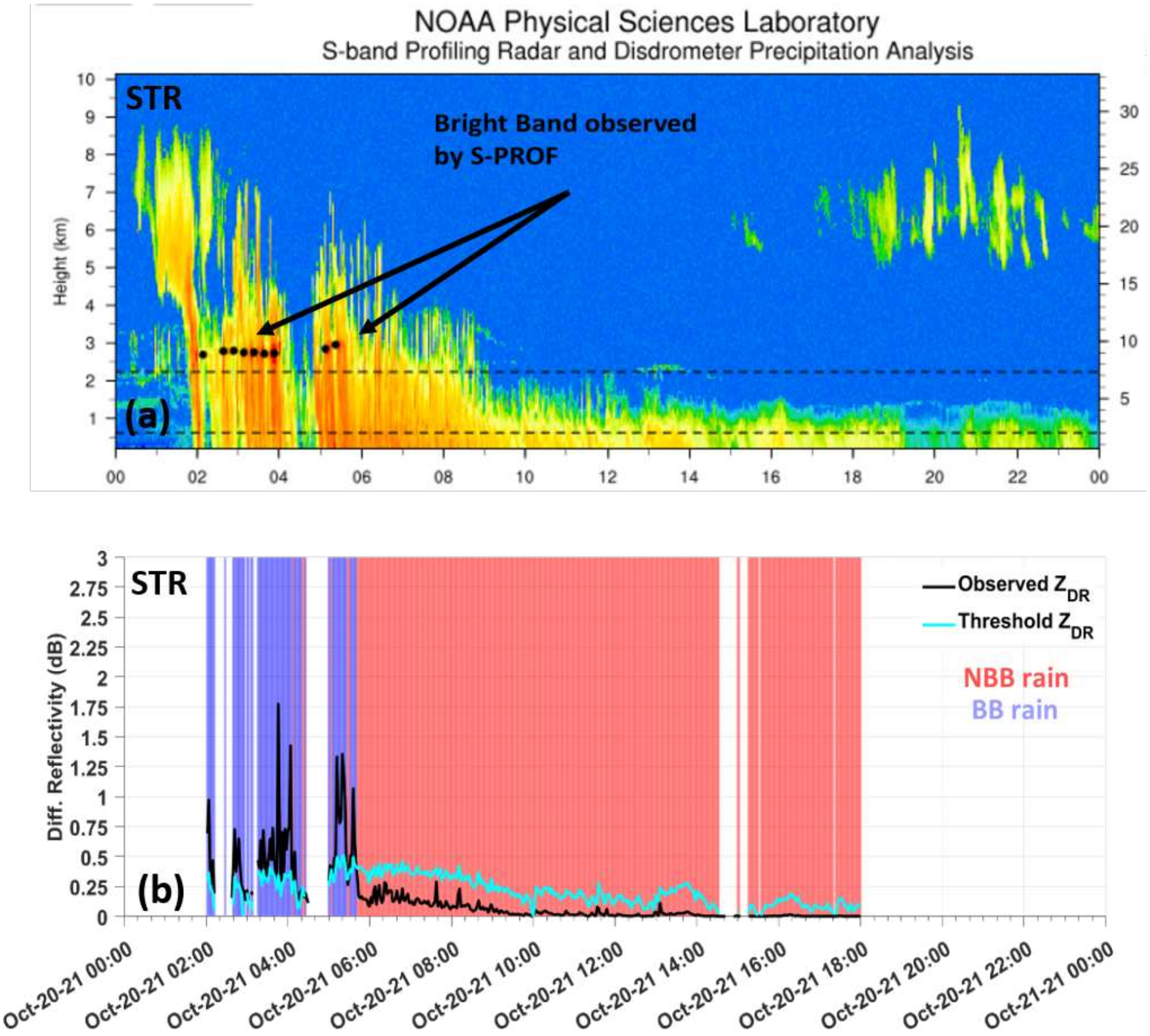

Figure 5.8: (a) Image of S-PROF Signal to Noise Ratio at the STR site for October 20 2021 precipitation event. The black dots represent the melting layer height. This image is taken from the website "https://psl.noaa.gov/data/obs/datadisplay/". (b) Classification of BB versus NBB rain at the STR site using dual-pol XSCW radar observations for the October 20 2021 precipitation event. The black and light blue lines represent observed Z_{DR} and threshold Z_{DR} calculated using equation 5.13 respectively. Periods of BB rain are shaded in blue while NBB rain is shaded in red.

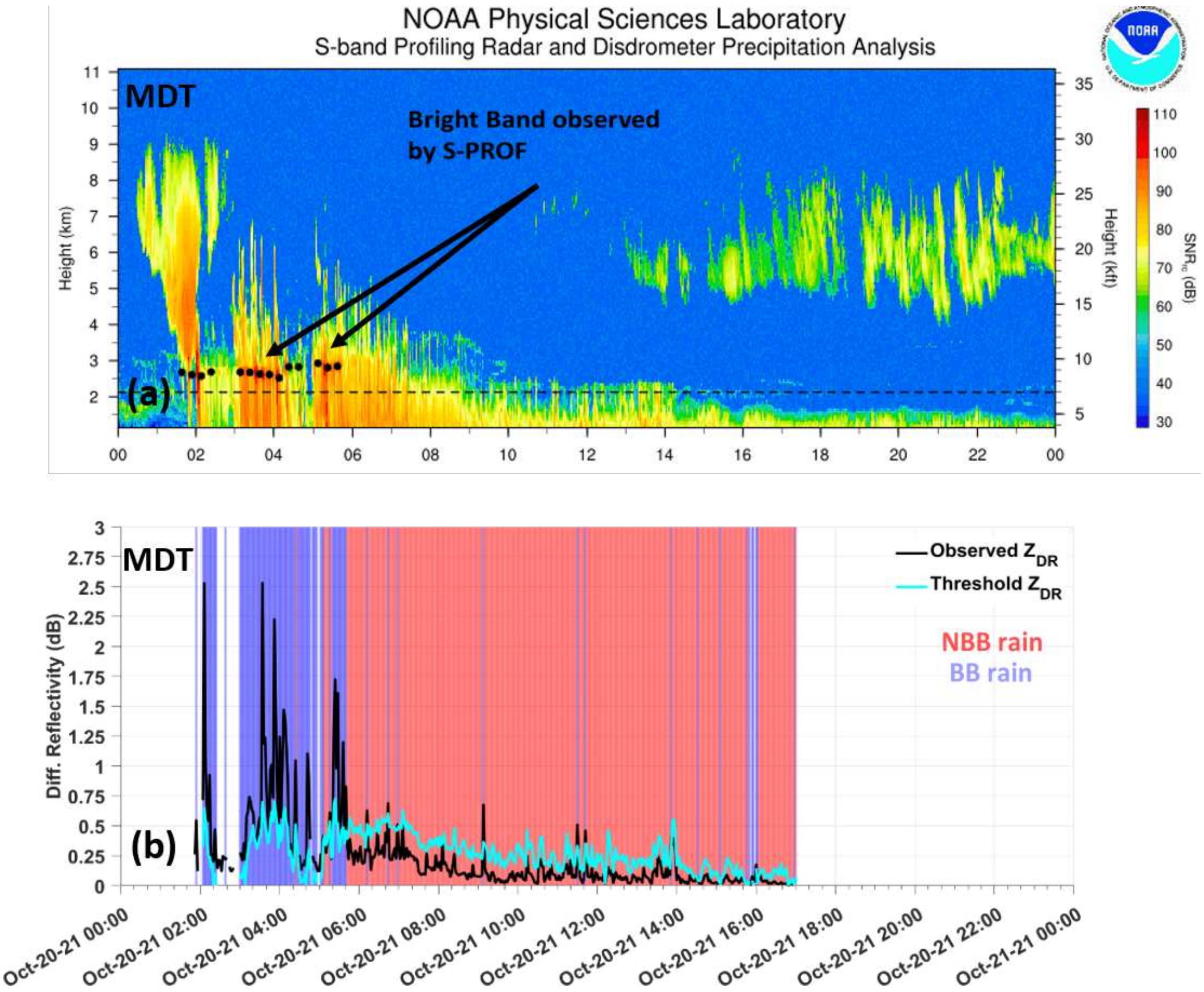

Figure 5.9: (a) and (b) are same as Figure 5.8 but for the MDT site

Figures 5.8 and 5.9 show BB vs NBB classification at the STR and MDT sites following the method developed in this study. Figures 5.8a and 5.9a are images of the S-SPROF radar SNR at the STR and MDT site respectively. These images are taken from the NOAA PSL web display. Figure 5.8b and 5.9b show time series of measured Z_{DR} at the two sites. The black line depicts observed Z_{DR} whereas the light blue line denotes the Z_{DR} threshold calculated from the relation in equation 5.13. The blue shaded periods correspond to BB rain whereas the orange shaded periods corresponds to NBB rain. The classification based on X-Band dual-pol observations in Figures 5.8b and 5.9b is found to be consistent compared to the S-PROF observations. The occurrence of BB rain can be observed approximately until around 06:00 UTC, after which it is all NBB rain. The hybrid $R(K_{DP})$ estimator is applied according to the rainfall type classification and subsequently, rainfall accumulations are calculated for each hour for the whole event at both sites. Hourly rainfall accumulations are also calculated using the average $R(K_{DP})$ relation, given by equation 5.15. The radar estimates are compared against the tipping bucket rain gauges present at both sites. In addition, two operational QPE products namely the MRMS MultiSensor Pass1 and MRMS RadarOnly are also compared. Detailed descriptions of the MRMS products can be found in [18] and [87]. Both of these operational products provide hourly estimates of rainfall over the CONUS.

Figures 5.10 and 5.11 show comparison of the hourly rainfall estimates obtained from the rain gauge measurements with the hybrid $R(K_{DP})$ and the average $R(K_{DP})$. It is interesting to note that, both in figures 5.10b and 5.11b that the hourly rainfall estimates calculated using the average $R(K_{DP})$ slightly overestimates during the BB periods with significant underestimation during the NBB periods. In contrast, the radar estimates using the hybrid $R(K_{DP})$ estimators, as shown in figures 5.10a and 5.11a, performs very well. This can be observed in the rainfall cumulative accumulation comparison in figures 5.10c and 5.11b. Both of the MRMS QPE products as well as the rainfall estimate using average $R(K_{DP})$ tends to significantly underestimate. Oftentimes, at very low rainfall rates the estimated K_{DP} from radar observations of differential phase can be very noisy. In addition, K_{DP} can be affected by bright band contamination when the lowest radar

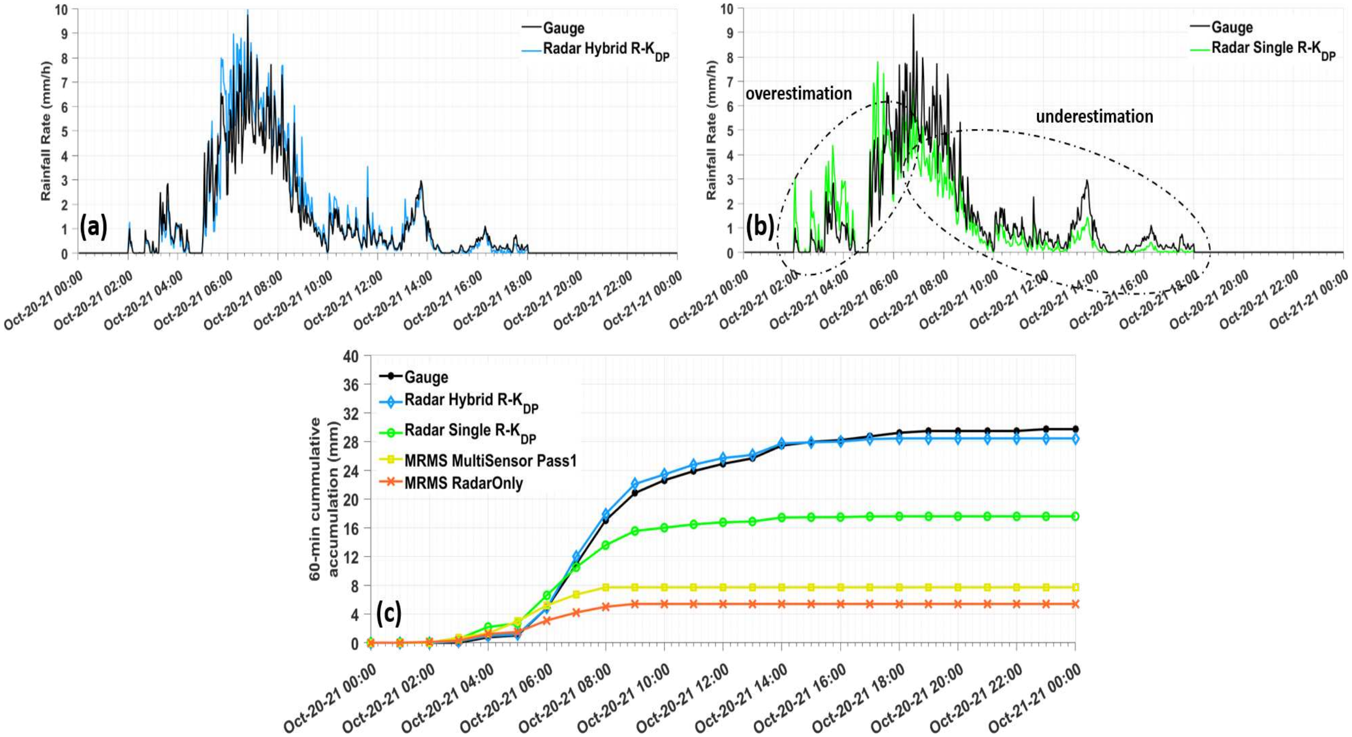

Figure 5.10: Comparison of different rainfall products with a rain gauge at the STR site for the October 20, 2021, precipitation event. (a) Rainfall Rate using hybrid $R(K_{DP})$ vs gauge rainfall (b) Rainfall Rate using a single $R(K_{DP})$ relation vs gauge rainfall. (c) Cumulative accumulation of hourly rainfall at the STR rain gauge location from different rainfall products.

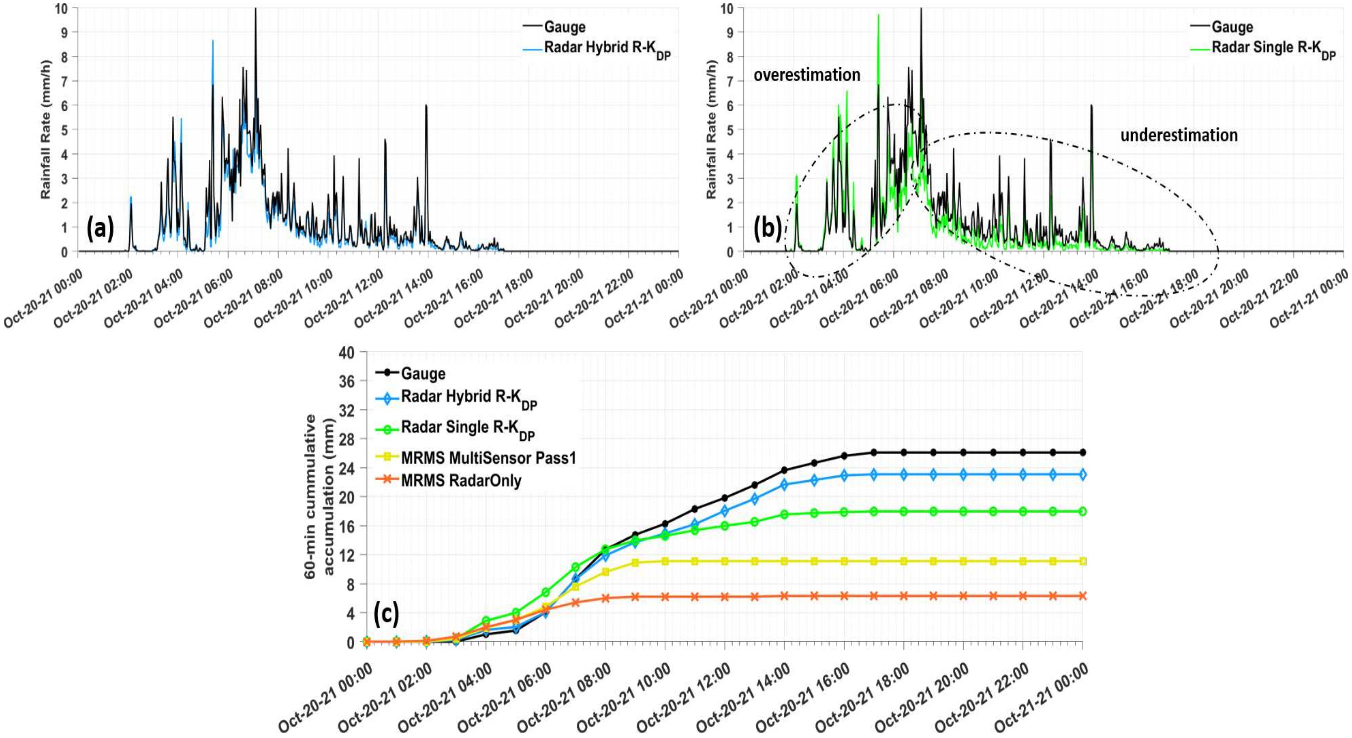

Figure 5.11: Comparison of different rainfall products with a rain gauge at the MDT site for the October 20, 2021, precipitation event. (a) Rainfall Rate using hybrid $R(K_{DP})$ vs gauge rainfall (b) Rainfall Rate using a single $R(K_{DP})$ relation vs gauge rainfall. (c) Cumulative accumulation of hourly rainfall at the MDT rain gauge location from different rainfall products.

scans are intersected by the melting layer being very close to the ground. In these scenarios, it is not advisable to use K_{DP} for estimating rainfall and use Z instead. In case of bright band contamination, appropriate correction of the reflectivity vertical profile should be performed before using the $R(Z)$ estimator. Thus, apart from the $R(K_{DP})$ relations, $R(Z)$ relations for both BB and NBB rain are also developed using the disdrometer measurements. They are given by

$$\begin{aligned} R_{BB} &= 0.15 Z_{lin}^{0.43} \\ R_{NBB} &= 0.3 Z_{lin}^{0.41} \end{aligned} \tag{5.16}$$

where Z_{lin} is reflectivity in linear units $(mm^6\ m^{-3})$. Figure 5.12 presents the $R(Z)$ estimators.

5.5 VPR correction and QPE Blending

Oftentimes, in the Bay area, environmental freezing levels are situated close to the ground, typically less than 1 kilometer above ground level (AGL). In such circumstances, particularly at extended range distances, even during surface rainfall, the radar's resolution volume may be partially or entirely occupied by mixed-phase hydrometeors within a melting layer or snow particles located above the freezing level. These situations are more common when dealing with longer-wavelength operational radars, as radar beams at even the lowest elevation angles of 0.5 degrees tend to broaden and extend in height with increasing distance. To address the impact of these conditions on reflectivity-based rainfall estimations, one approach involves using a priori knowledge of the vertical profile of reflectivity (VPR) [88]. Following this approach, the measured reflectivity at higher altitudes is statistically related to the expected reflectivity at ground level. This estimated ground-level reflectivity is then employed for quantitative precipitation estimation (QPE). Previous showed that for ranges of less than 100 kilometers, applying a VPR correction can improve reflectivity-based rainfall estimates obtained from NEXRAD radars by a factor ranging from 1.5 to 2.

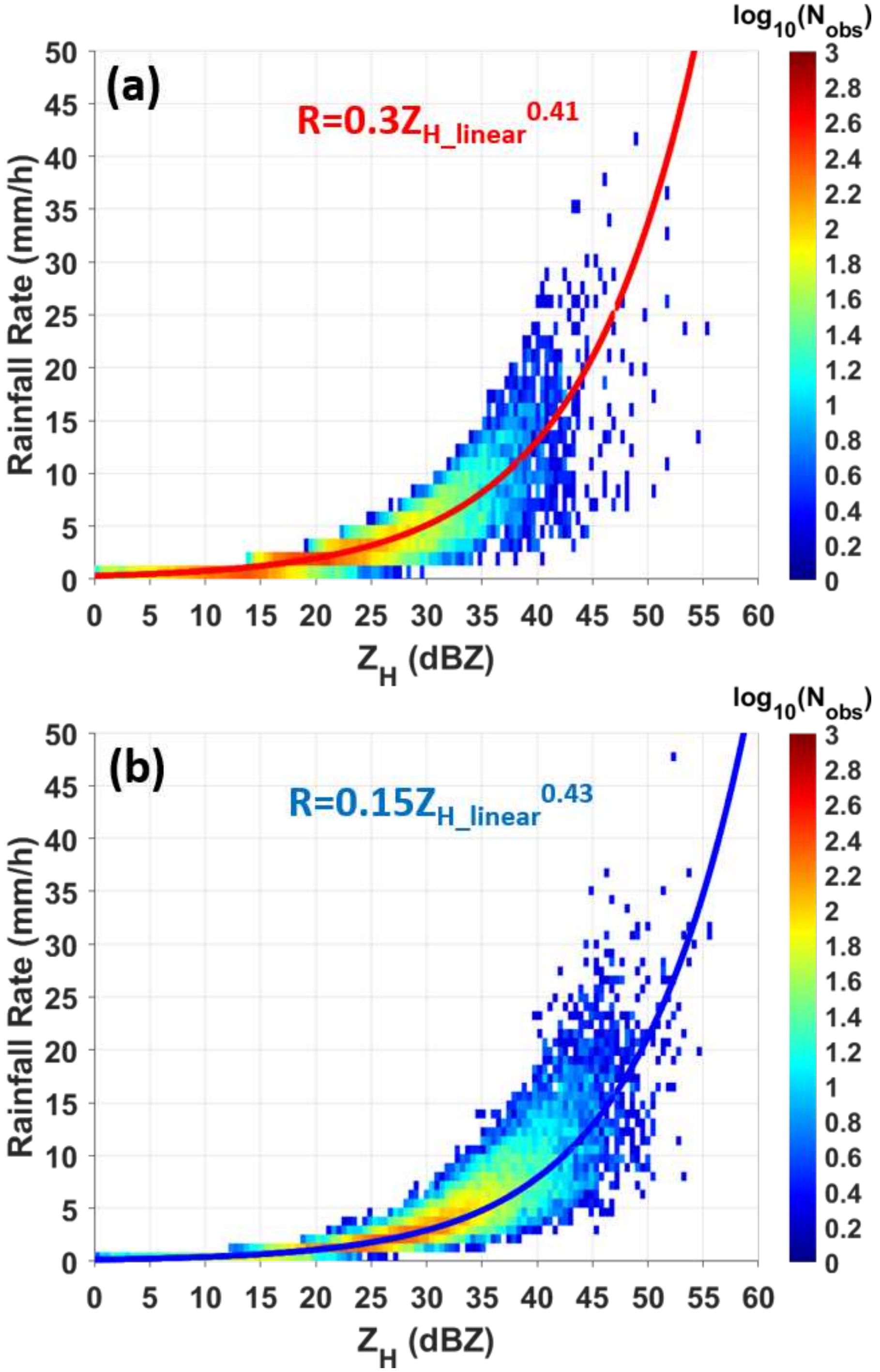

Figure 5.12: Rainfall Rate R versus Reflectivity Z in BB and NBB rain

Figure 5.13 shows an example of the XSCV X-Band radar 2^o beam intersecting the melting layer when the environmental freezing level is at 1 km. In cases of stratiform rain, when the radar beam observes below the freezing level, the QPE product is based on R(KDP). On the other hand, When the radar beam samples the melting layer in the BB region, the QPE product is based on R(ZH) along with a VPR correction applied.

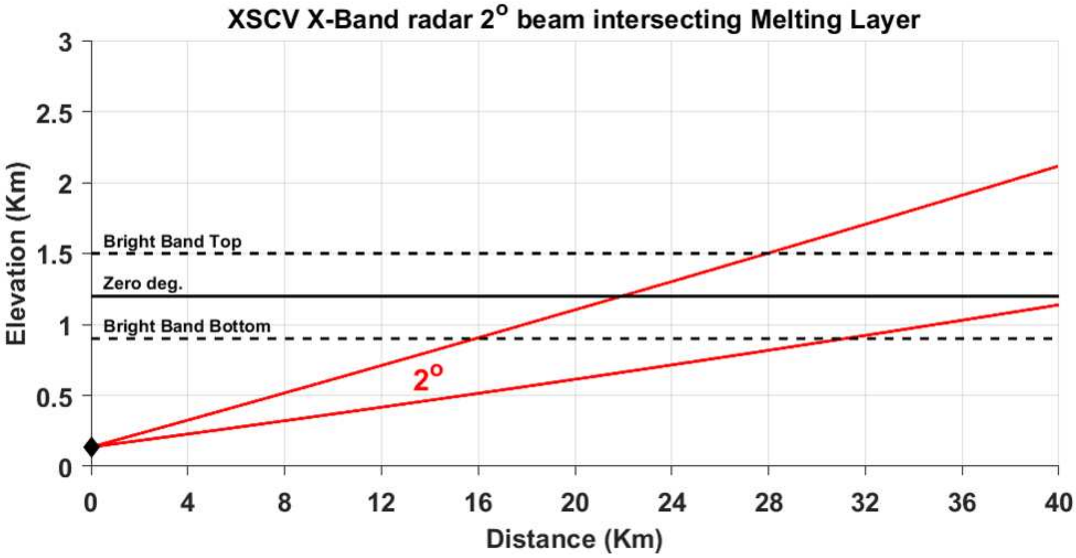

Figure 5.13: Example of the XSCV 2^o beam intersecting the freezing level.

It can be observed from the figure that rainfall estimators are switched from $R(K_{DP})$ to $R(Z_H)$ when the centerline of the radar beam intersects the bright band bottom. It was mentioned earlier in Chapter 4 that the XSCW radar performs RHI scans along with PPIs. Vertical profiles of reflectivity are constructed from the RHI scans from ranges 10 km to 40 km. A mean profile of the VPR is presented in Figure 5.14. This mean profile is used for aiding in the VPR correction. Since the XSCV radar does not do RHI scans, this mean VPR is used for the XSCV VPR correction as well.

First, BB top and BB bottom heights are identified from the mean profile. Ground level reflectivity values are considered from 0 km to the BB bottom height. The highest scan beam top height is determined and reflectivity values from BB bottom to this beam top height are considered as

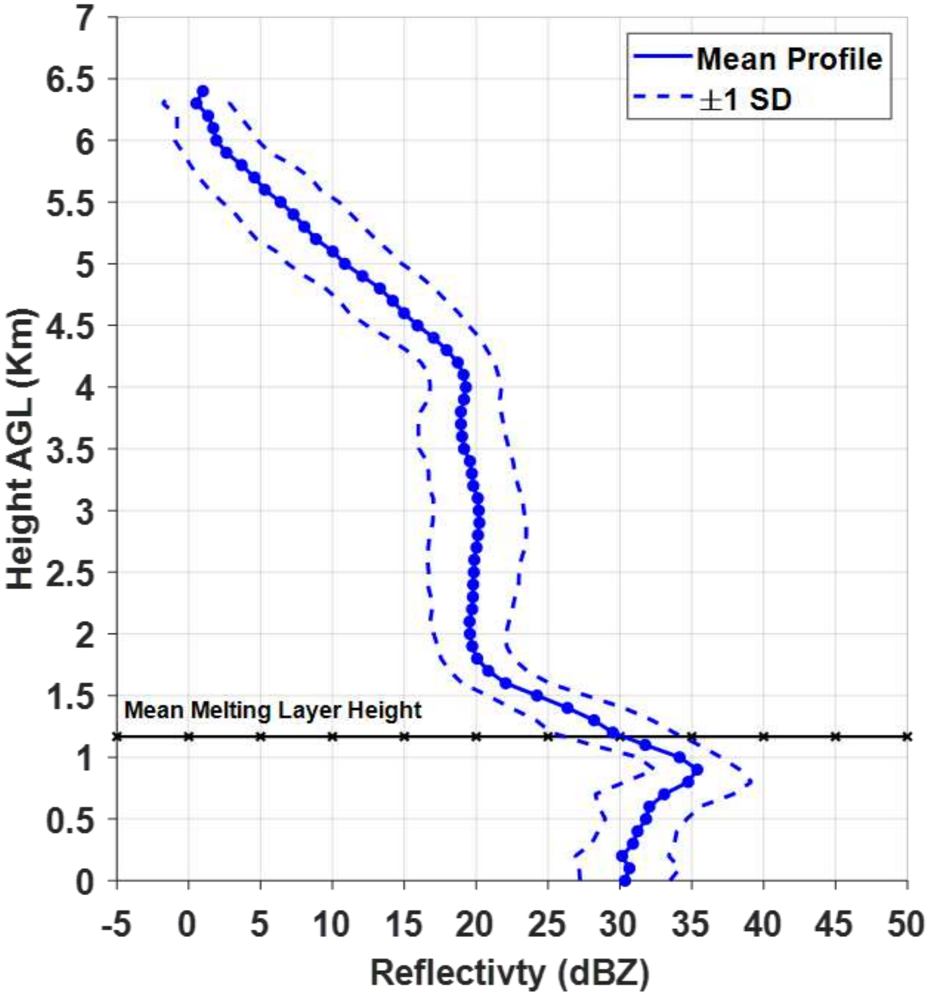

Figure 5.14: Mean vertical profile of reflectivity constructed from XSCW radar RHI scans. The dashed blue lines denote the ±1 standard deviation. The black solid line represents the environmental freezing height. The black dashed lines represent the melting layer top and bottom heights.

reflectivity in and above the BB region. A power law relation is calculated based on these two sets of reflectivity given as

$$Z_{H(ground)} = 11.1 Z_{H(above)}^{0.3} \tag{5.17}$$

This relation is applied for VPR correction at regions above the BB bottom height. It should be noted that no VPR correction is required for NBB rain profiles since NBB rain forms by warm rain processes below the freezing level [6].

Figure 5.15 shows a flowchart of the rainfall estimation algorithm based on the BB and NBB rain type delineation.

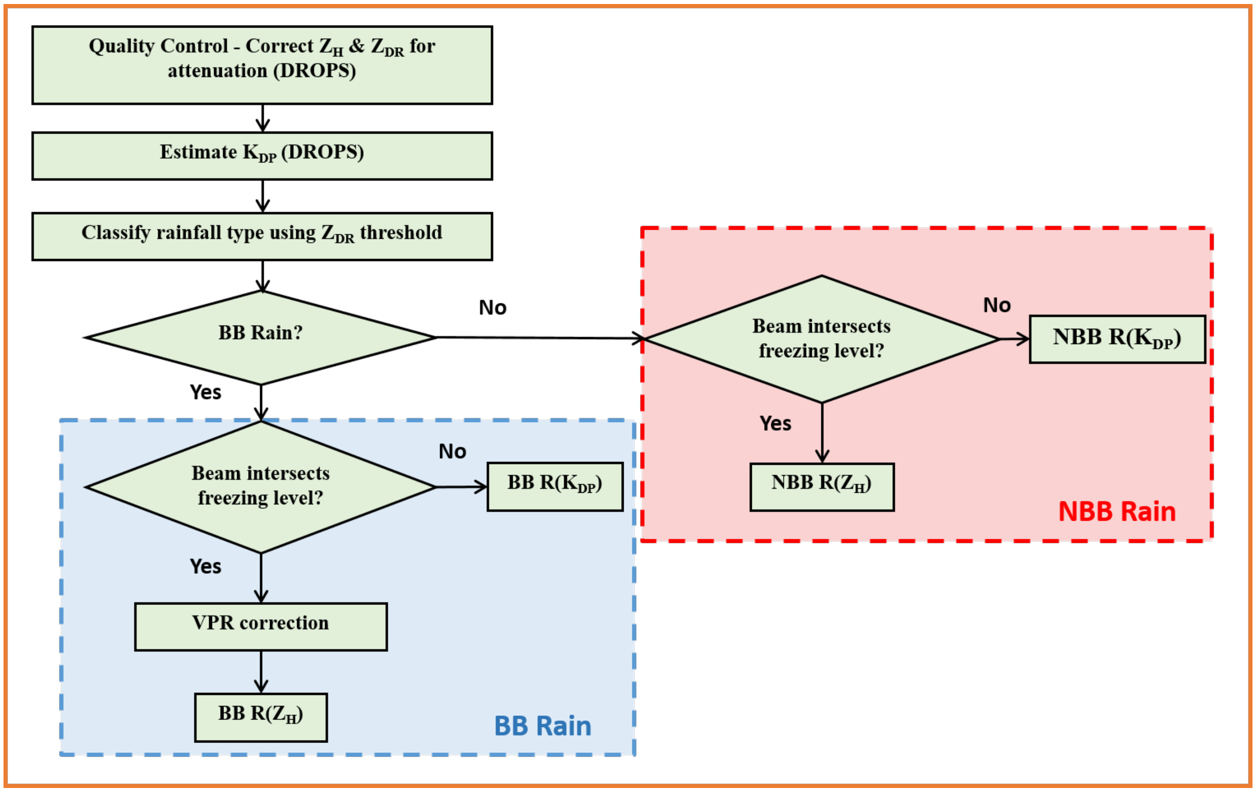

Figure 5.15: Flowchart representing rainfall rate estimation based on BB versus NBB rain classification.

A combination of both $R(Z)$ and $R(K_{DP})$ estimators are used in case of precipitation events when the freezing level is close to the ground. When generating QPE maps over the entire radar domain, there could be an abrupt change in the spatial structure of rainfall due to the usage of different estimators that might lead to an impression of unnatural estimates. This issue can be addressed by combining the different estimates at ranges corresponding to the BB bottom height by a blending method. Therefore a blend between the two rainfall types is implemented which will produce a reasonable spatial structure while preserving estimation accuracy. The rainfall rate blending is done following Equation 5.18.

$$R = \alpha R(K_{DP}) + (1 - \alpha)R(Z_H) \tag{5.18}$$

Here α is the blending factor and it is a function of the radar range. A higher value of alpha will give more weightage on the K_{DP} estimates and less weightage on the reflectivity based estimates. Within the X-band radar domain, the alpha is varied exponentially using the equation 5.19.

$$\alpha(r) = \frac{10^{pr} - 10^{pr_{ML}}}{1 - 10^{pr_{ML}}} \tag{5.19}$$

where p is the parameter that controls the shape of the α, r is the radar range, and r_{ML} is the range corresponding to the melting level height. An example of a variation of the α with the radar range when melting level height is at 1 km AGL is shown in Figure 5.16. Here the parameter p is set at 5. This yields higher values of alpha at near ranges. Alpha decreases exponentially near the melting level. This means more weight is given to the K_{DP} based estimates at ranges near the radar. The value of alpha is set to 0 at the range corresponding to the melting layer height. Beyond that range, the estimates should be only $R(Z_H)$.

Next, an example of the blended QPE is generated with observations from a precipitation event on Jan 27 2021 when the freezing level was around 1 km from MSL. This is compared to the

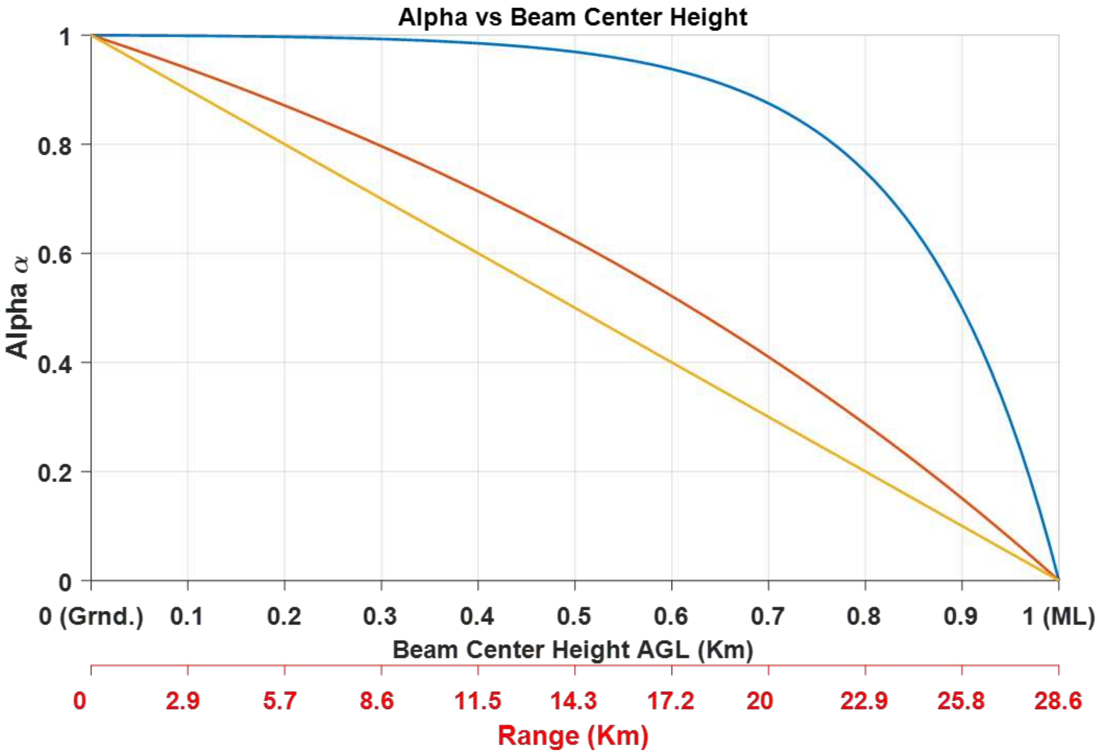

Figure 5.16: An example showing blending parameter α as a function of radar range considering the melting layer height at 1 km. The yellow line denotes an linear variation. The orange line denotes an exponential variation. The blue line is based on the equation 5.18 with p = 5

MRMS Radaronly product and rainfall estimation based on R(KDP) alone with VPR correction. This is presented in Figure 5.17.

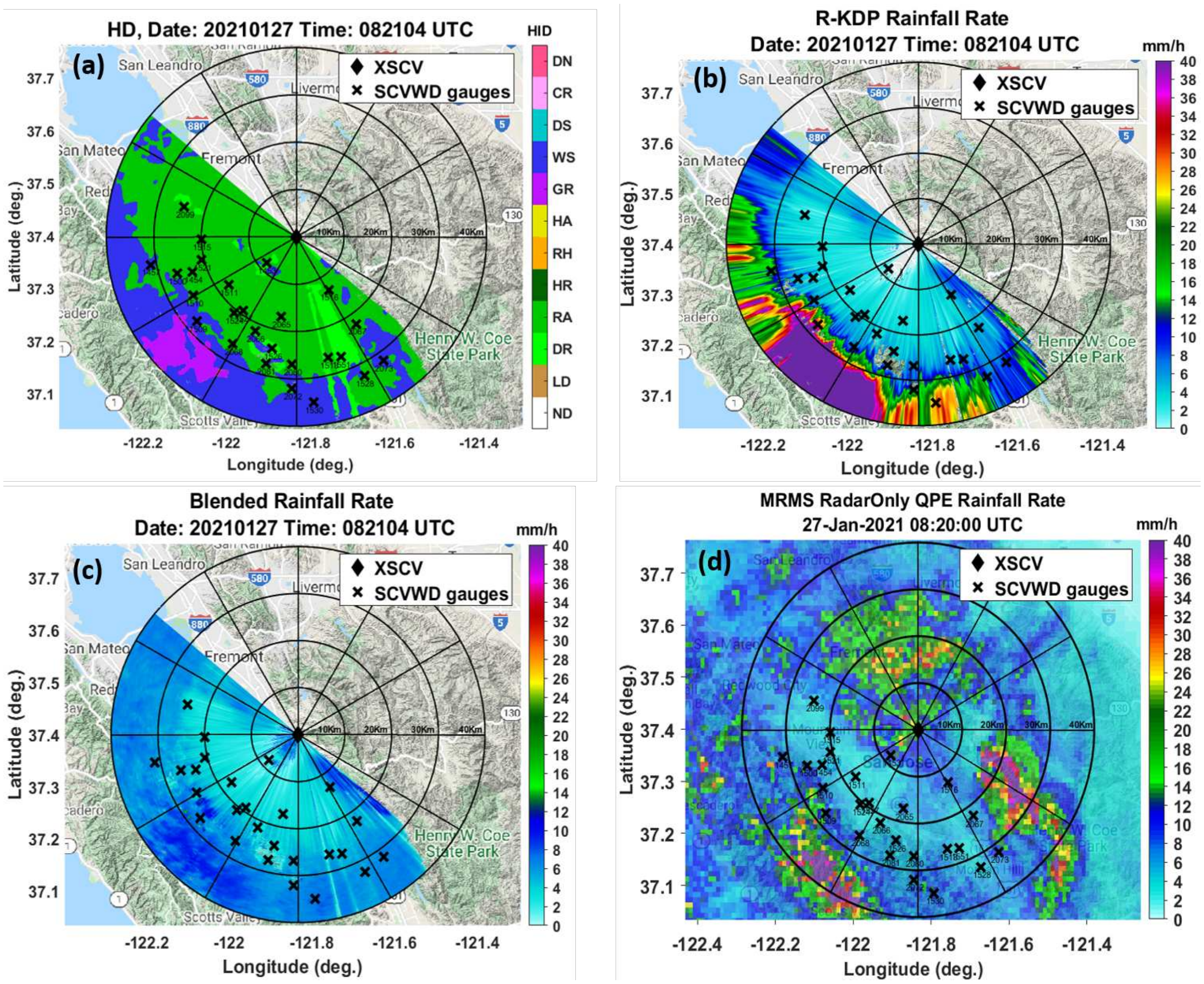

Figure 5.17: An example of the blended QPE map computed using the XSCV radar 2^o observations of the precipitation event of Jan 27 2021 at around 08:20 UTC and comparison to different rainfall estimates highlighting the effect of BB contamination. (a) Hydrometeor classification results (b) Rainfall map without VPR correction, (c) Rainfall map calculated using a blend of RK_{DP} and R_{Z_H} using VPR correction. (d) MRMS RadarOnly QPE product cropped within the XSCV domain.

5.6 Evaluation

The performance of the hybrid rainfall relations, developed in the preceding section, has been tested using observations from the XSCW X-Band radar. This radar, situated in Santa Rosa, conducts PPI scans starting at an elevation of 1.5^o and terminating at 4.5^o with 1-degree intervals. Throughout the year 2021, it observed numerous orographic precipitation events. For comparison and evaluation, three significant events have been selected, encompassing a range of low to moderate to heavy rainfall accumulations. The first event transpired from January 27 to 28, 2021, resulting in moderate rainfall amounts. During this event, the environmental freezing level was close to the ground, at approximately 1 km above ground level. The other two events took place on October 20, 2021, and October 24, 2021. Both of these events exhibited notable orographic enhancements, as observed by the S-PROF radar. The October 24, 2021 event was the most prolific rainfall producer of the year in this region, while the October 20, 2021 event featured lower rainfall rates in comparison to the other two events. To assess the accuracy of radar-based rainfall estimates, a comparative analysis is performed using simultaneous measurements from 26 rain gauges maintained by the Sonoma County Water Agency (SCWA).

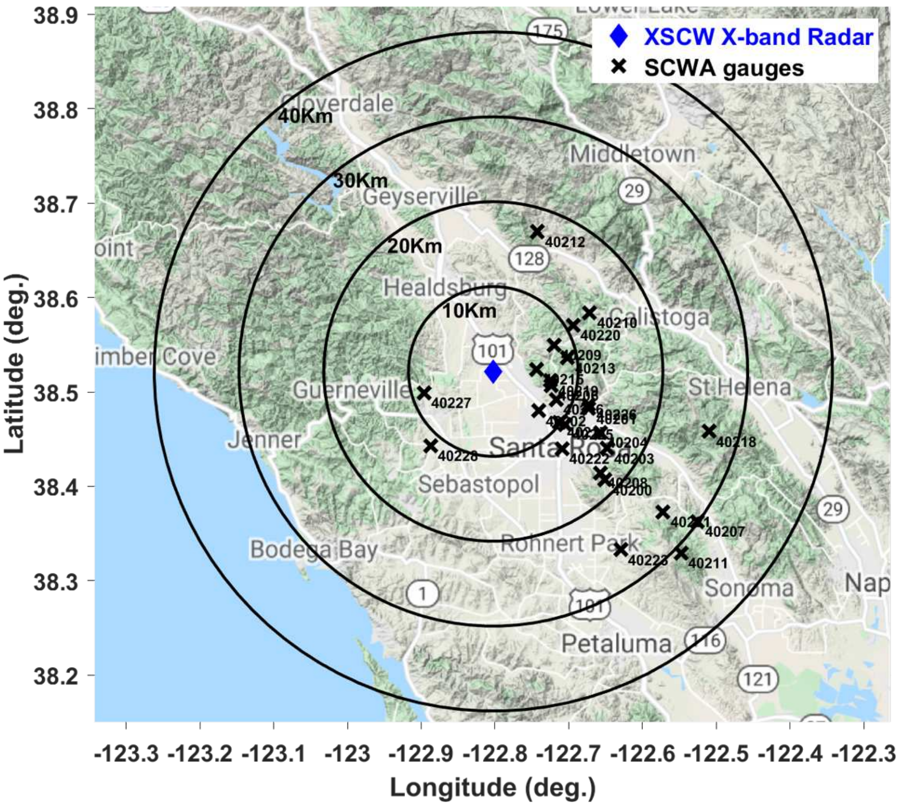

Figure 5.18: Location of rain gauges within the 40 km range domain of the XSCW radar used for validation purposes in this study. These rain gauges are maintained by the Sonoma County Water Agency

Table 5.1: Sonoma County Water Agency Rain Gauge Location

Gauge ID	Lat. (deg.)	Long. (deg.)	Location
'40200'	38.406656	-122.651431	Matanzas Reservoir
'40201'	38.482242	-122.672988	Brush Creek
'40202'	38.479830	-122.740988	Piner Creek
'40203'	38.440170	-122.648364	Spring Creek
'40204'	38.457047	-122.657442	Spring Lake
'40206'	38.506803	-122.723863	Linda Creek
'40207'	38.362584	-122.525253	Sonoma Creek
'40208'	38.413978	-122.657462	Matanzas Creek
'40209'	38.549400	-122.720072	Mark West Creek
'40210'	38.583716	-122.671742	Franz Creek
'40211'	38.329098	-122.547601	McCrea Trail Parcel
'40212'	38.669962	-122.742251	Buckeye Creek Ranch
'40213'	38.535928	-122.701547	Mark West Regional Park
'40215'	38.523822	-122.743892	Shiloh Ranch Regional Park
'40216'	38.492002	-122.717053	Skyfarm Water Tank
'40217'	38.467749	-122.712766	Paulin Creek
'40218'	38.458215	-122.510119	Bald Mountain
'40219'	38.511754	-122.724335	Mark West Creek
'40220'	38.570609	-122.694050	Pepperwood Preserve
'40221'	38.372593	-122.572176	Enterprise Road
'40222'	38.439661	-122.708967	Santa Rosa Downtown Culverts
'40223'	38.332678	-122.629408	Copeland Creek
'40225'	38.465531	-122.704673	Piner Creek Dam
'40226'	38.486643	-122.672493	Brush Creek Middle Fork Dam
'40227'	38.499188	-122.896077	Mirabel
'40228'	38.442742	-122.887214	Green Valley

Figure 5.18 shows the location of the gauges within the radar 40 km range domain. Table 5.1 shows the different SCWA gauge IDs along with their location and geographic coordinates.

The methodology for classifying rainfall into BB (Bright Band) and NBB (Non-Bright Band) categories uses radar observations of reflectivity Z and Z_{DR} at each radar range gate. A crucial aspect of this methodology is ensuring that Z and Z_{DR} are well-calibrated and free of systematic bias. The bias estimation for Z was conducted by comparing Z values calculated from data collected by a disdrometer at the STR (Santa Rosa) site with the actual observed Z values from the radar. This comparison revealed a mean Z bias of -5 dBZ, indicating that the radar measurements were lower by 5 dBZ. Consequently, a +5 dBZ adjustment was applied to rectify this bias. For the estimation of Z_{DR} bias, two distinct approaches were followed. The first method involved comparing Z_{DR} with the disdrometer data, much like the Z bias estimation process. The other one uses observation of drizzle data as discussed in chapter 4 section 4.3. Both approaches determined that the mean Z_{DR} bias was 2.5 dB based on the two methodologies used. The next step involved applying the classification methodology to radar scanning data obtained at the 2.5^o elevation angle. This specific elevation was chosen as it is the lowest angle at which there is no beam blockage at the gauge locations. For the January 27-28, 2021 event, during which the freezing level was very close to the ground, the radar beam at the 2.5^o elevation angle intersected the melting layer bottom at ranges of 16 km and beyond from the radar site. To account for this, a vertical profile correction algorithm was employed to project the radar reflectivity, contaminated by the Bright Band (BB), to the ground level. The methodology involved using hybrid rainfall estimators, with $R(K_{DP})$ estimators for ranges closer to the radar and $R(Z)$ estimators for ranges beyond 16 km where the radar beam was affected by BB. For the events on October 20 and 24, 2021, when the freezing level was higher, at about 2.5 km and 3.5 km from the mean sea level, respectively, only $R(K_{DP})$ estimators were utilized. Rainfall accumulations were computed based on 60-minute or hourly rainfall estimates. The performance of the classification methodology and the accuracy of radar-based rainfall estimates were evaluated by comparing these estimates with measurements from rain gauges maintained by the Sonoma County Water Agency (SCWA). While all rain gauges within the radar domain were used in the evaluation, Figure 5.19 displays comparisons between X-band radar rainfall estimates, SCWA rain gauge measurements, and operational Multi-Radar Multi-Sensor (MRMS) products at selected SCWA gauge locations. This assessment aims to validate the proposed methodology for different rainfall scenarios.

Figure 5.19 reveals a notable agreement between X-Band radar-derived rainfall accumulation and gauge-based estimates in the context of total precipitation accumulation. In contrast,

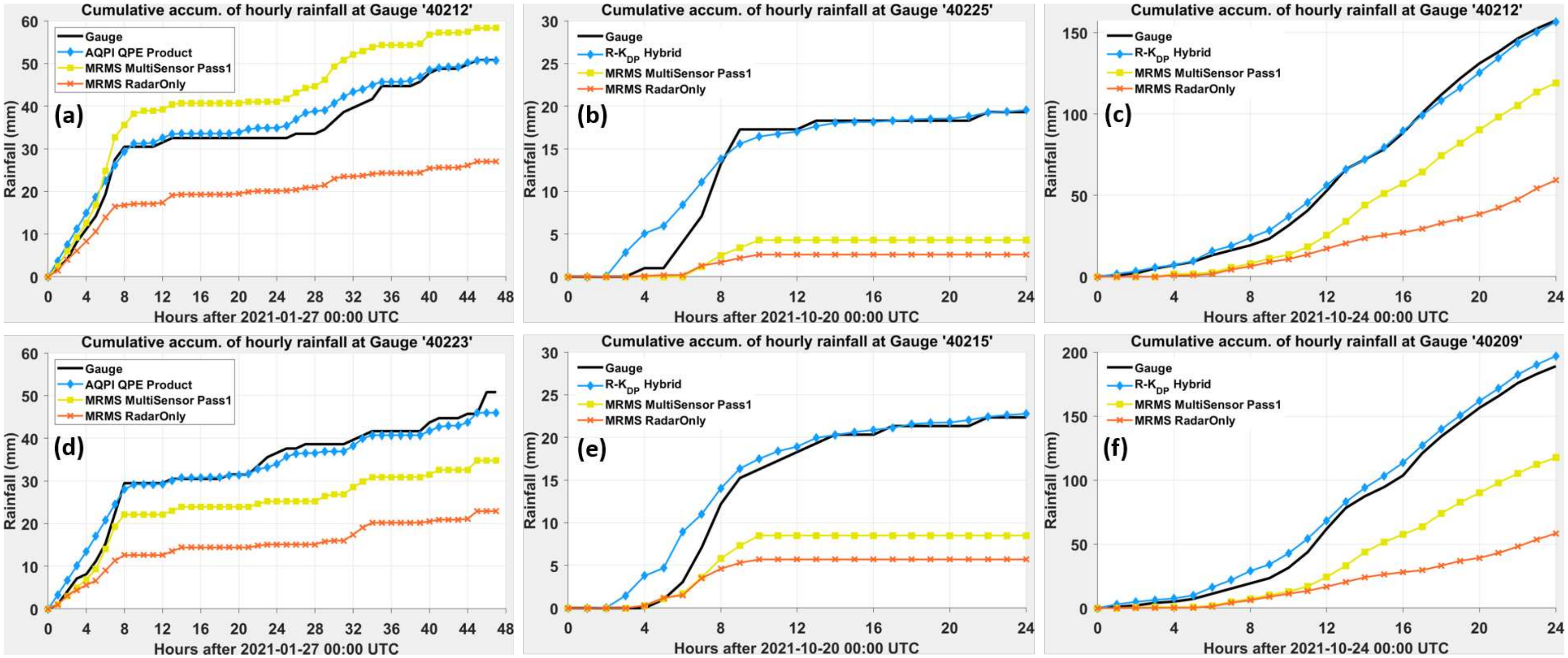

Figure 5.19: Comparison between cumulative accumulation of hourly rainfall for whole event at SCWA (a,d) gauge ID 40212 and 40223 for the January 27-28 2021 event, (b,e) gauge ID 40225 and 40215 for the October 20 2021 event, and (c,f) gauge ID 40212 and 40209 for the October 24 2021 event. The blue line indicates the AQPI XSCW radar product using the hybrid rainfall estimation algorithm, the yellow line indicates the MRMS Multisensor Pass 1 product and the orange line indicates the MRMS RadarOnly Product.

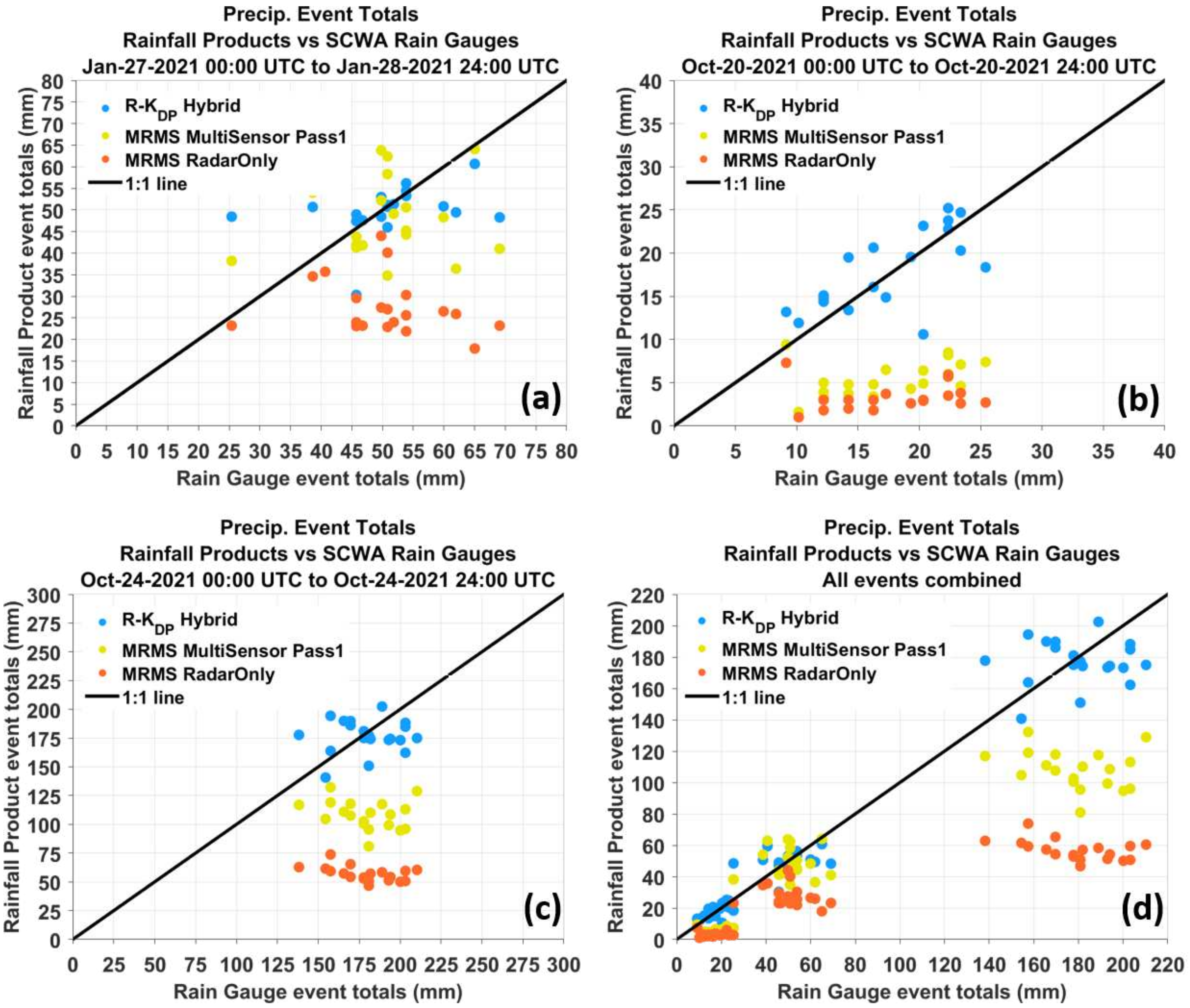

Figure 5.20: Scatter plot of event total rainfall accumulations from XSCW radar using hybrid $R(K_{DP})$, MRMS MultiSensor Pass1, and MRMS RadarOnly with all SCWA rain gauges. The black line denotes the 1:1 line. (a) January 27-28 2021 event. (b) October 20 2021 event. (c) October 24 2021 event. (d) All events combined.

the MRMS RadarOnly product, which relies on observations from the S-Band WSR-88D radar, consistently exhibits substantial underestimation of precipitation compared to the rain gauge measurements. The performance of the MultiSensor Pass 1 product displays some variability across different gauge locations. It is essential to acknowledge that, during the January 27-28, 2021 event, the MultiSensor Pass 1 product outperformed the X-Band radar estimates at a few gauge locations. This superior performance can be attributed to the relatively lower orographic enhancement observed in the January event compared to the other two events. In this context, the product demonstrates commendable accuracy at gauge locations closely located with those utilized in the intrinsic gauge correction mechanism of the MultiSensor Pass 1 Product. To gain a comprehensive perspective on the overall performance of QPE, event total accumulations were systematically compared and represented through a scatter plot, as depicted in Figure 5.20. In Table 5.2, key statistical metrics, including Mean Bias, Mean Absolute Error, and Root Mean Squared Error, provide a quantitative evaluation of the performance of different QPE products. Assuming the rain gauge measurements as the ground truth, each score can be defined as follows

$$MB = \frac{1}{N}\sum_{n=1}^{N}(R_n - G_n) \tag{5.20}$$

$$MAE = \frac{1}{N}\left|\sum_{n=1}^{N}(R_n - G_n)\right| \tag{5.21}$$

$$RMSE = \sqrt{\frac{1}{N}\sum_{n=1}^{N}(R_n - G_n)^2} \tag{5.22}$$

where G_n and R_n denote the rain gauge and radar rainfall measurement at each rain gauge location respectively. N is the total number of rain gauges.

A negative mean bias indicates overall underestimation. Overall, the hybrid $R(K_{DP}$ shows a small negative mean bias (not exceeding 3.6 mm) compared to the MRMS products, indicating little underestimation. The mean absolute error gives an idea of the magnitude of underestimation or overestimation. When all three events are considered together the overall mean absolute error is less than 9 mm and the root mean squared error is less than 13 mm which is good when compared to the MRMS products. Of the three products, the MRMS RadarOnly has the worst performance in terms of all three scores. Overall, the performance of the QPE using the X-Band hybrid $R(K_{DP})$ estimator is the best compared to the MRMS products.

Table 5.2: Statistical Metrics

		Mean Bias (mm)	Mean Absolute Error (mm)	Root Mean Square Error (mm)
Jan 27-28 2021	R-KDP Hybrid	-0.17	6.78	10.00
	MRMS MultiSensor Pass1	-1.78	10.37	13.00
	MRMS RadarOnly	-22.78	22.00	26.20
Oct 20 2021	R-KDP Hybrid	0.48	2.92	3.75
	MRMS MultiSensor Pass1	-12.08	12.11	12.8
	MRMS RadarOnly	-14.32	14.32	15.13
Oct 24 2021	R-KDP Hybrid	-3.6	19.6	22.99
	MRMS MultiSensor Pass1	-71.89	71.89	75.93
	MRMS RadarOnly	-123.42	123.42	125.4
All events	R-KDP Hybrid	-1.15	8.91	12.76
	MRMS MultiSensor Pass1	-28.86	31.79	45.44
	MRMS RadarOnly	-54.24	54.24	75.10

Chapter 6

Development of AQPI QPE products

6.1 Introduction on MRMS

The Multi-Radar Multi-Sensor (MRMS) system, developed at the National Centers for Environmental Prediction (NCEP), showcases remarkable capabilities. Currently, MRMS seamlessly combines data from approximately 180 operational radars to create a unified 3D radar mosaic over the contiguous United States (CONUS) and southern Canada. This mosaic has a spatial resolution of 1 km. The temporal resolution is 1 hour for most of the products and 2 minutes for the RadarOnly product. MRMS synergizes radar base data with atmospheric environmental data, satellite information, and data from lightning and rain gauges to generate a comprehensive suite of products related to severe weather and quantitative precipitation estimation (QPE). The integration of multiple radars overcomes limitations inherent in the single-radar framework, such as issues related to radar coverage gaps. Furthermore, the combination of radar data with multisensor inputs facilitates more accurate insights into atmospheric physical processes when compared to using radar data in isolation. For instance, having access to the 3D temperature and moisture fields proves invaluable for tasks like hydrometeor classification and distinguishing between continental and tropical rain.

MRMS originated from the collaborative efforts of the National Severe Storms Laboratory (NSSL) and draws from components found in the Warning Decision Support System–Integrated Information (WDSS-II) developed by Lakshmanan et al. (2007) [89] and the National Mosaic and Multi-Sensor QPE (NMQ) system described by Zhang et al. (2011) [13]. The MRMS domain covers the CONUS area, bounded by latitudes ranging from 20° to 55° N and longitudes from 130° to 60° W. The MRMS grid features a horizontal resolution of 0.01° in both latitude and longitude, equivalent to approximately 1.11 kilometers in the north–south direction across the domain. In the west–east direction, the grid resolution varies, with about 1 kilometer at the southern boundary and approximately 0.6 kilometers at the northern boundary. Regarding radar data, MRMS assimilates 3D volume scans from approximately 146 S-band dual-polarization Weather Surveillance Radar-1988 Doppler (WSR-88D) radars and roughly 30 C-band single-polarization weather radars operated by Environment Canada. The volume scan duration within these networks spans from 3 to 10 minutes.

6.2 MRMS Products

MRMS offers three primary Quantitative Precipitation Estimation (QPE) products, specifically:

RadarOnly QPE: This product aggregates Surface Precipitation Rate (SPR) data over defined time intervals to compute precipitation accumulations. The QPE – Radar Only component boasts superior spatial and temporal coverage for precipitation estimation. It provides updated one-hour accumulations every 2 minutes, making it particularly valuable for flash flood warning decisions. Longer accumulations serve well for riverine flood warnings and as approximations for "storm total" metrics. It's important to note that this product primarily generates accumulations at the top of each hour, preventing the calculation of running or storm totals, which is a limitation for flash flood forecasting. Radar-based precipitation accumulations, while valuable, are not true surface measurements, as they are subject to radar coverage, which typically samples above the surface. This can result in certain precipitation not reaching the ground due to factors like evaporation or wind shear. At extended distances from radar sites, beam broadening may cause the volume being sampled to smooth out precipitation features, leading to a loss of fine-scale details necessary for accurate accumulation estimates. These instances of potentially false light precipitation justify the 0.01 inch precipitation removal threshold. Moreover, the QPE – Radar Only field can exhibit biases tied to SPR data. This encompasses issues related to beam blockage and the Z-R relationships and their capacity to fully represent drop size distributions (DSDs). It's worth mentioning that the QPE – Radar with Gauge Bias Correction product demonstrates greater accuracy over non-mountainous terrain.

Multi-Sensor QPE: This product supplements radar data by combining gauge measurements with Numerical Weather Prediction (NWP) Quantitative Precipitation Forecast (QPF) data, particularly from the High-Resolution Rapid Refresh (HRRR) and Rapid Refresh (RAP) models for the CONUS. Multi-Sensor QPE is available in two variants: Pass 1 and Pass 2. Pass 1 is released earlier but includes fewer gauge inputs, whereas Pass 2 has higher latency but incorporates most gauge data. This QPE product relies on a decision tree that dictates which input product should be assigned to each grid cell. Radar QPE with Gauge Bias Correction is the preferred input, and in areas with poor radar coverage, Mountain Mapper QPE and NWP model QPF serve as supplemental inputs. The Multi-Sensor QPE leverages a range of data sources (radar, gauges, and model QPF) to ensure comprehensive QPE coverage across the CONUS. Radar QPE with Gauge Bias Correction optimizes the spatial coverage of radar data by adjusting it with direct rainfall observations, outperforming the Radar-Only product. Mountain Mapper, an integral component, mitigates beam blockage artifacts and considers flow regimes. Importantly, it operates independently of radar coverage. To fill the remaining radar gaps, particularly in snow and convective rain environments and stratiform rain in non-complex terrain, NWP model QPF data is utilized. The Multi-Sensor QPE does face latency issues, with Pass 1 having a 60-minute delay and Pass 2 having a 120-minute delay. Notably, errors can still arise due to limitations in rain gauge measurements, radar-estimated QPE (including Z-R relationships), and Gauge Quality Control (QC) algorithms. When the real-time precipitation gradient significantly deviates from PRISM climatology, substantial errors may occur in Mountain Mapper. Sparse gauge networks can lead to extensive interpolation, potentially introducing errors. It's also important to acknowledge that HRRR has inherent biases and limitations in terms of precipitation placement and generation.

The Multi-Radar Multi-Sensor (MRMS) system plays a pivotal role in enhancing the accuracy of precipitation estimation, catering to various weather-related decision-making processes, ranging from flash flood warnings to riverine flood predictions.

6.3 AQPI QPE products over the entire domain

AQPI includes several products from both the observations and models. Some products are simply model forecasts of precipitation, streamflow, and coastal water levels from the modeling systems described above, customized for the water agency's region of interest. Other products are derived from observations. This includes QPE and Nowcast. The QPE product includes a blend of AQPI radar data where the X-bands provide coverage and MRMS data to cover the rest of the domain. The system architecture of the radar data flow during various steps of data processing is shown below in Figure 6.1.

The raw X-band radar data is streamed from the radar sites in the Bay Area to the local storage distribution server known as the sfbay server by LDM (Local Data Manager) protocol. From the sfbay server, the data is moved to the local computation server where radar data quality control and QPE processing are done. Once individual X-Band QPE data are generated, it is mapped into the AQPI grid and consequently merged with the MRMS RadarOnly QPE data to generate the final AQPI QPE product. The spatial resolution of this product is 250m by 250m and the temporal resolution is every 2 minutes. The final QPE products are stored at local storage servers and also displayed via the website which can be accessed by end users. The AQPI radar QPE builds on the specific differential phase approach described in [20]. The current version of the QPE is based on the application of optimum radar rainfall estimators (both reflectivity and specific differential phase based) which is guided by an orographic/stratiform rainfall type classification as discussed in chapter 5.3. It also includes an algorithm to mitigate bright band contamination. The MRMS radar-only QPE is used to fill the QPE in the remainder of the AQPI domain outside the coverage of the AQPI radars as well as areas within the AQPI radar coverage domain that are blocked by terrain or other features. Both 15-minute and hourly QPE are provided with an update time of two minutes. An example of the QPE product is shown in Figure 6.3.

It should be noted that some "spike" like appearances are still present in the final QPE product, especially in the northern part of the XSCW domain. This pattern indicates blockage of the AQPI radar signal resulting from objects near the radar site. This region is completely blocked for all the

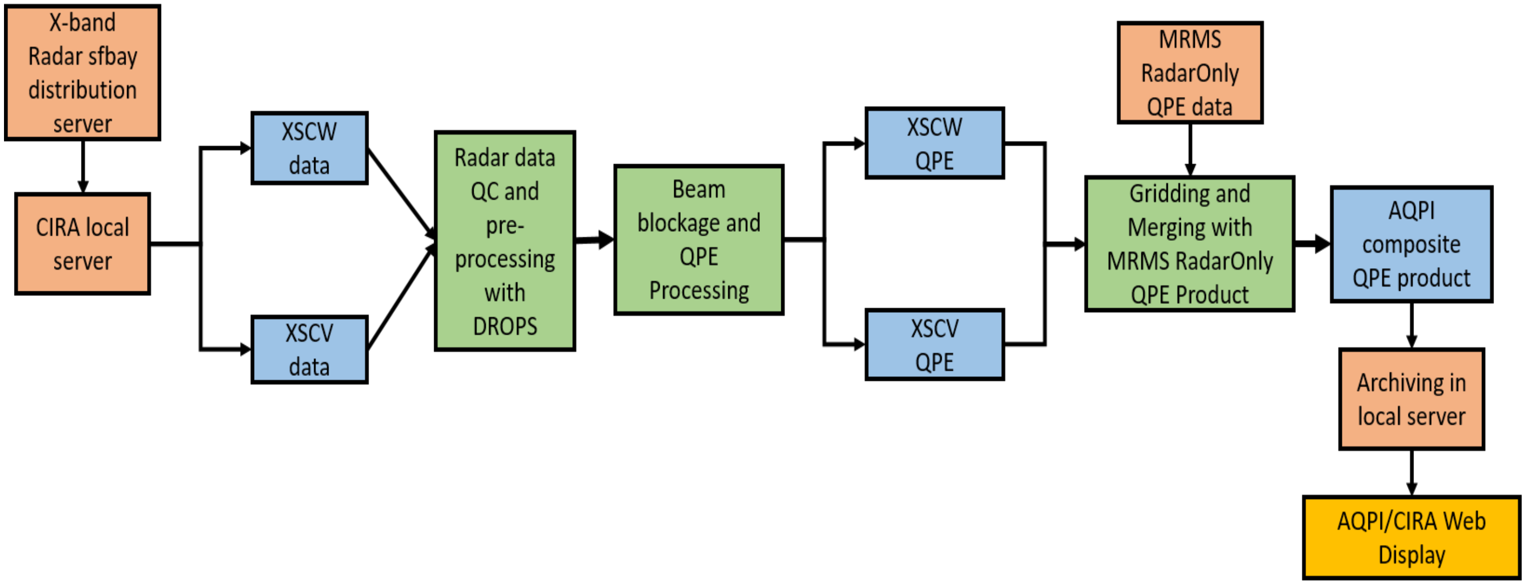

https://www.chivo.engr.colostate.edu/aqpi

Figure 6.1: AQPI QPE system real-time data flow architecture.

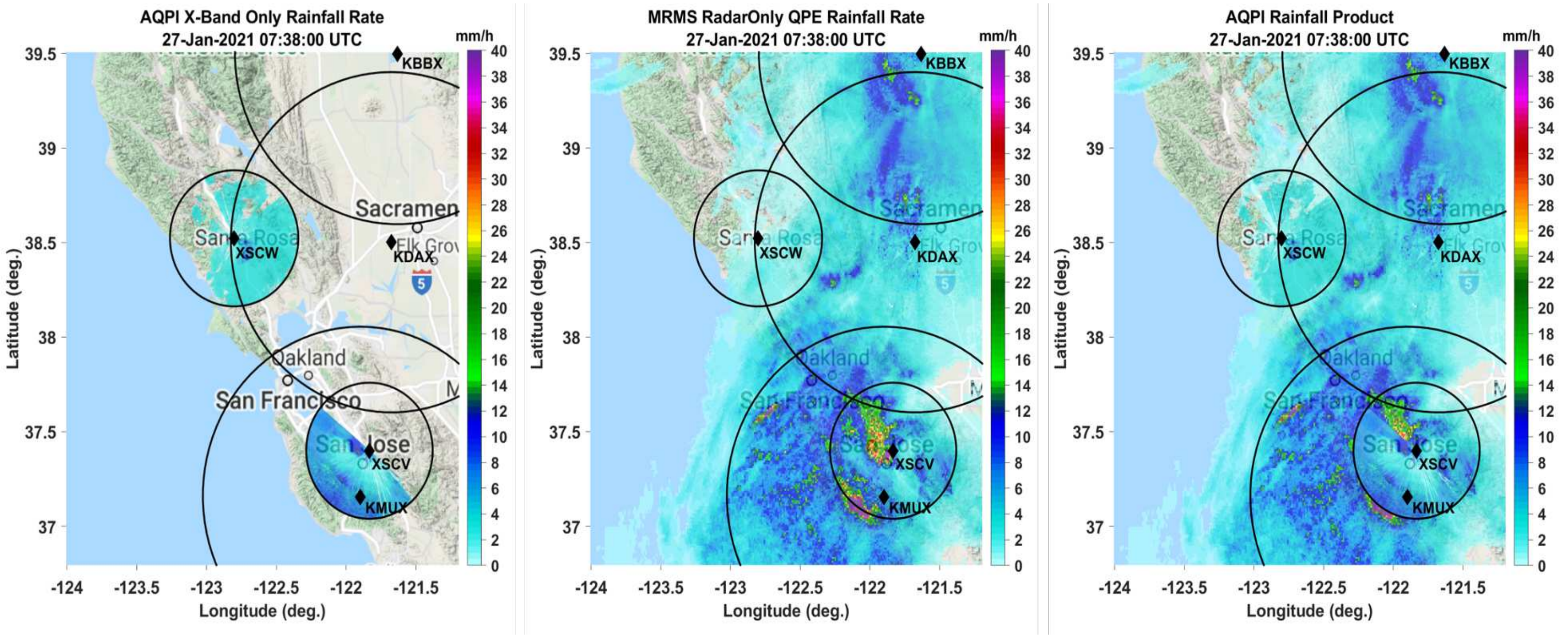

Figure 6.2: (a)AQPI X-Band Radar only QPE. (b) The MRMS RadarOnly Product QPE (c) Combined AQPI X-Band and MRMS RadarOnly Product QPE.

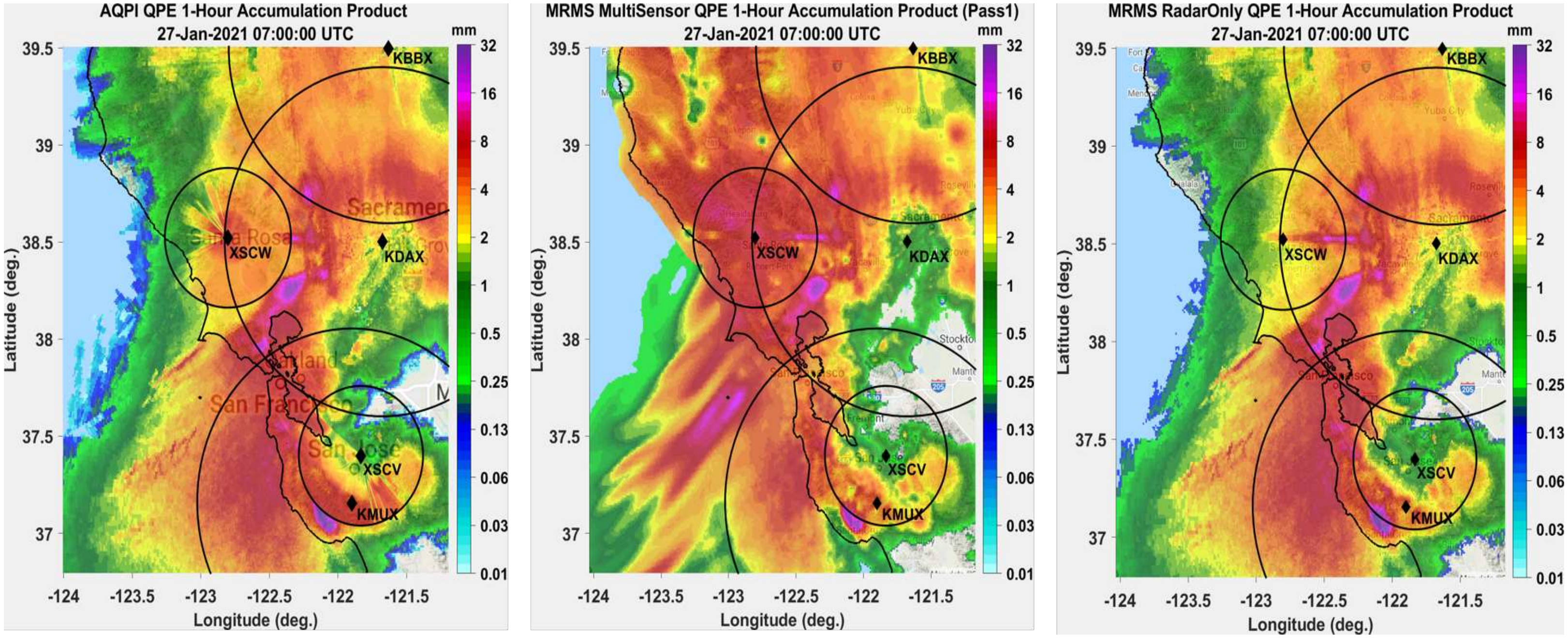

Figure 6.3: Examples of different QPE products over the AQPI domain for the January 27 2021 precipitation event. Images show Hourly QPE ending at 07:00 UTC. (a) AQPI product (b) MRMS RadarOnly QPE (c) MUltiSensor Pass 1. The QPE map is constructed using a combination of AQPI radar QPE within the small circles and MRMS radar-only QPE over the rest of the domain. Small circles show the 40-km range rings of AQPI X-band radars located near XSCW and XSCV and the larger circles represent the 100-km range ring of the NEXRAD KMUX, KDAX, and KBBX radar systems. Note that the streaks in the XSCW circle represent terrain blockage.

XSCW PPI scan angles. MRMS data is currently used to fill gaps, which is less than ideal given the challenges with NEXRAD coverage in this area. There are long-term plans to raise the XSCW radar to help reduce the blockage or move it to an alternate location.

Chapter 7

Discussions and Future Work

This study underscores the significance of high-resolution radar measurements within the San Francisco Bay Area. The utilization of state-of-the-art X-band radar systems for gap-filling purposes serves as a pivotal resource for enhancing situational awareness. Furthermore, it offers the advantage of delivering high-quality Quantitative Precipitation Estimation (QPE), which, in turn, aids meteorologists in identifying urban flash flood threats and assists water managers in addressing potential water quality concerns arising from precipitation events. The study presented in this work demonstrates the benefits of advanced precipitation monitoring in the complex terrain region of the US West, including the Bay Area. In this regard, the establishment of a network of X-band radars stands poised to augment the existing NEXRAD coverage. By providing high-resolution QPE and short-term forecasts, such a network has the potential to yield an array of advantages spanning multiple economic sectors. These benefits include flood damage mitigation, preservation of water quality, and the optimization of transportation systems.

7.1 AQPI Benefits

AQPI has been meticulously designed to offer valuable support for a myriad of water management endeavors within the Bay Area. While it may not provide extensive long-term forecasts suitable for the management of large reservoirs, its utility shines when it comes to assisting smaller reservoir managers. These stakeholders can effectively time discharges before and during periods of heavy rainfall, thereby ensuring the preservation of water supplies and the prevention of downstream flood damage exacerbation. Wastewater treatment plant operators situated around the Bay would gain the ability to take proactive measures in response to substantial storm surges during such events.

Another notable advantage of the AQPI system lies in its capacity to empower flood protection agency managers with improved foresight into potential flooding incidents. This enhancement enables them to deploy their resources more strategically and efficiently in preparation for such events. Johnson et al. (2020) conducted a comprehensive analysis of the potential advantages presented by the AQPI system. Their assessment encompassed diverse economic sectors, including flood damage mitigation, augmented water supplies, and the enrichment of ecological, recreational, and transportation services. Of particular significance is the finding that a substantial 48% of the overall benefits are attributed to the prevention of flood damages. The estimated benefits-to-costs ratio spans from 2:1 to 10:1, with the most probable ratio standing at 5:1. This variation underscores the inherent uncertainty linked to the percentage of water management agencies and citizens who take appropriate measures. It emphasizes the pivotal role of outreach and training efforts in maximizing the desired responses.

7.2 Discussions

Precipitation in the San Francisco Bay Area is profoundly influenced by orographic effects, particularly with the presence of mountains. Existing research, as demonstrated by studies such as [9, 10], has recorded instances of orographic rain even in flat valley regions where orographic rainfall might not be expected. The current research focuses on two NOAA Hydrometeorology Testbed (HMT) sites: MDT, situated in mountainous terrain, and STR, located in a valley region. The investigation delves into the characteristics of Drop Size Distributions (DSD) at these sites, evaluated based on collocated disdrometer and S-PROF observations. This comprehensive exploration encompasses diverse rainfall processes, including scenarios with bright-band rain featuring robust ice processes, subsequent melting, and non bright band rain, which is predominantly marked by warm rain collision coalescence below the melting level. Remarkably, orographic rain, herein referred to as NBB (Non-Bright Band) rain, exhibits distinctive characteristics when compared to BB (Bright Band) rain. It is typified by a higher concentration of smaller raindrops, typically less than 1 mm in diameter. Notably, NBB rain is associated with lower values of radar parameters, including radar reflectivity (Z) and specific differential phase (K_{DP}), in contrast to BB rain. Strikingly, an observation is made that, when radar parameters (Z and K_{DP}) are held constant, NBB rainfall yields a higher rainfall rate compared to BB rain. This disparity underscores the necessity of an improved radar-based Quantitative Precipitation Estimation (QPE) approach, particularly in complex terrains. To address this, a $Z - Z_{DR}$ threshold is introduced in this study, which serves to distinguish NBB rain from BB rain. Importantly, it can be applied to real-time radar scan data. However, it's worth noting that there is a degree of sample overlap in the $Z - Z_{DR}$ space between BB and NBB rain. This overlap could be attributed to parameterization errors, which may be addressed through more advanced techniques like machine learning-based classification. Another plausible explanation for this overlap is the presence of an intermediate rainfall type known as hybrid rain, detailed in White (2003). Hybrid rainfall exhibits characteristics that bridge the gap between BB and NBB rain types. Although not explored separately in this work, investigating the hybrid rainfall type and incorporating it into algorithm development may further enhance radar-based QPE in complex terrains. Radar rainfall estimators, including $R(K_{DP})$ and $R(Z)$, are calculated independently for BB and NBB rain types. Significantly, the coefficients for NBB rainfall estimators differ substantially from those associated with BB rainfall estimators. An average $R(K_{DP})$ relation, which amalgamates BB and NBB rain data, is also established. Notably, using an average relation results in overestimation during BB periods and significant underestimation during NBB periods. This discrepancy underscores the paramount significance of the proposed radar-based QPE algorithm introduced in this study. It's a well-established fact that K_{DP} offers substantial advantages in radar-based rainfall estimation, particularly at X-band frequencies. Additionally, the parameterization error associated with $R(K_{DP})$ is lower compared to reflectivity-based estimators. However, it's important to note that $R(K_{DP})$ may not be suitable in cases of bright band contamination. As a countermeasure, $R(Z)$ estimators are also derived for both BB and NBB rainfall types, with a recommendation to employ VPR correction in regions impacted by bright band contamination. It's important to exercise caution when applying polarimetric algorithms to radar data in real-time, particularly concerning the Z_{DR} parameter, as it plays a crucial role in NBB rainfall classification and estimation. Any bias in Z_{DR} can lead to inaccuracies in QPE estimation using the algorithm outlined in this study. Therefore, frequent calibration and correction of Z_{DR} is essential. In conclusion, this research suggests the potential for a more precise X-band radar-based QPE approach that effectively accounts for variations in rainfall type within the San Francisco Bay Area region.

7.3 Future Work

In this work, a methodology for detecting orographic rainfall based on dual-pol radar measurements at X-Band has been developed followed by calculation dual-pol based rainfall estimators. An algorithm has been proposed that can distinguish orographic rainfall from stratiform rainfall and accordingly apply rainfall type-specific estimators. It is robust and can be applied to scanning X-Band radar data in real-time. Application of the algorithm to a few historical precipitation events demonstrated superior performance compared to existing operational QPE products. The results are promising. However, some scientific and technical aspects need to be addressed so that the methodology can be applied operationally for creating QPE products. The overall goal is to develop accurate QPE products over the entire AQPI domain. Future works are summarized as follows:

Due to the spatial and temporal variability of DSD, a mean Vertical Profile of the Reflectivity (VPR) is not sufficient to represent rainfall microphysics correctly. The VPR correction scheme proposed in this study can be improved using a more sophisticated approach using real-time observations from the vertically pointing radars. AQPI would benefit from a more dense deployment of profiler radars. By the time this research was completed, there was another deployment of an X-Band radar named XSCR at Santa Cruz. This radar is located close to the XSCV radar. There is an overlap of the southern domain of the XSCV with that of the XSCR northern domain. A methodology should be developed that will merge the precipitation estimates from the individual radars in the common observation area. There is a considerable amount of beam blockages in both of the X-band radar domains due to terrain. The current study demonstrated a methodology that utilizes higher elevation scan data at the blocked region to create a composite map. However, this method has its limitations when all the elevation scans are blocked. At present, the complete blocked regions are filled up by azimuthal interpolation of nearby rays. However, when the observation gap is large, this method will give unrealistic estimates of radar measurements. In such a scenario, a more sophisticated machine learning approach is desirable which can fill the observation discontinuities using deep learning techniques employing convolutional neural networks. QPE product is needed over the regions in the AQPI domain which is not covered by the X-Band. At present, there are operational QPE products available in the domain that are not quite accurate. An independent QPE product needs to be developed based on the operational S-Band NEXRAD observations which will fill the gaps in the domain. Using this, a final blended QPE product can be developed that will cover the entire AQPI domain based on both individual X-Band and S-Band products.

Bibliography

[1] R. Cifelli, V. Chandrasekar, L. Herdman, D. D. Turner, A. B. White, T. I. Alcott, M. Anderson, P. Barnard, S. K. Biswas, M. Boucher, J. Bytheway, H. Chen, H. Cutler, J. M. English, L. Erikson, F. Junyent, D. J. Gottas, J. Jasperse, L. E. Johnson, J. Krebs, J. van de Lindt, J. Kim, M. Leon, Y. Ma, M. Marquis, W. Moninger, G. Pratt, C. Radhakrishnan, M. Shields, J. Spaulding, B. Tehranirad, and R. Webb, "Advanced quantitative precipitation information: Improving monitoring and forecasts of precipitation, streamflow, and coastal flooding in the san francisco bay area," *Bulletin of the American Meteorological Society*, 2022.

[2] R. Cifelli and V. Chandrasekar, "Dual-polarization radar rainfall estimation," *Washington DC American Geophysical Union Geophysical Monograph Series*, vol. 191, pp. 105–125, 2010.

[3] H. Chen, V. Chandrasekar, and R. Bechini, "An improved dual-polarization radar rainfall algorithm (drops2. 0): Application in nasa ifloods field campaign," *Journal of Hydrometeorology*, vol. 18, no. 4, pp. 917–937, 2017.

[4] G. Skofronick-Jackson, W. A. Petersen, W. Berg, C. Kidd, E. F. Stocker, D. B. Kirschbaum, R. Kakar, S. A. Braun, G. J. Huffman, T. Iguchi, *et al.*, "The global precipitation measurement (gpm) mission for science and society," *Bulletin of the American Meteorological Society*, vol. 98, no. 8, pp. 1679–1695, 2017.

[5] S. K. Biswas and V. Chandrasekar, "Cross-validation of observations between the gpm dual-frequency precipitation radar and ground based dual-polarization radars," *Remote Sensing*, vol. 10, no. 11, p. 1773, 2018.

[6] S. Y. Matrosov, F. M. Ralph, P. J. Neiman, and A. B. White, "Quantitative assessment of operational weather radar rainfall estimates over california's northern sonoma county using hmt-west data," *Journal of Hydrometeorology*, vol. 15, no. 1, pp. 393 – 410, 2014.

[7] A. B. White, P. J. Neiman, F. M. Ralph, D. E. Kingsmill, and P. O. G. Persson, "Coastal orographic rainfall processes observed by radar during the california land-falling jets experiment," *Journal of Hydrometeorology*, vol. 4, no. 2, pp. 264–282, 2003.

[8] B. E. Martner, S. E. Yuter, A. B. White, S. Y. Matrosov, D. E. Kingsmill, and F. M. Ralph, "Raindrop size distributions and rain characteristics in california coastal rainfall for periods with and without a radar bright band," *Journal of Hydrometeorology*, vol. 9, no. 3, pp. 408 – 425, 2008.

[9] S. Y. Matrosov, R. Cifelli, P. J. Neiman, and A. B. White, "Radar rain-rate estimators and their variability due to rainfall type: An assessment based on hydrometeorology testbed data from the southeastern united states," *Journal of Applied Meteorology and Climatology*, vol. 55, no. 6, pp. 1345 – 1358, 2016.

[10] D. E. Kingsmill, P. J. Neiman, and A. B. White, "Microphysics regime impacts on the relationship between orographic rain and orographic forcing in the coastal mountains of northern california," *Journal of Hydrometeorology*, vol. 17, no. 11, pp. 2905–2922, 2016.

[11] J. Marshall, W. Hitschfeld, and K. Gunn, "Advances in weather radar," *Advances in Geophysics*, vol. 2, pp. 1–56, 1955.

[12] D. Rosenfeld, D. B. Wolff, and D. Atlas, "General probability-matched relations between radar reflectivity and rain rate," *Journal of Applied Meteorology and Climatology*, vol. 32, no. 1, pp. 50–72, 1993.

[13] J. Zhang, K. Howard, C. Langston, S. Vasiloff, B. Kaney, A. Arthur, S. Van Cooten, K. Kelleher, D. Kitzmiller, F. Ding, *et al.*, "National mosaic and multi-sensor qpe (nmq) system: Description, results, and future plans," *Bulletin of the American Meteorological Society*, vol. 92, no. 10, pp. 1321–1338, 2011.

[14] M. N. Anagnostou, J. Kalogiros, E. N. Anagnostou, M. Tarolli, A. Papadopoulos, and M. Borga, "Performance evaluation of high-resolution rainfall estimation by x-band dual-

polarization radar for flash flood applications in mountainous basins," *Journal of hydrology*, vol. 394, no. 1-2, pp. 4–16, 2010.

[15] V. Chandrasekar, R. M. Beauchamp, and R. Bechini, *Introduction to Dual Polarization Weather Radar: Fundamentals, Applications, and Networks*. Cambridge University Press, 2023.

[16] S. Lim, D.-R. Lee, R. Cifelli, and S. H. Hwang, "Quantitative precipitation estimation for an x-band dual-polarization radar in the complex mountainous terrain," *KSCE Journal of Civil Engineering*, vol. 18, no. 5, pp. 1548–1553, 2014.

[17] R. Cifelli, V. Chandrasekar, S. Lim, P. C. Kennedy, Y. Wang, and S. A. Rutledge, "A new dual-polarization radar rainfall algorithm: Application in colorado precipitation events," *Journal of Atmospheric and Oceanic Technology*, vol. 28, no. 3, pp. 352–364, 2011.

[18] J. Zhang, K. Howard, C. Langston, B. Kaney, Y. Qi, L. Tang, H. Grams, Y. Wang, S. Cocks, S. Martinaitis, *et al.*, "Multi-radar multi-sensor (mrms) quantitative precipitation estimation: Initial operating capabilities," *Bulletin of the American Meteorological Society*, vol. 97, no. 4, pp. 621–638, 2016.

[19] S. E. Yuter and R. A. Houze, "Measurements of raindrop size distributions over the pacific warm pool and implications for z–r relations," *Journal of Applied Meteorology and Climatology*, vol. 36, no. 7, pp. 847–867, 1997.

[20] R. Cifelli, V. Chandrasekar, H. Chen, and L. E. Johnson, "High resolution radar quantitative precipitation estimation in the san francisco bay area: Rainfall monitoring for the urban environment," *Journal of the Meteorological Society of Japan. Ser. II*, vol. 96, pp. 141–155, 2018.

[21] S. K. Biswas, R. Cifelli, and V. Chandrasekar, "Evaluation of quantitative precipitation estimation by s-band radar in complex terrain over the feather river basin in california, usa.," in *AGU Fall Meeting Abstracts*, vol. 2018, pp. A31H–2926, 2018.

[22] S. K. Biswas, V. Chandrasekar, R. Cifelli, and J. Bytheway, “Evaluation of the mountain mapper product generated by the multi-radar multi-sensor system (mrms) over the russian river basin region in california,” in *98th American Meteorological Society Annual Meeting*, AMS, 2018.

[23] H. Chen, R. Cifelli, V. Chandrasekar, and Y. Ma, “A flexible bayesian approach to bias correction of radar-derived precipitation estimates over complex terrain: Model design and initial verification,” *Journal of Hydrometeorology*, vol. 20, no. 12, pp. 2367–2382, 2019.

[24] S. K. Biswas, R. Cifelli, and V. Chandrasekar, “Improving quantitative precipitation estimation by x-band dual-polarization radars in complex terrain over the bay area in california, usa,” in *IGARSS 2020-2020 IEEE International Geoscience and Remote Sensing Symposium*, pp. 5411–5414, IEEE, 2020.

[25] J. L. Bytheway, M. Hughes, K. Mahoney, and R. Cifelli, “On the uncertainty of high-resolution hourly quantitative precipitation estimates in california,” *Journal of Hydrometeorology*, vol. 21, no. 5, pp. 865–879, 2020.

[26] L. E. Johnson, R. Cifelli, and A. White, “Benefits of an advanced quantitative precipitation information system,” *Journal of flood risk management*, vol. 13, p. e12573, 2020.

[27] P. Waterman, “Matrix formulation of electromagnetic scattering,” *Proceedings of the IEEE*, vol. 53, no. 8, pp. 805–812, 1965.

[28] F. M. Ralph, P. J. Neiman, D. E. Kingsmill, P. O. G. Persson, A. B. White, E. T. Strem, E. D. Andrews, and R. C. Antweiler, “The impact of a prominent rain shadow on flooding in california’s santa cruz mountains: A caljet case study and sensitivity to the enso cycle,” *Journal of Hydrometeorology*, vol. 4, no. 6, pp. 1243 – 1264, 2003.

[29] F. M. Ralph, P. J. Neiman, G. A. Wick, S. I. Gutman, M. D. Dettinger, D. R. Cayan, and A. B. White, “Flooding on california’s russian river: Role of atmospheric rivers,” *Geophysical Research Letters*, vol. 33, no. 13, 2006.

[30] P. J. Neiman, F. M. Ralph, G. A. Wick, J. D. Lundquist, and M. D. Dettinger, "Meteorological characteristics and overland precipitation impacts of atmospheric rivers affecting the west coast of north america based on eight years of ssm/i satellite observations," *Journal of Hydrometeorology*, vol. 9, no. 1, pp. 22 – 47, 2008.

[31] J. J. Gourley, D. P. Jorgensen, S. Y. Matrosov, and Z. L. Flamig, "Evaluation of incremental improvements to quantitative precipitation estimates in complex terrain," *Journal of Hydrometeorology*, vol. 10, no. 6, pp. 1507–1520, 2009.

[32] R. J. Doviak and D. S. Zrnic, *Doppler radar and weather observations*. Courier Corporation, 2013.

[33] V. E. Baer, "The transition from the present radar dissemination system to the nexrad information dissemination service (nids)," *Bulletin of the American Meteorological Society*, vol. 72, no. 1, pp. 29 – 33, 1991.

[34] T. D. Crum and R. L. Alberty, "The wsr-88d and the wsr-88d operational support facility," *Bulletin of the American Meteorological Society*, vol. 74, no. 8, pp. 1669–1687, 1993.

[35] T. D. Crum, R. E. Saffle, and J. W. Wilson, "An update on the nexrad program and future wsr-88d support to operations," *Weather and Forecasting*, vol. 13, no. 2, pp. 253 – 262, 1998.

[36] M. Xue, D. Wang, J. Gao, K. Brewster, and K. K. Droegemeier, "The advanced regional prediction system (arps), storm-scale numerical weather prediction and data assimilation.," *Meteorology & Atmospheric Physics*, vol. 82, 2003.

[37] R. J. Doviak, V. Bringi, A. Ryzhkov, A. Zahrai, and D. Zrnić, "Considerations for polarimetric upgrades to operational wsr-88d radars," *Journal of Atmospheric and Oceanic Technology*, vol. 17, no. 3, pp. 257 – 278, 2000.

[38] J. Vivekanandan, D. S. Zrnic, S. M. Ellis, R. Oye, A. V. Ryzhkov, and J. Straka, "Cloud microphysics retrieval using s-band dual-polarization radar measurements," *Bulletin of the American Meteorological Society*, vol. 80, no. 3, pp. 381 – 388, 1999.

[39] H. Liu and V. Chandrasekar, “Classification of hydrometeors based on polarimetric radar measurements: Development of fuzzy logic and neuro-fuzzy systems, and in situ verification,” *Journal of Atmospheric and Oceanic Technology*, vol. 17, no. 2, pp. 140–164, 2000.

[40] K. J. Westrick, C. F. Mass, and B. A. Colle, “The limitations of the wsr-88d radar network for quantitative precipitation measurement over the coastal western united states,” *Bulletin of the American Meteorological Society*, vol. 80, no. 11, pp. 2289–2298, 1999.

[41] S. Y. Matrosov, D. E. Kingsmill, B. E. Martner, and F. M. Ralph, “The utility of x-band polarimetric radar for quantitative estimates of rainfall parameters,” *Journal of Hydrometeorology*, vol. 6, no. 3, pp. 248 – 262, 2005.

[42] V. N. Bringi and V. Chandrasekar, *Polarimetric Doppler weather radar: principles and applications*. Cambridge university press, 2001.

[43] D. McLaughlin, D. Pepyne, V. Chandrasekar, B. Philips, J. Kurose, M. Zink, K. Droegemeier, S. Cruz-Pol, F. Junyent, J. Brotzge, *et al.*, “Short-wavelength technology and the potential for distributed networks of small radar systems,” *Bulletin of the American Meteorological Society*, vol. 90, no. 12, pp. 1797–1818, 2009.

[44] F. Junyent and V. Chandrasekar, “Theory and characterization of weather radar networks,” *Journal of Atmospheric and Oceanic Technology*, vol. 26, no. 3, pp. 474 – 491, 2009.

[45] E. Gorgucci and V. Chandrasekar, “Evaluation of attenuation correction methodology for dual-polarization radars: Application to x-band systems,” *Journal of Atmospheric and Oceanic Technology*, vol. 22, no. 8, pp. 1195 – 1206, 2005.

[46] S. Lim and V. Chandrasekar, “A robust attenuation correction system for reflectivity and differential reflectivity in weather radars,” *IEEE Transactions on Geoscience and Remote Sensing*, vol. 54, no. 3, pp. 1727–1737, 2016.

[47] N. Bharadwaj, V. Chandrasekar, and F. Junyent, "Signal processing system for the casa integrated project i radars," *Journal of Atmospheric and Oceanic Technology*, vol. 27, no. 9, pp. 1440–1460, 2010.

[48] M. D. Dettinger, F. M. Ralph, T. Das, P. J. Neiman, and D. R. Cayan, "Atmospheric rivers, floods and the water resources of california," *Water*, vol. 3, no. 2, pp. 445–478, 2011.

[49] T. W. Corringham, F. M. Ralph, A. Gershunov, D. R. Cayan, and C. A. Talbot, "Atmospheric rivers drive flood damages in the western united states," *Science advances*, vol. 5, no. 12, p. eaax4631, 2019.

[50] A. B. White, B. J. Moore, D. J. Gottas, and P. J. Neiman, "Winter storm conditions leading to excessive runoff above california's oroville dam during january and february 2017," *Bulletin of the American Meteorological Society*, vol. 100, no. 1, pp. 55–70, 2019.

[51] N. N. C. for Environmental Information (NCEI), "U.S. Billion-Dollar Weather and Climate Disasters." https://www.ncei.noaa.gov/access/billions/, 2023.

[52] Federal Emergency Management Agency (FEMA), "California Disaster Declaration, DR-4434." https://www.fema.gov/sites/default/files/2020-03/FEMA4434DRCA.pdf, 2020.

[53] J. M. Cordeira, J. Stock, M. D. Dettinger, A. M. Young, J. F. Kalansky, and F. M. Ralph, "A 142-year climatology of northern california landslides and atmospheric rivers," *Bulletin of the American Meteorological Society*, vol. 100, no. 8, pp. 1499–1509, 2019.

[54] A. B. White, K. M. Mahoney, R. Cifelli, and C. W. King, "Wind profilers to aid with monitoring and forecasting of high-impact weather in the southeastern and western united states," *Bulletin of the American Meteorological Society*, vol. 96, no. 12, pp. 2039–2043, 2015.

[55] A. J. Ray and A. B. White, "The hydrometeorology testbed–west legacy observing network: Supporting research to applications for atmospheric rivers and beyond," *Atmosphere*, vol. 10, no. 9, p. 533, 2019.

[56] P. J. Neiman, F. M. Ralph, A. White, D. Kingsmill, and P. Persson, "The statistical relationship between upslope flow and rainfall in california's coastal mountains: Observations during caljet," *Monthly Weather Review*, vol. 130, no. 6, pp. 1468–1492, 2002.

[57] J. Zhang, Y. Qi, D. Kingsmill, and K. Howard, "Radar-based quantitative precipitation estimation for the cool season in complex terrain: Case studies from the noaa hydrometeorology testbed," *Journal of Hydrometeorology*, vol. 13, no. 6, pp. 1836–1854, 2012.

[58] K. Nederhoff, R. Saleh, B. Tehranirad, L. Herdman, L. Erikson, P. L. Barnard, and M. van der Wegen, "Drivers of extreme water levels in a large, urban, high-energy coastal estuary – a case study of the san francisco bay," *Coastal Engineering*, vol. 170, p. 103984, 2021.

[59] B. Tehranirad, L. Herdman, K. Nederhoff, L. Erikson, R. Cifelli, G. Pratt, M. Leon, and P. Barnard, "Effect of fluvial discharges and remote non-tidal residuals on compound flood forecasting in san francisco bay," *Water*, vol. 12, no. 9, 2020.

[60] R. Martyr-Koller, H. Kernkamp, A. van Dam, M. van der Wegen, L. Lucas, N. Knowles, B. Jaffe, and T. Fregoso, "Application of an unstructured 3d finite volume numerical model to flows and salinity dynamics in the san francisco bay-delta," *Estuarine, Coastal and Shelf Science*, vol. 192, pp. 86–107, 2017.

[61] Y. Ma, V. Chandrasekar, H. Chen, and R. Cifelli, "Quantifying the potential of aqpi gap-filling radar network for streamflow simulation through a wrf-hydro experiment," *Journal of Hydrometeorology*, vol. 22, no. 7, pp. 1869 – 1882, 2021.

[62] P. V. Hobbs, "Organization and structure of clouds and precipitation on the mesoscale and microscale in cyclonic storms," *Reviews of Geophysics*, vol. 16, no. 4, pp. 741–755, 1978.

[63] B. D. Collins, N. S. Oakley, J. P. Perkins, A. E. East, S. C. Corbett, and B. J. Hatchett, "Linking mesoscale meteorology with extreme landscape response: Effects of narrow cold frontal rainbands (ncfr)," *Journal of Geophysical Research: Earth Surface*, vol. 125, no. 10, p. e2020JF005675, 2020. e2020JF005675 2020JF005675.

[64] M. de Orla-Barile, F. Cannon, N. S. Oakley, and F. M. Ralph, “A climatology of narrow cold-frontal rainbands in southern california,” *Geophysical Research Letters*, vol. 49, no. 2, p. e2021GL095362, 2022. e2021GL095362 2021GL095362.

[65] D. Kim, B. Nelson, and D.-J. Seo, “Characteristics of reprocessed hydrometeorological automated data system (hads) hourly precipitation data,” *Weather and Forecasting*, vol. 24, no. 5, pp. 1287 – 1296, 2009.

[66] A. B. White, M. L. Anderson, M. D. Dettinger, F. M. Ralph, A. Hinojosa, D. R. Cayan, R. K. Hartman, D. W. Reynolds, L. E. Johnson, T. L. Schneider, R. Cifelli, Z. Toth, S. I. Gutman, C. W. King, F. Gehrke, P. E. Johnston, C. Walls, D. Mann, D. J. Gottas, and T. Coleman, “A twenty-first-century california observing network for monitoring extreme weather events,” *Journal of Atmospheric and Oceanic Technology*, vol. 30, no. 8, pp. 1585 – 1603, 2013.

[67] P. A. Miller, M. F. Barth, and L. A. Benjamin, “An update on madis observation ingest, integration, quality control, and distribution capabilities,” in *Preprints, 21st International Conference on Interactive Information and Processing Systems (IIPS) for Meteorology, Oceanography, and Hydrology*, 2005.

[68] S. K. Biswas, R. Cifelli, and V. Chandrasekar, “Quantitative precipitation estimation using x-band radar for orographic rainfall in the san francisco bay area,” *IEEE Transactions on Geoscience and Remote Sensing*, pp. 1–1, 2022.

[69] J. J. Danielson, S. K. Poppenga, J. C. Brock, G. A. Evans, D. J. Tyler, D. B. Gesch, C. A. Thatcher, and J. A. Barras, “Topobathymetric Elevation Model Development using a New Methodology: Coastal National Elevation Database,” *Journal of Coastal Research*, vol. 76, no. sp1, pp. 75 – 89, 2016.

[70] Y. Wang and V. Chandrasekar, “Algorithm for estimation of the specific differential phase,” *Journal of Atmospheric and Oceanic Technology*, vol. 26, no. 12, pp. 2565 – 2578, 2009.

[71] R. J. Hogan, D. Bouniol, D. N. Ladd, E. J. O'Connor, and A. J. Illingworth, "Absolute calibration of 94/95-ghz radars using rain," *Journal of Atmospheric and Oceanic Technology*, vol. 20, no. 4, pp. 572–580, 2003.

[72] J. Delanoë, A. Protat, J.-P. Vinson, W. Brett, C. Caudoux, F. Bertrand, J. P. Du Châtelet, R. Hallali, L. Barthes, M. Haeffelin, *et al.*, "Basta: A 95-ghz fmcw doppler radar for cloud and fog studies," *Journal of Atmospheric and Oceanic Technology*, vol. 33, no. 5, pp. 1023–1038, 2016.

[73] E. Gorgucci, G. Scarchilli, and V. Chandrasekar, "A procedure to calibrate multiparameter weather radar using properties of the rain medium," *IEEE Transactions on Geoscience and Remote Sensing*, vol. 37, no. 1, pp. 269–276, 1999.

[74] E. A. Brandes, G. Zhang, and J. Vivekanandan, "Experiments in rainfall estimation with a polarimetric radar in a subtropical environment," *Journal of Applied Meteorology and Climatology*, vol. 41, no. 6, pp. 674–685, 2002.

[75] A. Tokay, D. B. Wolff, and W. A. Petersen, "Evaluation of the new version of the laser-optical disdrometer, ott parsivel2," *Journal of Atmospheric and Oceanic Technology*, vol. 31, no. 6, pp. 1276–1288, 2014.

[76] D. Jash, E. Resmi, C. Unnikrishnan, R. Sumesh, T. Sreekanth, N. Sukumar, and K. Ramachandran, "Variation in rain drop size distribution and rain integral parameters during southwest monsoon over a tropical station: An inter-comparison of disdrometer and micro rain radar," *Atmospheric Research*, vol. 217, pp. 24–36, 2019.

[77] D. Atlas, R. Srivastava, and R. S. Sekhon, "Doppler radar characteristics of precipitation at vertical incidence," *Reviews of Geophysics*, vol. 11, no. 1, pp. 1–35, 1973.

[78] J. Testud, E. Le Bouar, E. Obligis, and M. Ali-Mehenni, "The rain profiling algorithm applied to polarimetric weather radar," *Journal of Atmospheric and Oceanic Technology*, vol. 17, no. 3, pp. 332–356, 2000.

[79] M. Thurai, W. Petersen, A. Tokay, C. Schultz, and P. Gatlin, “Drop size distribution comparisons between parsivel and 2-d video disdrometers,” *Advances in Geosciences*, vol. 30, pp. 3–9, 2011.

[80] B. K. Seela, J. Janapati, P.-L. Lin, K. K. Reddy, R. Shirooka, and P. K. Wang, “A comparison study of summer season raindrop size distribution between palau and taiwan, two islands in western pacific,” *Journal of Geophysical Research: Atmospheres*, vol. 122, no. 21, pp. 11–787, 2017.

[81] E. A. Brandes, G. Zhang, and J. Vivekanandan, “An evaluation of a drop distribution–based polarimetric radar rainfall estimator,” *Journal of Applied Meteorology*, vol. 42, no. 5, pp. 652–660, 2003.

[82] M. Thurai, P. Gatlin, and V. Bringi, “Separating stratiform and convective rain types based on the drop size distribution characteristics using 2d video disdrometer data,” *Atmospheric Research*, vol. 169, pp. 416–423, 2016.

[83] S. Y. Matrosov, K. A. Clark, and D. E. Kingsmill, “A polarimetric radar approach to identify rain, melting-layer, and snow regions for applying corrections to vertical profiles of reflectivity,” *Journal of applied meteorology and climatology*, vol. 46, no. 2, pp. 154–166, 2007.

[84] R. Sánchez-Diezma, I. Zawadzki, and D. Sempere-Torres, “Identification of the bright band through the analysis of volumetric radar data,” *Journal of Geophysical Research: Atmospheres*, vol. 105, no. D2, pp. 2225–2236, 2000.

[85] Y. Qi, J. Zhang, P. Zhang, and Q. Cao, “Vpr correction of bright band effects in radar qpes using polarimetric radar observations,” *Journal of Geophysical Research: Atmospheres*, vol. 118, no. 9, pp. 3627–3633, 2013.

[86] E. A. Brandes, G. Zhang, and J. Vivekanandan, “Corrigendum,” *J. Appl. Meteor.*, vol. 44, p. 186, 2005.

[87] S. M. Martinaitis, S. B. Cocks, M. J. Simpson, A. P. Osborne, S. S. Harkema, H. M. Grams, J. Zhang, and K. W. Howard, “Advancements and characteristics of gauge ingest and quality control within the multi-radar multi-sensor system,” *Journal of Hydrometeorology*, vol. 22, no. 9, pp. 2455–2474, 2021.

[88] A. Bellon, G. W. Lee, and I. Zawadzki, “Error statistics of vpr corrections in stratiform precipitation,” *Journal of Applied Meteorology*, vol. 44, no. 7, pp. 998 – 1015, 2005.

[89] V. Lakshmanan, T. Smith, G. Stumpf, and K. Hondl, “The warning decision support system–integrated information,” *Weather and Forecasting*, vol. 22, no. 3, pp. 596–612, 2007.